



# Photometric Analyses of Saturn's Small Moons: Aegaeon, Methone, and Pallene Are Dark; Helene and Calypso Are Bright

M. M. Hedman<sup>1</sup> , P. Helfenstein<sup>2</sup> , R. O. Chancia<sup>1,3</sup> , P. Thomas<sup>2</sup>, E. Roussos<sup>4</sup> , C. Paranicas<sup>5</sup> , and A. J. Verbiscer<sup>6</sup>

<sup>1</sup> Department of Physics, University of Idaho, Moscow, ID 83844, USA

<sup>2</sup> Cornell Center for Astrophysics and Planetary Science, Cornell University, Ithaca NY 14853, USA

<sup>3</sup> Center for Imaging Science, Rochester Institute of Technology, Rochester NY 14623, USA

<sup>4</sup> Max Planck Institute for Solar System Research, Göttingen D-37077, Germany

<sup>5</sup> APL, John Hopkins University, Laurel MD 20723, USA

<sup>6</sup> Department of Astronomy, University of Virginia, Charlottesville, VA 22904, USA

Received 2019 September 26; revised 2019 December 3; accepted 2019 December 13; published 2020 February 26

## Abstract

We examine the surface brightnesses of Saturn's smaller satellites using a photometric model that explicitly accounts for their elongated shapes and thus facilitates comparisons among different moons. Analyses of *Cassini* imaging data with this model reveal that the moons Aegaeon, Methone, and Pallene are darker than one would expect given trends previously observed among the nearby mid-sized satellites. On the other hand, the trojan moons Calypso and Helene have substantially brighter surfaces than their co-orbital companions Tethys and Dione. These observations are inconsistent with the moons' surface brightnesses being entirely controlled by the local flux of E-ring particles, and therefore strongly imply that other phenomena are affecting their surface properties. The darkness of Aegaeon, Methone, and Pallene is correlated with the fluxes of high-energy protons, implying that high-energy radiation is responsible for darkening these small moons. Meanwhile, Prometheus and Pandora appear to be brightened by their interactions with the nearby dusty F ring, implying that enhanced dust fluxes are most likely responsible for Calypso's and Helene's excess brightness. However, there are no obvious structures in the E ring that would preferentially brighten these two moons, so there must either be something subtle in the E-ring particles' orbital properties that leads to asymmetries in the relevant fluxes, or something happened recently to temporarily increase these moons' brightnesses.

*Unified Astronomy Thesaurus concepts:* [Saturnian satellites \(1427\)](#); [Natural satellites \(Solar system\) \(1089\)](#); [Photometry \(1234\)](#); [Surface photometry \(1670\)](#); [Planetary magnetosphere \(997\)](#); [Planetary rings \(1254\)](#)

*Supporting material:* machine-readable tables

## 1. Introduction

Saturn's regular moons exhibit a very diverse range of spectral and photometric properties, with Enceladus having an extremely bright and ice-rich surface, while the leading side of Iapetus is exceptionally dark due to being covered with a layer of debris derived from Saturn's irregular satellites (for recent reviews, see Hendrix et al. 2018; Thomas et al. 2018; Verbiscer et al. 2018). For the mid-sized moons orbiting between Titan and the rings (i.e., Mimas, Enceladus, Tethys, Dione and Rhea), many of the observed spectral and photometric trends have been attributed to interactions with the E ring. This broad and diffuse ring consists of dust-sized, ice-rich particles generated by Enceladus' geological activity that impact the surfaces of different moons at different rates. The brightness and density of the E ring is strongly correlated with the geometric albedos of these satellites at visible (Verbiscer et al. 2007) and radio wavelengths (Ostro et al. 2010; Le Gall et al. 2019), as well as spectral features like the depth of water-ice absorption bands (Filacchione et al. 2012, 2013). Furthermore, there are brightness asymmetries between the leading and trailing sides of these moons that can be attributed to differences in the fluxes of E-ring particles (Buratti et al. 1998; Schenk et al. 2011; Scipioni et al. 2013, 2014; Hendrix et al. 2018; Le Gall et al. 2019).

However, there are several smaller moons orbiting within the E ring whose surface scattering properties deviate from the trends observed among the larger moons. On the one hand, four

extremely small moons (Aegaeon, Anthe, Methone, and Pallene) are found within the E-ring's inner flank. Aegaeon is situated between Janus and Mimas in the G ring, while Methone, Anthe, and Pallene orbit between Mimas and Enceladus. One might therefore expect these moons to follow the same trend as Janus, Mimas, and Enceladus, but in fact, they appear to be somewhat darker than this trend would predict (Thomas et al. 2018; Verbiscer et al. 2018). On the other hand, the small moons Telesto and Calypso share Tethys' orbit, while Helene and Polydeuces share Dione's orbit, but they do not all appear to have the same spectrophotometric properties as their larger companions (Verbiscer et al. 2007, 2018; Filacchione et al. 2012, 2013).

A major challenge in interpreting existing brightness estimates of these objects is that many of them are significantly elongated, and so their brightness varies substantially depending on their orientation relative to the observer and the Sun, leading to large scatter in the disk-integrated brightness estimates at any given phase angle. Fortunately, all of these objects are spin-locked and so their orientation relative to the Sun and the spacecraft can be securely predicted. Furthermore, almost all of these moons were observed at high enough resolution to determine their shapes, and Aegaeon, Methone, and Pallene in particular are very close to perfect ellipsoids. It should therefore be possible to model their shape-related brightness variations to a fair degree of accuracy, and thereby derive estimates of their surface brightnesses that can be compared to those of the larger moons.

This paper describes a new investigation of Saturn's moons that uses a photometric model to obtain precise and comparable measurements of the surface brightnesses for both the small and mid-sized moons orbiting interior to Titan. The brightness estimates for the mid-sized moons, along with the smaller moons Janus and Epimetheus, are consistent with previous studies in that they are clearly correlated with the local flux of E-ring particles. However, this work also confirms that many small moons deviate from this basic trend, implying that other processes influence the moons' surface brightnesses. Specifically, we find that (1) Aegaeon is exceptionally dark, (2) Methone and Pallene are darker than one would expect given their locations between Mimas and Enceladus, (3) Calypso and Helene are brighter than their larger companions, and (4) Prometheus and Pandora are brighter than moons orbiting nearby like Atlas, Janus, and Epimetheus. Aegaeon, Methone, and Pallene are most likely dark because they occupy belts of high-energy proton fluxes. While the mechanism by which this radiation darkens their surfaces is still obscure, we find that the overall brightnesses of these moons are probably determined by the ratio of the energetic proton flux to the E-ring particle flux. On the other hand, the excess brightness of Helene, Calypso, Prometheus, and Pandora is most likely due to some localized increase in the particle flux. For Prometheus and Pandora, the additional flux of particles from the F ring is probably responsible for increasing their brightness. However, there is no obvious particle source that would preferentially brighten Calypso and Helene more than their co-orbital companions, so the brightness of these moons either involves a previously unknown asymmetry in the E-ring particle flux or is a transient phenomenon due to a recent event like an impact.

Section 2 below describes the *Cassini* imaging data used in this study and how it is transformed into estimates of the disk-integrated brightness of Saturn's various moons. Section 3 then describes the photometric model we use to convert these disk-integrated brightness estimates into estimates of the moons' surface brightness while accounting for the moons' variably elongated shapes. Finally, Section 4 describes the trends among these shape-corrected brightness estimates and their implications, while Section 5 summarizes our findings.

## 2. Observations and Preliminary Data Reduction

The disk-integrated brightness estimates considered in this study are derived from images obtained by the Narrow Angle Camera (NAC) of the Imaging Science Subsystem (ISS) on board the *Cassini* Spacecraft (Porco et al. 2004). These images were all calibrated using version 3.9 of the Cisscal package to remove dark current and instrumental electronic noise, apply flat-field corrections, and convert the raw data numbers to values of radiance factors  $I/F$ , a standard dimensionless measure of reflectance that is unity for an illuminated Lambertian surface viewed at normal incidence and emission angles (Porco et al. 2004; West et al. 2010). Here,  $I$  is the scattered intensity of light, and  $\pi F$  is the specific solar flux over the camera filter bandpass.

While this analysis focuses on the photometry of the small moons, in order to facilitate comparisons with the mid-sized satellites, we will consider data for all of the satellites interior to Titan except for Daphnis (whose location within a narrow gap in the main rings would have required specialized algorithms). We searched for images containing all moons obtained by the NAC through its clear filters using the OPUS

search tool on the PDS ring-moon system node (<https://pds-rings.seti.org/search>). For the small moons Aegaeon, Anthe, Methone, and Pallene, as well as the trojan moons Telesto, Calypso, Helene, and Polydeuces, we considered all images where the moon was observed at phase angles below  $80^\circ$  (at higher phase angles, the signal-to-noise ratio for these moons was often too poor to be useful), while for Pan, Atlas, Prometheus, Pandora, Janus, Epimetheus, Mimas, Enceladus, Tethys, Dione, and Rhea, we only considered images where the moon was at phase angles between  $20^\circ$  and  $40^\circ$ . This more restricted phase range corresponds to conditions with the best signal-to-noise ratio data for the smaller moons, and reduces the number of images that needed to be analyzed to a manageable level.

Since nearly all of the images of the small moons were unresolved, this analysis will only consider disk-integrated brightness estimates for the moons, which were computed following approaches similar to those described in Hedman et al. (2010). This process begins by selecting a region within each image that contains the entire signal from the moon based on visual inspection. Then, instrumental and ring backgrounds are removed from this region using one of three different procedures depending on the moon:

1. *Aegaeon and Pan*. For these moons, the dominant backgrounds come from the nearby rings (the A ring for Pan and the G ring for Aegaeon). Each image was therefore geometrically navigated based on the positions of stars in the field of view and the appropriate SPICE kernels (Acton 1996) using a variant of the CAVIAR software package (<https://www.imcce.fr/recherche/equipes/pegase/caviar>). We then used regions extending 10 pixels on either side of the selected region along the moon's orbit to determine the mean background image brightness as a function of ringplane radius. This profile was then interpolated onto the pixels in the selected region containing the moon and removed from that region.
2. *Atlas, Anthe, Methone, Pallene, Telesto, Calypso, Helene, and Polydeuces*. For these moons, instrumental backgrounds dominate, and these are typically a stronger function of row than sample number (West et al. 2010). Hence, we used regions 10 columns wide on either side of the region containing the moon to define a background brightness level as a function of row number, which was then removed from all of the pixels in the selected regions.
3. *Prometheus, Pandora, Janus, Epimetheus, Mimas, Enceladus, Tethys, Dione, and Rhea*. These larger moons were often resolved and so the signal-to-noise ratio was much higher than that for the smaller moons. Hence, we used regions that are 10 columns wide on either side of the region containing the moon to define a mean background brightness level that was removed from all of the pixels in the selected regions.

After removing the backgrounds, the total brightness of the object in each image was computed and expressed in terms of an effective area,  $A_{\text{eff}}$ , which is the equivalent area of material with  $I/F = 1$  that would be required to account for the observed brightness:

$$A_{\text{eff}} = \sum_x \sum_y I/F_{x,y} \times \Omega_{\text{pixel}} \times D^2 \quad (1)$$

where  $x$  and  $y$  are the row and column numbers of the pixels in the selected region,  $I/F_{x,y}$  is the (background-subtracted) brightness in the  $x,y$  pixel,  $\Omega_{\text{pixel}} = (6 \mu\text{rad})^2$  is the assumed solid angle subtended by a NAC pixel, and  $D$  is the distance between the spacecraft and the object during the observation (designated as “Range” in Tables 8–28 of Appendix C). The assumed values for  $D$  are derived from the appropriate SPICE kernels (Acton 1996). This approach deviates from traditional integrated disk measurement convention in that an effective whole-disk area is measured at each phase angle rather than the magnitude equivalent of an average whole-disk reflectance. Two advantages of this approach for our study are that (1) it requires no a priori knowledge of the object’s average size, and (2) it easily accommodates target blur in which subpixel-sized objects are smeared across several pixels due to spacecraft motion and/or long camera exposures. We also estimate the statistical uncertainty on  $A_{\text{eff}}$  based on the standard deviation of the brightness levels in the second region after any radial trends have been removed. Note that this procedure underestimates the true uncertainty in the measurements but is still a useful way to identify images with low signal-to-noise ratios. For the smaller objects, we also computed their mean position in the field of view by computing the coordinates (in pixels) of the streaks center of light  $x_c$  and  $y_c$ :

$$x_c = \frac{\sum_x \sum_y x \times I/F_{x,y}}{\sum_x \sum_y I/F_{x,y}} \quad (2)$$

$$y_c = \frac{\sum_x \sum_y y \times I/F_{x,y}}{\sum_x \sum_y I/F_{x,y}}. \quad (3)$$

These numbers are not used directly for any part of this study. However, they are useful for identifying images where the background levels were not removed properly, since in those images, the computed center of light would fall outside of the image of the moon.

For the larger moons, the signal-to-noise ratio for every image was sufficiently high that all unsaturated images yielded useful estimates of  $A_{\text{eff}}$ . After excluding any moons with saturated pixels, we had the following numbers of data points for these moons: 40 for Prometheus, 40 for Pandora, 53 for Janus, 47 for Epimetheus, 76 for Mimas, 82 for Enceladus, 67 for Tethys, 67 for Dione, and 74 for Rhea (see Tables 18–26 in Appendix C). For the smaller moons, we visually inspected the regions containing the moons and excluded any images where these regions were obviously corrupted by bad pixels or cosmic rays, or where the computed center of light was noticeably displaced from the bright pixels containing the signal from the moon. For Aegaeon, Anthe, Methone, and Pallene, we also excluded any images where  $A_{\text{eff}}$  was negative or more than 10 times the median value among all of the images, as well as any images where the brightest pixel in the relevant region was more than 10 times the median pixel brightness times the number of pixels in the region (this removed images contaminated by a bad pixel or cosmic ray that was not obvious upon visual inspection). Finally, we excluded any images of Aegaeon, Anthe, Methone, and Pallene with exposures less than 0.5 s because these usually had poor signal-to-noise ratios, and any images of Anthe, Methone, and Pallene with exposures longer than 2 s, where unresolved

images could be saturated. Similarly, we excluded images of Polydeuces with exposures longer than 0.68 s and any images of Telesto, Calypso, and Helene with exposures longer than 0.15 s. After these selections, the final number of measurements for the small moons were: 168 for Aegaeon, 167 for Anthe, 187 for Methone, 159 for Pallene, 41 for Pan, 71 for Atlas, 142 for Telesto, 157 for Calypso, 122 for Helene, and 136 for Polydeuces (see Tables 8–17 in Appendix C). Estimates of  $A_{\text{eff}}$  for these images, along with relevant geometric parameters like the sub-solar and sub-observer latitudes and longitudes, are provided in Tables 8–26 in Appendix C.

### 3. A Photometric Model for Elongated Bodies

The challenges associated with photometric analyses of small moons are best seen in the left-hand panels of Figures 1–3, which show the effective area estimates for these moons as functions of the observed phase angle. While there is a clear trend of decreasing brightness with increasing phase angle, the data points also show a relatively large amount of scatter around this basic trend. This scatter cannot be entirely attributed to measurement errors because it is strongly correlated with the viewing geometry. In particular, the moons’ sub-Saturn and anti-Saturn quadrants are systematically lower in  $A_{\text{eff}}$  than their leading and trailing quadrants. These variations can be more clearly documented by plotting the fractional residuals from the mean trend (where  $A_{\text{eff}}$  is assumed to be a linear or quadratic function of phase angle) as functions of the sub-observer longitude. With the exception of Helene, Pan, and Atlas, these plots all show clear sinusoidal patterns with maxima around  $90^\circ$  and  $270^\circ$  and minima around  $0^\circ$  and  $180^\circ$ .

These trends with sub-observer longitude arise because these small moons have ellipsoidal shapes and are tidally locked so that their long axes point toward Saturn. Resolved images of these moons show that they are all significantly elongated (see Table 1; note that Anthe was never observed with sufficient resolution to determine its shape and size accurately). Furthermore, the relative magnitudes of the longitudinal brightness variations shown in Figures 1–3 are generally consistent with the relative  $a/b$  ratios of these different moons, with Aegaeon being the most elongated object and the one with the largest longitudinal brightness variations, followed by Calypso, Prometheus, and Methone.

#### 3.1. Variations in Projected Area Do Not Adequately Account for the Moons’ Photometric Properties

The simplest way to account for these shape-related brightness variations is to divide the observed  $A_{\text{eff}}$  by the plane-projected area of the object  $A_{\text{phys}}$ , which, for an ellipsoidal object, is given by the following formula (Vickers 1996):

$$A_{\text{phys}} = \pi [b^2 c^2 \cos^2 \lambda_O \cos^2 \phi_O + a^2 c^2 \cos^2 \lambda_O \sin^2 \phi_O + a^2 b^2 \sin^2 \lambda_O]^{1/2} \quad (4)$$

where  $a$ ,  $b$ , and  $c$  are the dimensions of the ellipsoid, while  $\lambda_O$  and  $\phi_O$  are the sub-observer latitude and longitude for the object. The resulting ratio then yields the disk-averaged

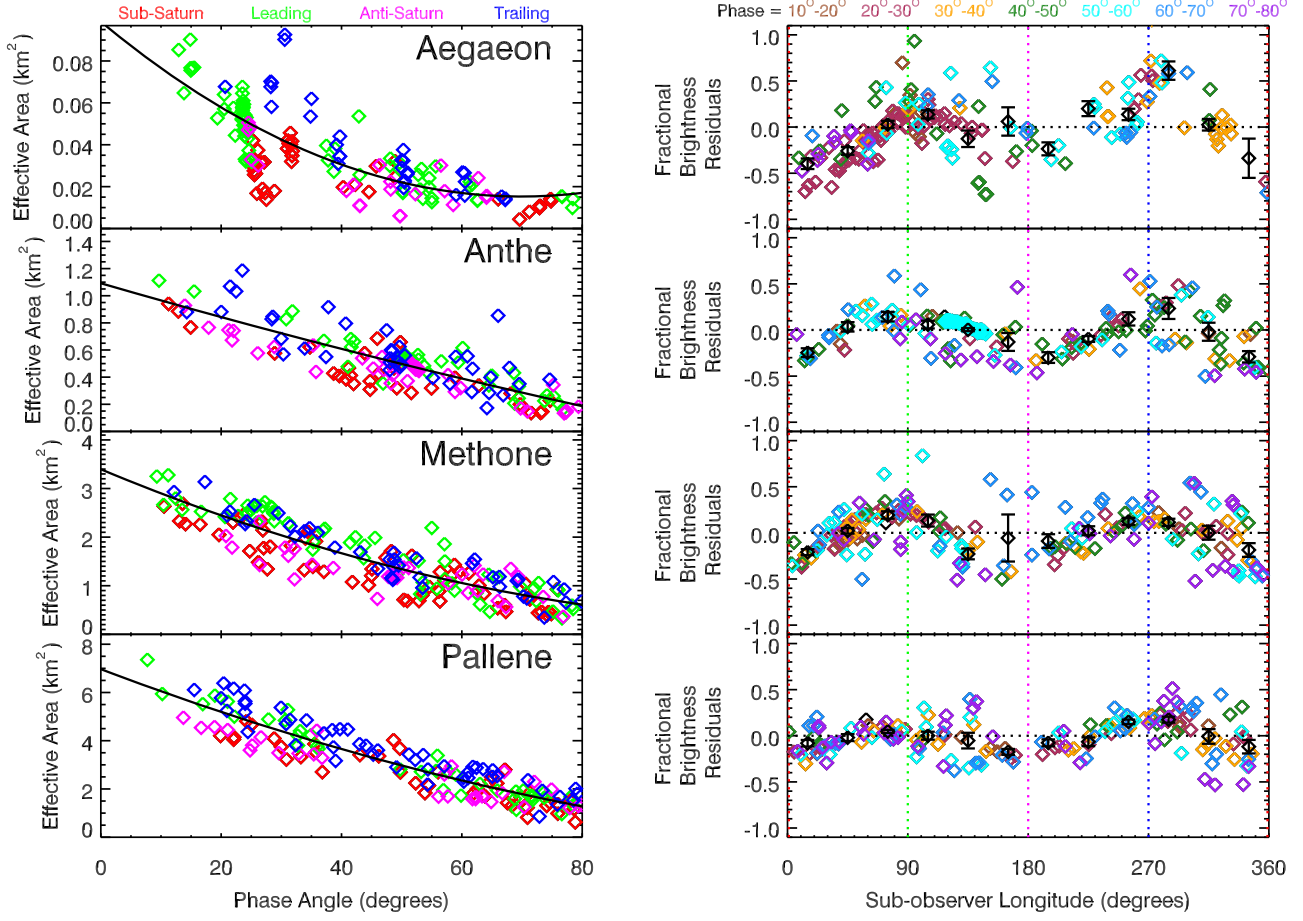


**Figure 1.** Summary of the brightness measurements for Aegaeon, Anthe, Methone, and Pallene. The left-hand plots show the effective areas  $A_{\text{eff}}$  of the moons as a function of phase angle, with the data points color coded by the quadrant viewed by the spacecraft. The right-hand plots show the fractional residuals of the brightness estimates relative to the quadratic trend shown as a solid line in the left-hand plots. Note that all of these objects are consistently brighter when their leading or trailing sides are viewed than when their sub-Saturn or anti-Saturn sides are viewed.

reflectance of the object:

$$\langle I/F \rangle = \frac{A_{\text{eff}}}{A_{\text{phys}}} \quad (5)$$

Tables 8–28 include estimates of  $A_{\text{phys}}$  computed assuming that these bodies have the shape parameters given in Table 1, and Figures 4–6 show the resulting estimates of  $\langle I/F \rangle$  as functions of phase and sub-observer longitude. While the fractional brightness residuals around the mean phase curve are somewhat smaller for  $\langle I/F \rangle$  than they are for  $A_{\text{eff}}$ , the dispersion is still rather large. For Aegaeon, Prometheus, and Pandora there are still clear maxima at  $90^\circ$  and  $270^\circ$ , while for Methone, Pallene, Telesto, and Calypso the dispersion at larger phase angles has a similar magnitude for the two parameters.

### 3.2. A Generic Ellipsoid Photometric Model (GEPM)

The major problem with using  $\langle I/F \rangle$  is that this parameter only accounts for the viewing geometry, but not how the moon is illuminated by the Sun, which, for very elongated bodies, can strongly affect the observed brightness (Helfenstein & Veverka 1989). Muinonen & Lumme (2015) provide an analytical formula for elongated bodies assuming the surface follows a Lommel-Seeliger scattering law, which is appropriate for dark surfaces. However, the applicability of such a model

for bright objects like many of Saturn’s moons is less clear. We therefore use a more generic numerical method to translate whole-disk brightness data into information about the object’s global average reflectance behavior, which we call the Generic Ellipsoid Photometric Model, or GEPM.

The GEPM predicts an ellipsoidal object’s  $A_{\text{eff}}$  in any given image assuming its surface reflectance  $R$  follows a generic scattering law that is a function of the cosines of the incidence and emission angles  $\cos i$  and  $\cos e$ . The predicted effective area of an object whose surface obeys these scattering laws is given by the following integral:

$$A_{\text{pred}} = \int_{++} (\cos e) R r_{\text{eff}}^2 \cos \lambda d\lambda d\phi \quad (6)$$

where  $\lambda$  and  $\phi$  are the latitude and longitude on the object, the  $++$  sign indicates that the integral is performed only over the part of the object that is both illuminated and visible (i.e., where  $\cos i$  and  $\cos e$  are both positive), the factor of  $\cos e$  in this integral accounts for variations in the projected size of the area element, and  $r_{\text{eff}}$  is the effective radius of the object at a given latitude and longitude, which is given by the following expression:

$$r_{\text{eff}}^2 = [b^2 c^2 \cos^2 \lambda \cos^2 \phi + a^2 b^2 \sin^2 \lambda \sin^2 \phi]^{1/2} \quad (7)$$

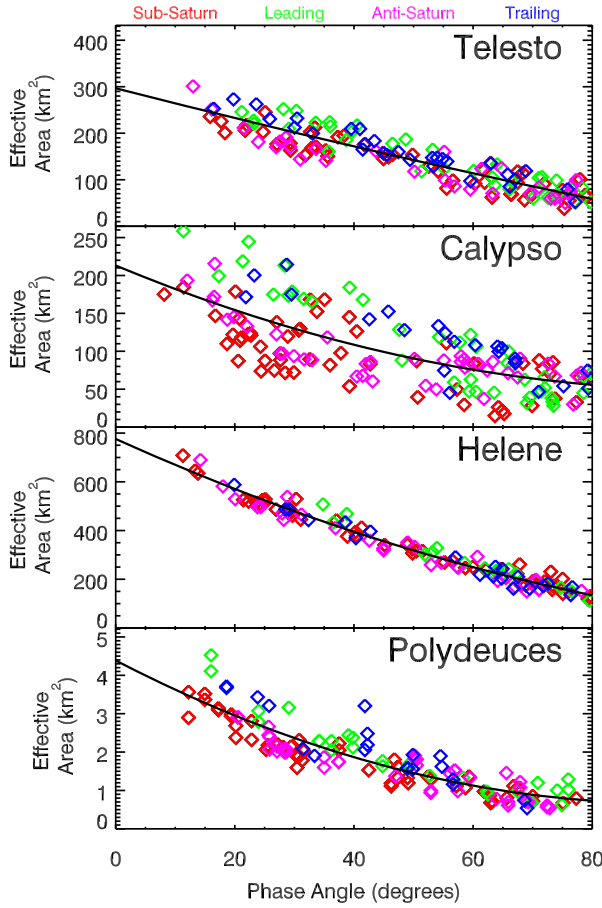


**Figure 2.** Summary of the brightness measurements for the trojan moons Telesto, Calypso, Helene, and Polydeuces. The left-hand plots show the effective areas  $A_{\text{eff}}$  of the moons as a function of phase angle, with the data points color coded by the quadrant viewed by the spacecraft. The right-hand plots show the fractional residuals of the brightness estimates relative to the quadratic trend shown as a solid line in the left-hand plots. Note that these objects are consistently brighter when their leading or trailing sides are viewed than they are when their sub-Saturn or anti-Saturn sides are viewed.

The factors of  $\cos i$  and  $\cos e$  in the above integral are also functions of  $\lambda$  and  $\phi$  that depend upon the viewing and illumination geometry, as well as the object's shape. To obtain these functions, we first use the sub-observer latitude  $\lambda_O$  and longitude  $\phi_O$  to define a unit vector pointing from the center of the body toward the spacecraft:

$$\hat{o} = \cos \lambda_O \cos \phi_O \hat{x} + \cos \lambda_O \sin \phi_O \hat{y} + \sin \lambda_O \hat{z} \quad (8)$$

where  $\hat{x}$  points from the moon toward Saturn,  $\hat{y}$  points in the direction of orbital motion, and  $\hat{z}$  points along the object's rotation axis. Similarly, we use the sub-solar latitude  $\lambda_S$  and longitude  $\phi_S$  to define a unit vector pointing from the center of the body toward the Sun

$$\hat{s} = \cos \lambda_S \cos \phi_S \hat{x} + \cos \lambda_S \sin \phi_S \hat{y} + \sin \lambda_S \hat{z}. \quad (9)$$

Finally, for each latitude  $\lambda$  and longitude  $\phi$  on the surface, we compute the surface normal for the body, which depends on the shape parameters  $a$ ,  $b$ , and  $c$ .

$$\hat{n} = \frac{\frac{\cos \lambda \cos \phi}{a} \hat{x} + \frac{\cos \lambda \sin \phi}{b} \hat{y} + \frac{\sin \lambda}{c} \hat{z}}{\sqrt{\frac{\cos^2 \lambda \cos^2 \phi}{a^2} + \frac{\cos^2 \lambda \sin^2 \phi}{b^2} + \frac{\sin^2 \lambda}{c^2}}}. \quad (10)$$

The cosines of the incidence and emission angles are then given by the standard expressions  $\cos i = \hat{n} \cdot \hat{s}$  and  $\cos e = \hat{n} \cdot \hat{o}$ .

The above expressions allow us to evaluate  $A_{\text{pred}}$  for any given scattering law  $R$ , including Lunar-Lambert functions or Akimov functions (McEwen 1991; Shkuratov et al. 2011; Schröder et al. 2014). However, for the sake of concreteness, we will here assume that  $R$  is given by the Minnaert function (Minnaert 1941):

$$R_M = B(\cos i)^k (\cos e)^{1-k}, \quad (11)$$

where the quantities  $k$  and  $B$  will be assumed to be constants for each image. Note that if we assume that  $k = 1$ , the above expression reduces to the Lambert photometric function:

$$R_L = B \cos i. \quad (12)$$

For a generic Minnaert function, Equation (6) becomes:

$$\begin{aligned} A_{\text{pred}} &= B \int_{++} (\cos i)^k (\cos e)^{2-k} r_{\text{eff}}^2 \cos \lambda d\lambda d\phi \\ &= Ba_{\text{pred}}. \end{aligned} \quad (13)$$

The factor of  $B$  moves outside the integral, and the remaining factor  $a_{\text{pred}}$  can be numerically evaluated for any specified viewing and illumination geometry, so long as we also assume values for the object's shape parameters  $a$ ,  $b$ , and  $c$ , as well as the photometric parameter  $k$ . A Python function that evaluates  $a_{\text{pred}}$  given these parameters is provided in Appendix A. From this, we can estimate the “brightness coefficient” parameter  $B$

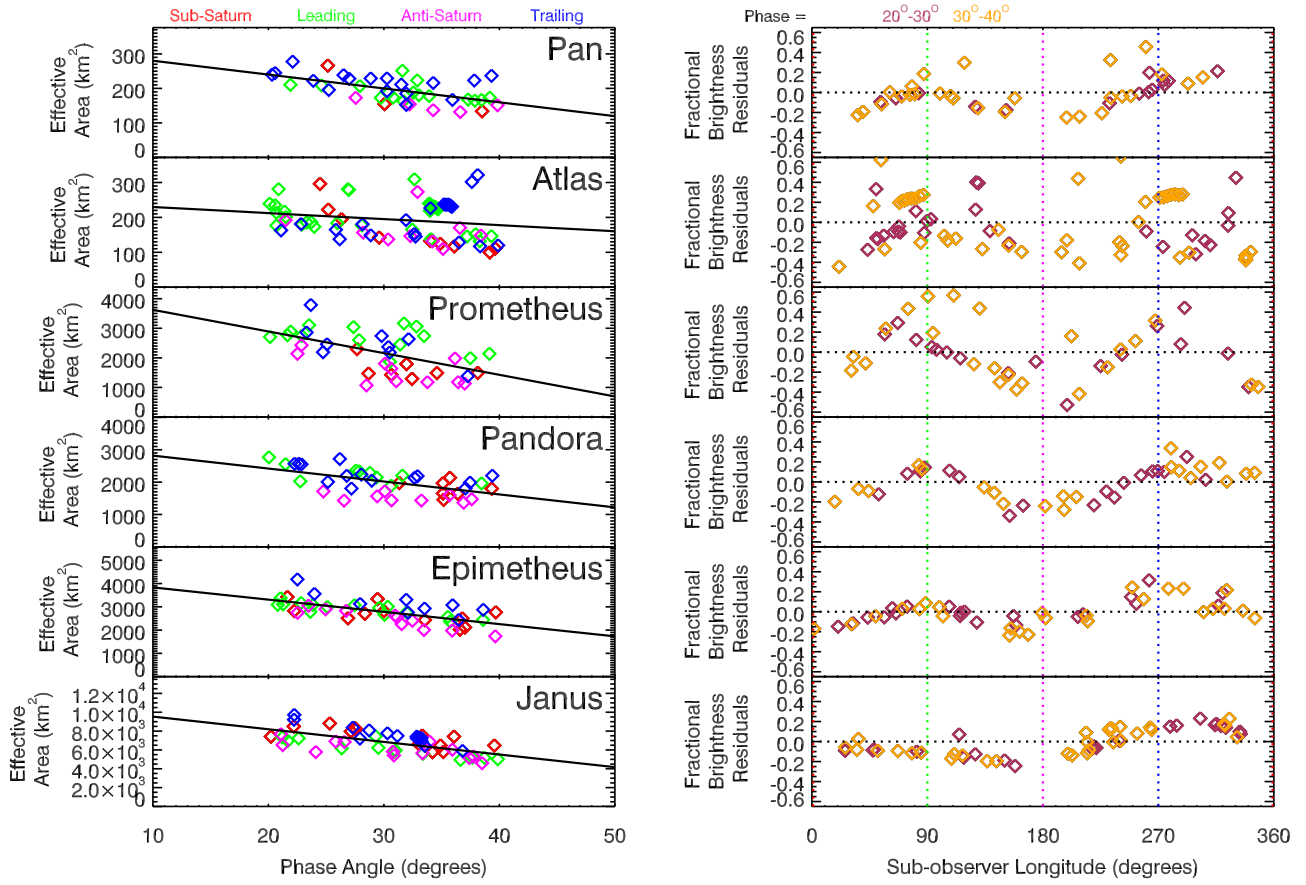


**Figure 3.** Summary of the brightness measurements for the ring moons. The left-hand plots show the effective areas  $A_{\text{eff}}$  of the moons as a function of phase angle, with the data points color coded by the quadrant viewed by the spacecraft. The right-hand plots show the fractional residuals of the brightness estimates relative to the linear trend shown as a solid line in the left-hand plots. Note that these objects are often brighter when their leading or trailing sides are viewed than they are when their sub-Saturn or anti-Saturn sides are viewed.

to be simply the ratio  $A_{\text{eff}}/a_{\text{pred}}$ . Note that  $B$  is not equal to the mean reflectance  $\langle I/F \rangle$ , even for spherical bodies, because it includes corrections for the varying incidence and emission angles across the disk.

Of course, the estimated value of  $B$  depends on the assumed values of  $a$ ,  $b$ ,  $c$ , and  $k$ , which are typically estimated from resolved images. While only a few images are needed to obtain useful estimates of  $a$ ,  $b$ , and  $c$ , the parameter  $k$  can depend on the observed phase angle and location on the object, and so  $k$  is far harder to estimate reliably for the full range of observation geometries. Previous studies of resolved *Voyager* images of the mid-sized moons found that Mimas, Enceladus, Tethys, Dione, and Rhea had  $k = 0.65$ ,  $0.78$ ,  $0.63$ ,  $0.53$ – $0.56$ , and  $0.52$ – $0.54$ , respectively, at phase angles between  $5^\circ$  and  $17^\circ$  (Buratti 1984), while a study of resolved *Cassini* images of Methone found that  $k = 0.887$ – $0.003\alpha$  ( $\alpha$  being the solar phase angle) based on images obtained at phase angles between  $45^\circ$  and  $65^\circ$  (Thomas et al. 2013). Thus, this parameter likely varies among these moons and with observation geometry and terrain for each moon.

Figure 7 shows the fractional differences in the predicted values of  $a_{\text{pred}}$  between a model where  $k = 0.5$  and a model where  $k = 1$  (that is, a Lambertian surface). Each data point corresponds to a different combination of sub-observer and sub-solar locations scattered over the entire object. For the spherical object, there is a trend where the  $k = 0.5$  model becomes 15% brighter than the Lambertian model at high

phase angles. Very prolate and oblate objects show a similar overall trend but with considerably more scatter depending on the exact viewing and illumination geometry. This suggests that one could constrain  $k$  by minimizing the rms scatter in the estimated brightness coefficients from unresolved images of elongated bodies at each phase angle. In practice, the rms scatter in the brightness coefficients for the various moons are very weak functions of  $k$ , most likely because real surface albedo variations and/or instrumental noise dominate the dispersion in the brightness coefficients. We therefore expect that a thorough analysis of resolved images would be needed to constrain  $k$  reliably for each of the moons, and such an analysis is well beyond the scope of this paper.

Fortunately, it turns out that the results presented below are insensitive to the exact value of  $k$ . We bracket the range of possible  $k$ -values by considering cases where  $k = 0.5$ ,  $0.75$ , and  $1.0$  when estimating the brightnesses of the various moons. Estimates of  $a_{\text{pred}}$  derived from all three cases are provided in Tables 8–28. However, since the brightness differences among these different scenarios are subtle, we will normally only plot brightness coefficients computed assuming the surface follows a Lambertian scattering law (i.e.,  $k = 1$ ).

### 3.3. Validation of General Ellipsoid Photometric Model with Saturn's Small Moons

The utility of this model can be most clearly demonstrated by taking a closer look at the data for Aegaeon. Aegaeon is not

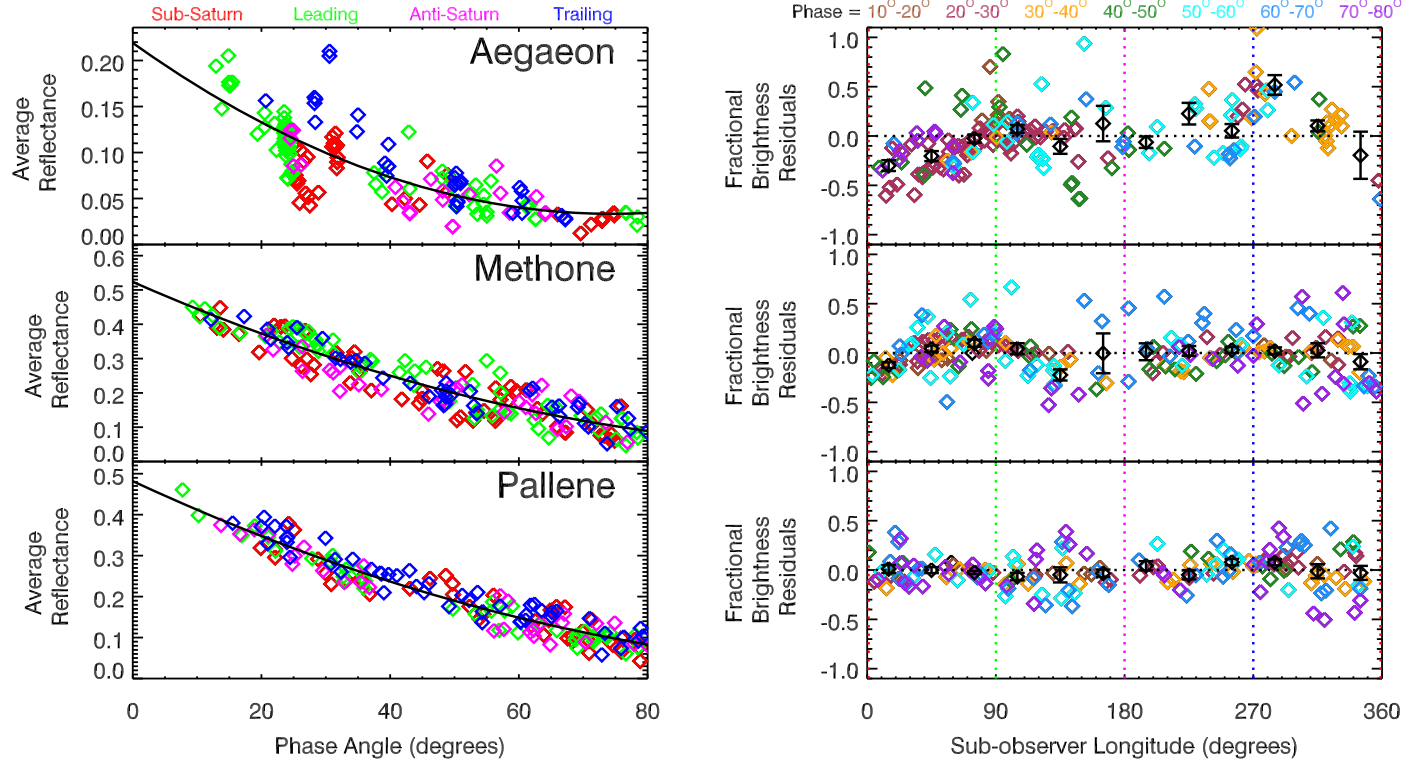


**Figure 4.** Average reflectances of Aegaeon, Methone, and Pallene. The left-hand plots show the average reflectances of the moons as a function of phase angle, with the data points color coded by the quadrant viewed by the spacecraft. The right-hand plots show the fractional residuals of the brightness estimates relative to the quadratic trend shown as a solid line in the left-hand plots. While the longitudinal brightness variations are reduced compared to the effective areas shown in Figure 1, they are not completely removed, especially at higher phase angles.

**Table 1**  
Satellite Shapes from Resolved Images (Thomas 2010; Thomas et al. 2013; Thomas & Helfenstein 2019, and Appendix B)

Object	$a$ (km)	$b$ (km)	$c$ (km)	$b/a$	$c/b$	$R_m$ (km)
Aegaeon	$0.70 \pm 0.05$	$0.25 \pm 0.06$	$0.20 \pm 0.08$	$0.36 \pm 0.09$	$0.80 \pm 0.37$	$0.33 \pm 0.06$
Methone	$1.94 \pm 0.02$	$1.29 \pm 0.04$	$1.21 \pm 0.02$	$0.66 \pm 0.02$	$0.94 \pm 0.03$	$1.45 \pm 0.03$
Pallene	$2.88 \pm 0.07$	$2.08 \pm 0.07$	$1.84 \pm 0.07$	$0.72 \pm 0.03$	$0.89 \pm 0.04$	$2.23 \pm 0.07$
Mimas	$207.8 \pm 0.5$	$196.7 \pm 0.5$	$190.6 \pm 0.3$	$0.947 \pm 0.003$	$0.969 \pm 0.003$	$198.2 \pm 0.4$
Enceladus	$256.6 \pm 0.3$	$251.4 \pm 0.2$	$248.3 \pm 0.2$	$0.980 \pm 0.002$	$0.988 \pm 0.001$	$252.1 \pm 0.2$
Tethys	$538.4 \pm 0.3$	$528.3 \pm 1.1$	$526.3 \pm 0.6$	$0.981 \pm 0.002$	$0.996 \pm 0.002$	$531.0 \pm 0.6$
Dione	$563.4 \pm 0.6$	$561.3 \pm 0.5$	$559.6 \pm 0.4$	$0.996 \pm 0.001$	$0.997 \pm 0.001$	$561.4 \pm 0.4$
Rhea	$765.0 \pm 0.7$	$763.1 \pm 0.6$	$762.4 \pm 0.6$	$0.998 \pm 0.001$	$0.999 \pm 0.001$	$763.5 \pm 0.6$
Pan	$17.3 \pm 0.2$	$14.1 \pm 0.2$	$10.5 \pm 0.5$	$0.815 \pm 0.015$	$0.745 \pm 0.037$	$13.7 \pm 0.3$
Atlas	$20.4 \pm 0.1$	$17.7 \pm 0.2$	$9.3 \pm 0.3$	$0.868 \pm 0.011$	$0.525 \pm 0.018$	$14.9 \pm 0.2$
Prometheus	$68.5 \pm 0.5$	$40.5 \pm 1.4$	$28.1 \pm 0.4$	$0.591 \pm 0.021$	$0.694 \pm 0.026$	$42.8 \pm 0.7$
Pandora	$51.5 \pm 0.3$	$39.5 \pm 0.3$	$31.5 \pm 0.2$	$0.767 \pm 0.007$	$0.797 \pm 0.008$	$40.0 \pm 0.3$
Epimetheus	$64.8 \pm 0.3$	$58.1 \pm 0.2$	$53.5 \pm 0.2$	$0.897 \pm 0.005$	$0.921 \pm 0.005$	$58.6 \pm 0.3$
Janus	$101.7 \pm 0.9$	$92.9 \pm 0.3$	$74.5 \pm 0.3$	$0.913 \pm 0.009$	$0.802 \pm 0.004$	$89.0 \pm 0.5$
Telesto	$16.6 \pm 0.3$	$11.7 \pm 0.3$	$9.6 \pm 0.2$	$0.705 \pm 0.022$	$0.821 \pm 0.027$	$12.3 \pm 0.3$
Calypso	$14.7 \pm 0.3$	$9.3 \pm 0.9$	$6.4 \pm 0.3$	$0.632 \pm 0.062$	$0.688 \pm 0.073$	$9.5 \pm 0.4$
Helene	$22.6 \pm 0.2$	$19.6 \pm 0.3$	$13.3 \pm 0.2$	$0.867 \pm 0.015$	$0.679 \pm 0.015$	$18.1 \pm 0.2$
Polydeuces	$1.75 \pm 0.2$	$1.55 \pm 0.2$	$1.31 \pm 0.2$	$0.89 \pm 0.15$	$0.85 \pm 0.17$	$1.53 \pm 0.2$

only the most elongated moon, it was also observed in multiple ARCORBIT sequences where the spacecraft repeatedly imaged the moon as it moved around a significant fraction of its orbit, yielding true rotational light curves. The images from eight of these sequences are listed in Table 2, while the values of  $A_{\text{eff}}$  are shown in Figure 8, plotted as a function of the sub-observer longitude. All show clear brightness variations that can be

attributed to the changing viewing geometry of the moon, with the lowest signals seen when the sub-observer longitude is near  $0^\circ$  or  $180^\circ$ , and the highest signals seen when the sub-observer longitude is close to  $90^\circ$  or  $270^\circ$ . However, it is also clear that the maxima and minima are not precisely aligned with these four longitudes (this is most clearly seen in the Rev 201, 210, and 236 data). This result clearly demonstrates that the

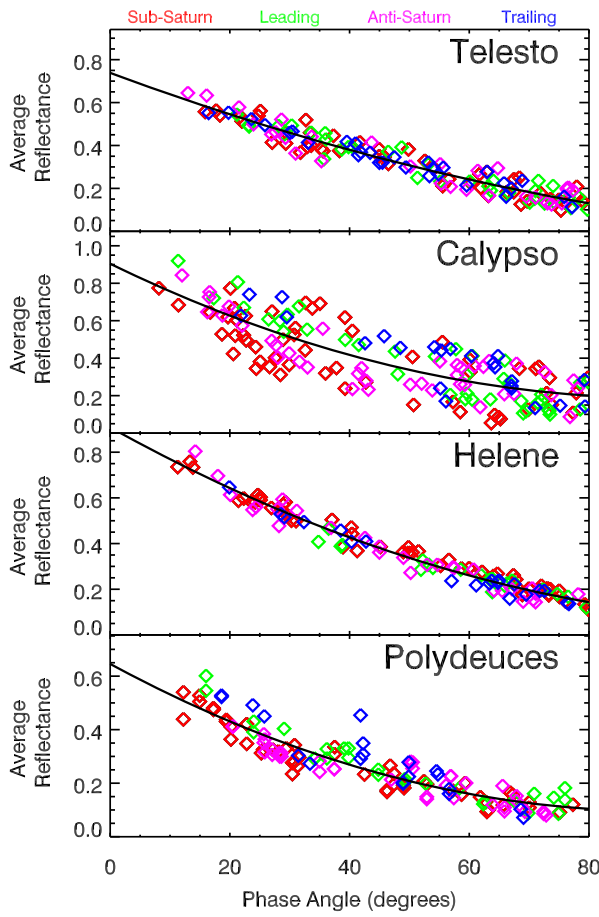


**Figure 5.** Average reflectances of Telesto, Calypso, Helene, and Polydeuces with their nominal shapes. The left-hand plots show the average reflectances as a function of phase angle, with the data points color coded by the quadrant viewed by the spacecraft. The right-hand plots show the fractional residuals of the average reflectances relative to the quadratic trend shown as a solid line in the left-hand plots. While the longitudinal brightness variations are reduced compared to the effective areas shown in Figure 2, they are not completely removed, especially at higher phase angles.

projected area is not the only thing affecting the moon's projected brightness. Indeed, the green curves show the variations in the projected area, scaled to match the mean signal in the data. These variations are both too subtle to match the observations, and the observed and predicted peaks and troughs do not line up. By contrast, the GEPM predictions are a much better fit to the data in all cases. This demonstrates that accounting for the lighting geometry not only causes the predicted locations of peaks and troughs to shift into alignment with the data, but it also increases the predicted fractional brightness variations.

More generally, Figures 9–11 show the estimated brightness coefficients for the small moons derived assuming that they have the nominal shapes given in Table 1 and surfaces that follow a Lambertian scattering law (assuming the surfaces follow Minnaert scattering laws with  $k = 0.5$  and  $0.75$  yield nearly identical results). Compared with Figures 4–6, the scatter around the mean trends with phase angle are much tighter for almost all of the moons. The exceptions to this trend are Helene, Polydeuces, Janus, and Epimetheus, for which the dispersions in  $B$  and  $\langle I/F \rangle$  are comparable. These exceptions are likely because these four moons are the most spherical in shape, so the corrections included in the GEPM are less important. There are some outlying data points for Aegaeon, Atlas, and Prometheus, but these can be attributed to the low

signals from Aegaeon and mis-estimated background levels for Atlas and Prometheus.

Besides the reduction in dispersion, the fractional brightness residuals no longer show double-peaked trends with co-rotating longitude. Instead, the most obvious remaining longitudinal trends are that the leading sides of Pallene, Epimetheus, and Janus are 10%–20% darker than their trailing sides. Such leading-trailing asymmetries are reminiscent of the longitudinal brightness variations seen in ground-based, Voyager, and *Cassini* images of the mid-sized icy moons (Noland et al. 1974; Franz & Millis 1975; Buratti & Veverka 1984; Verbiscer & Veverka 1989, 1992, 1994; Buratti et al. 1990, 1998; Pitman et al. 2010; Schenk et al. 2011). Figure 12 shows the brightness coefficients for these larger moons derived assuming the same Lambertian model as was used for the smaller moons.<sup>7</sup> Consistent with prior work (Buratti et al. 1998; Schenk et al. 2011; Hendrix et al. 2018; Verbiscer et al. 2018), we find that Tethys, Dione, and Rhea have brighter leading sides, while Mimas has a brighter trailing side. This overall trend is thought to arise because the particles in the E ring preferentially strike the leading sides of moons orbiting exterior to Enceladus and the trailing sides of moons orbiting interior to Enceladus (Hamilton & Burns 1994). The longitudinal brightness

<sup>7</sup> Due to the nearly spherical shape of these moons, the dispersions around the mean trends in these cases do not change much between  $A_{\text{eff}}$ ,  $\langle I/F \rangle$  and  $B$ .

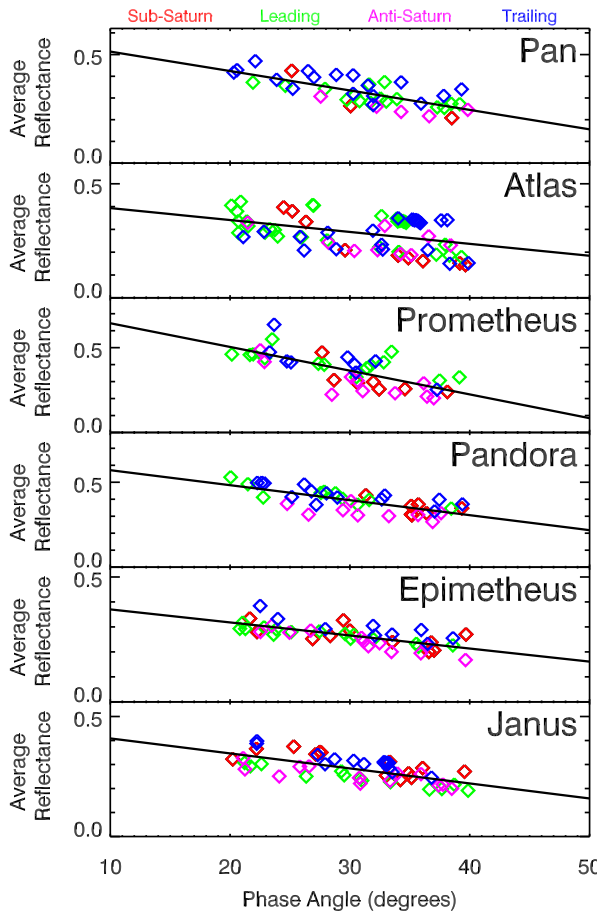
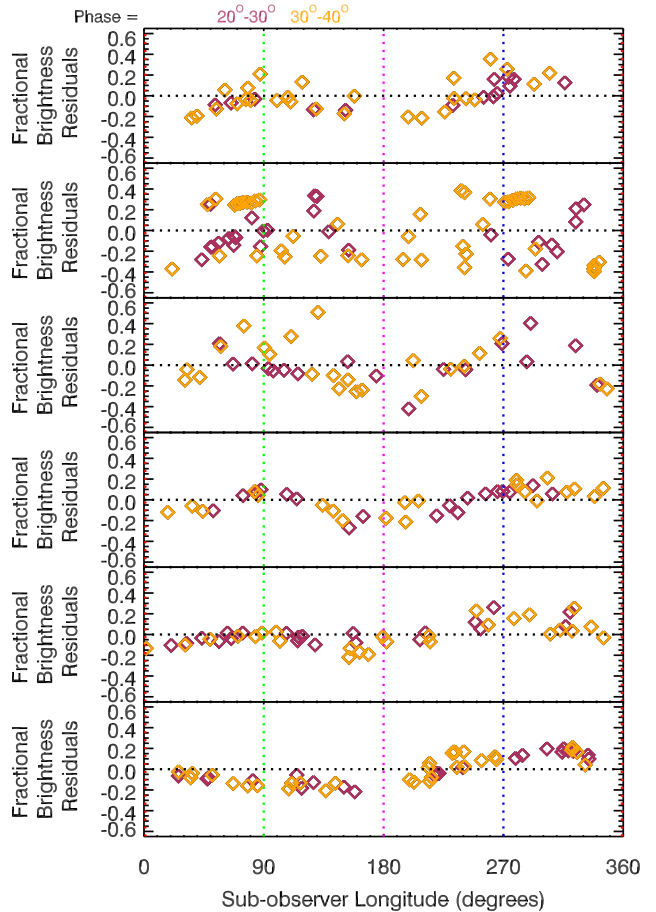


**Figure 6.** Average reflectances of the ring moons with their nominal shapes. The left-hand plots show the average reflectances of the moons as a function of phase angle, with the data points color coded by the quadrant viewed by the spacecraft. The right-hand plots show the fractional residuals of the brightness estimates relative to the linear trend shown as a solid line in the left-hand plots. Again, while the longitudinal brightness variations are slightly reduced compared to the effective areas shown in Figure 3, they are not completely removed.

asymmetries observed on Pallene, Janus, and Epimetheus are consistent with this pattern, but it is worth noting that Aegaeon, Methone, and the trojan moons do not appear to have such asymmetries. The implications of these findings will be discussed further in Section 4 below.

Finally, we may consider what happens if we relax the assumption that the shapes of these moons equal the best-fit values from resolved images. Figures 13 and 14 show the rms residuals as functions of the aspect ratios  $b/a$  and  $c/b$  for Aegaeon, Anthe, Methone, Pallene, and the trojan moons, along with the aspect ratios derived from the resolved images. For the smaller moons shown in Figure 13, the two methods for determining the shape agree fairly well. The best-fit solution for Aegaeon falls where  $b \simeq c$  and  $b \simeq 0.3a$ , consistent with the constraints from the resolved images. For Methone, the two methods yield best-fit solutions with the same value of  $c/b \simeq 0.95$  and  $b/a \simeq 0.65$ , although the photometry favors a slightly higher value for  $b/a$ . Similarly, for Pallene, we find both methods give  $c/b \simeq 0.9$ , but the resolved images favor  $b/a \simeq 0.7$ , while the photometry prefers 0.8. This discrepancy is likely related to the variations in the surface brightness with longitude mentioned above. More sophisticated photometric models could potentially resolve this difference, but even this level of consistency gives us some confidence in this method. Also, the photometric data for Anthe clearly favor a shape with



$b/a \simeq 0.7$  and  $c/b \simeq 0.95$ , which implies that Anthe has a shape similar to Methone.

The shapes of the trojan moons derived from the photometry and resolved images are somewhat more discrepant. For Polydeuces, both methods yield  $b/a \simeq 0.8$  and  $c/b \simeq 1$  with rather large uncertainties. For Calypso, both methods agree that  $b/a \simeq 0.6$ , but the photometry favors  $c/b \simeq 0.9$  while the resolved images prefer  $c/b \simeq 0.7$ . For Telesto, both methods agree that  $c/b \simeq 0.8$ , but the photometry favors  $b/a \simeq 0.8$  while the resolved images prefer  $b/a \simeq 0.7$ . The biggest discrepancies are found with Helene, where the photometry prefers a much more spherical shape than was found with the resolved images. These differences most likely arise because the shapes of these objects are not simple ellipsoids like the smaller moons appear to be. Again, a more sophisticated photometric model that could accommodate more complex shapes would likely reduce these discrepancies. Even so, the relatively simple GEPM clearly reduces the dispersion in the brightness estimates for Telesto, Polydeuces, and especially Calypso, and so it provides a useful basis for comparing the brightnesses of all these satellites.

#### 4. Brightness Trends among Saturn's Small Moons

The GEPM appears to provide reasonably consistent surface brightness estimates for moons with a range of sizes and shapes, so we will now compare these brightness estimates for

**Table 2**  
*Cassini ISS NAC Images Belonging to the Various ARCORBIT Sequences*

Sequence	Images
Rev 177	N1735282418 N1735287671 N1735287895 N1735292924 N1735293148 N1735298177 N1735298401 N1735303430 N1735303654
Rev 180	N1738781138 N1738781312 N1738785881 N1738786055 N1738790624 N1738790798 N1738804853 N1738805027 N1738809596 N1738809770 N1738814339 N1738814513 N1738842971
Rev 188	N1746467285 N1746467459 N1746472918 N1746473092 N1746484184 N1746484358 N1746489747 N1746489817 N1746489991 N1746495450 N1746495624 N1746501083 N1746501257
Rev 201	N1769540993 N1769545670 N1769549999 N1769550173 N1769559005 N1769559179 N1769563508 N1769563682 N1769568011 N1769572514 N1769572688 N1769577191 N1769581520 N1769581694 N1769586023 N1769586197
Rev 206	N1783325708 N178332836 N1783333010 N1783343963 N1783347440 N1783347614 N1783351091 N1783351265 N1783358393 N1783358567
Rev 210	N1796027549 N1796033113 N1796035895 N1796041459 N1796052587 N1796055369 N1796058151 N1796060933 N1796069279 N1796085971 N1796088753 N1796091535
Rev 236	N1843274411 N1843274619 N1843274723 N1843274810 N1843274984 N1843275331 N1843275435 N1843276039 N1843276143 N1843276747 N1843276851 N1843277559 N1843278163 N1843278267 N1843278739 N1843279092 N1843279196 N1843279800 N1843280612 N1843281924 N1843282326 N1843282500 N1843282957 N1843284269 N1843285081 N1843285685 N1843286261 N1843286614 N1843287322 N1843288134 N1843289446 N1843289550 N1843289848 N1843290022 N1843290479 N1843291083 N1843291187 N1843291791 N1843291895 N1843292499 N1843292603 N1843293311 N1843293609 N1843293783 N1843294136 N1843294240 N1843294844 N1843294948 N1843295552 N1843295656 N1843296260 N1843296364 N1843296968 N1843297072 N1843297370 N1843297544 N1843297897 N1843298001 N1843298605 N1843298709 N1843299313 N1843299417 N1843300021 N1843300125 N1843300729 N1843301131 N1843303074 N1843303886 N1843304490 N1843304594 N1843304892 N1843305066 N1843305419 N1843305523 N1843306127 N1843306231 N1843306835 N1843306939 N1843307543 N1843308251 N1843308827 N1843309180 N1843309888 N1843309992 N1843310596 N1843310700 N1843312012 N1843312116 N1843312414 N1843312588 N1843312941 N1843313649 N1843313753 N1843315065 N1843315169 N1843316175 N1843316349 N1843316702 N1843320110 N1843321275 N1843321879 N1843321983 N1843322587 N1843323399 N1843323864 N1843324006 N1843324110 N1843324422
Rev 239	N1848936800 N1848936974 N1848940466 N1848940640 N1848944132 N1848944306 N1848947798 N1848947972 N1848951464 N1848951638 N1848955130 N1848962392 N1848962462 N1848962636 N1848969794 N1848969968 N1848969968

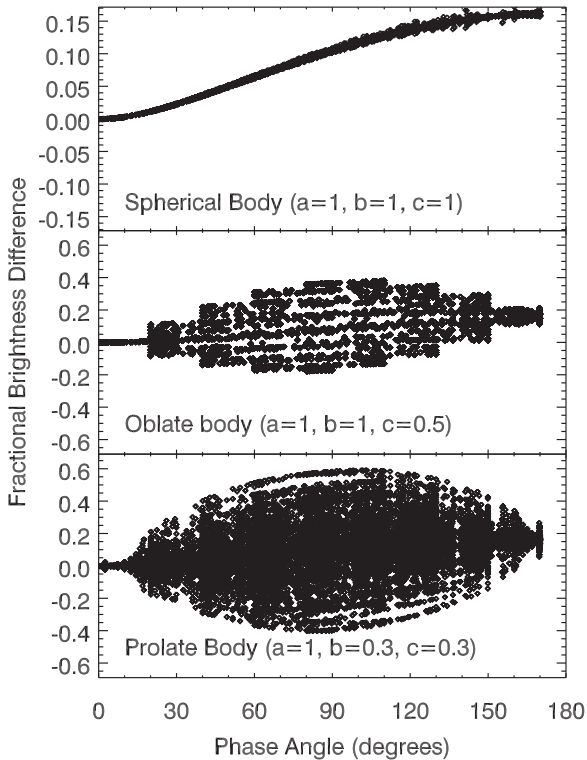


**Figure 7.** Fractional difference between the predicted values of  $a_{\text{pred}}$  between a Minnaert model with  $k = 0.5$  and a Lambertian model for three different shapes. Each point corresponds to a different combination of viewing and illuminate geometries scattered uniformly over the objects' surface.

the different moons and identify trends that might clarify the processes responsible for determining the moons' visible surface brightness. We begin by describing the specific brightness values we will use for this project in Section 4.1. Section 4.2 then shows how these brightness parameters for the mid-sized moons correlate with the local flux of E-ring particles, which is consistent with prior work. Next, Section 4.3 examines why some of the small moons are darker than expected given their locations within the E ring, and shows that high-energy proton radiation probably also influences the moons' surface brightness. Finally, Section 4.4 discusses the small moons that are brighter than one might expect given their locations.

#### 4.1. Comparable Brightness Estimates for Saturn's Moons

The calculations described in Section 3 demonstrate that our model is a sensible way to quantify the surface brightness of elongated moons. However, the absolute values of  $B$  derived by this method are not directly comparable to traditional parameters like geometric or Bond albedos previously reported in the literature. In principle, the derived values of  $B$  as functions of phase angle could be extrapolated to zero, and then we could translate that value of  $B$  to a geometric albedo for an equivalent spherical object. However, in practice, performing such an extrapolation would be problematic because the small moons were rarely observed by *Cassini* at phase angles below  $10^\circ$ , so we have no information about the magnitude or shape of the opposition surges for these bodies. Also, since these objects are not spherical, the amount of light scattered will depend on the orientation of the body, which complicates the

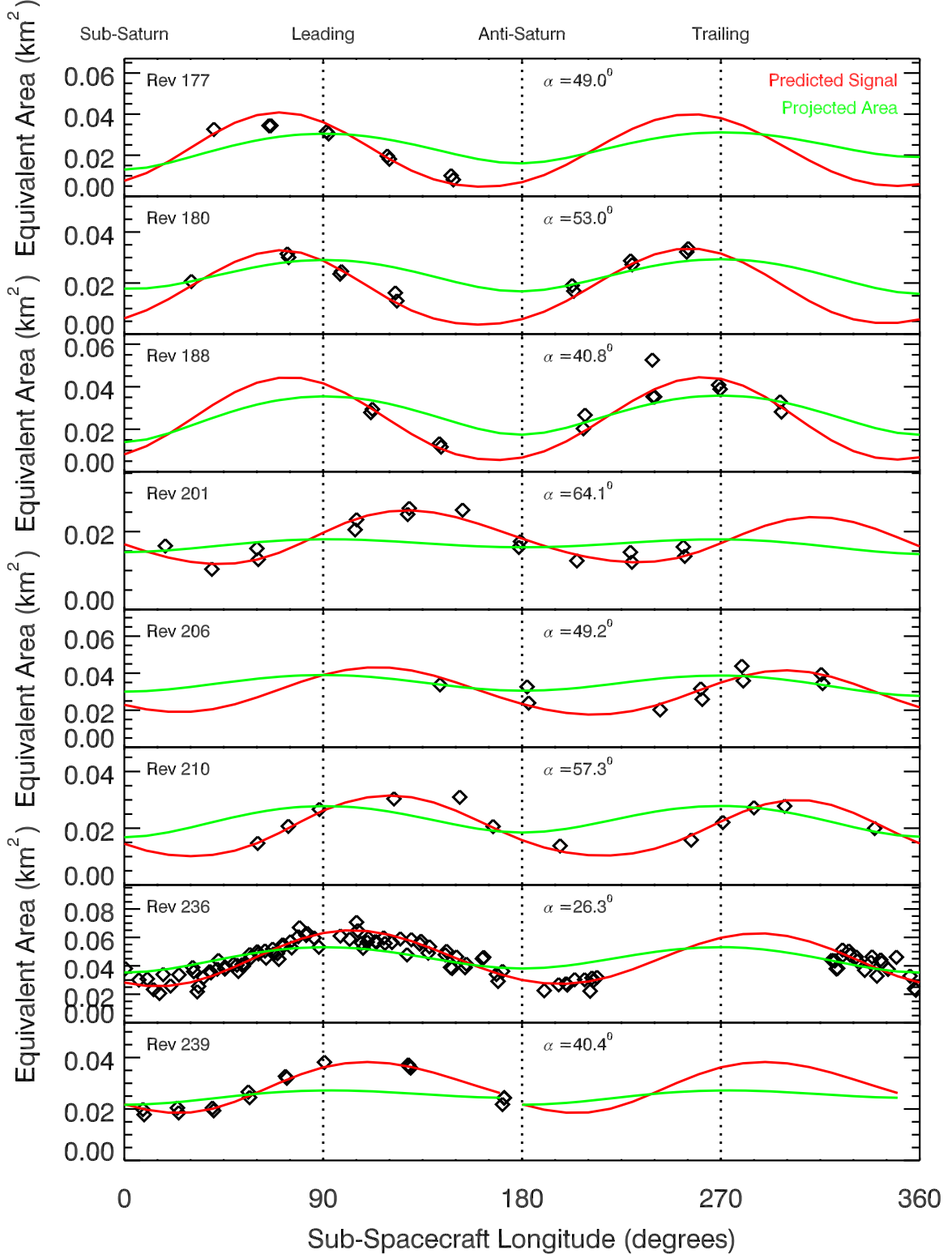


**Figure 8.** Observed and predicted rotation light curves for Aegaeon. Each plot shows data from one particular ARCORBIT observation of Aegaeon, which measured the brightness of Aegaeon as a function of sub-observer longitude. The data points are the measured data, while the green curves show the variations in the projected area of the moon, and the red curves show the predicted variations in  $a_{\text{pred}}$  for a Lambertian model with Aegaeon's nominal shape (Minnaert models with  $k = 0.5$  and  $k = 0.75$  show nearly the same trends). The predicted curves are both scaled to best match the median observed signal. The GEPM model predictions clearly match the data much better than the effective areas.

classical definition of albedo. On the other hand, it is relatively straightforward to estimate  $B$  for Saturn's other moons, and so we have chosen that approach for this analysis.

In order to compare the reflectances of these objects, we only consider the data obtained between phase angles of  $20^\circ$  and  $40^\circ$ , and fit the brightness coefficients in this phase range to a

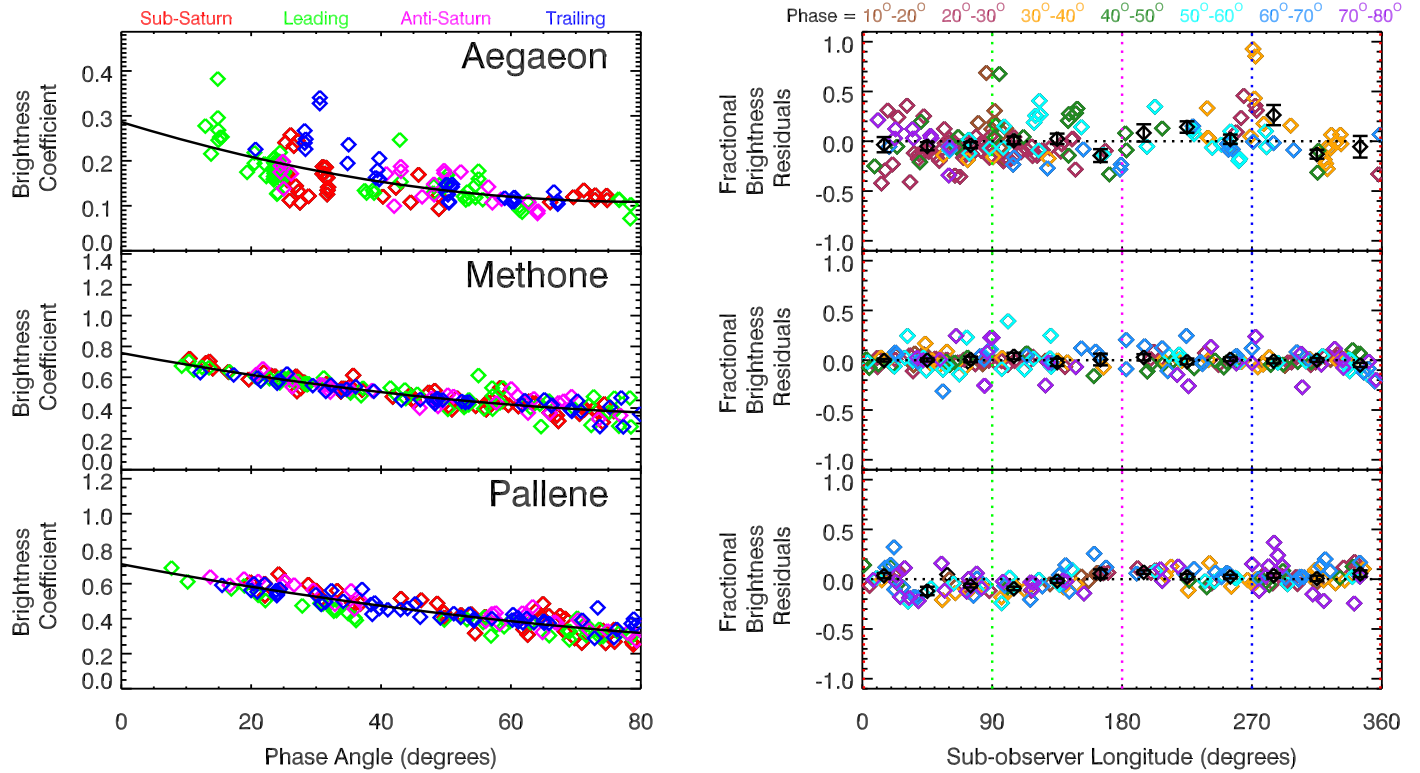


**Figure 9.** Estimated brightness coefficients for Lambertian models of Aegaeon, Methone, and Pallene with their nominal shapes. The left plots show the brightness coefficients of the moons as a function of phase angle, with the data points color coded by the quadrant viewed by the spacecraft. The right-hand plots show the fractional residuals of the brightness estimates relative to the quadratic trend shown as a solid line in the left-hand plots. The longitude-dependent brightness variations are almost completely removed, and those that remain, like Pallene’s leading-trailing asymmetry, are probably real surface features.

linear function of phase angle  $\alpha$ :

$$B(\alpha) = B_0 + (\alpha - 30^\circ) C_B. \quad (14)$$

Note that  $B_0$  is the brightness coefficient at  $30^\circ$  phase, which is in the middle of the range of observed phase angles and so does not depend on any questionable extrapolations. For a spherical object of radius  $r$  observed at  $0^\circ$  and  $30^\circ$  phase,  $a_{\text{pred}} = 2.12r^2$  and  $1.86r^2$ , respectively, for a Lambertian scattering law (for a Minnaert scattering law with  $k = 0.5$ , these numbers become  $a_{\text{pred}} = 2.12r^2$  and  $1.91r^2$ , respectively). Hence, the average reflectance the object would have at  $30^\circ$  if it were a sphere is  $\langle I/F \rangle_{\text{sphere}} = 0.59B_0$  for a Lambertian scattering law (or  $\langle I/F \rangle_{\text{sphere}} = 0.61B_0$  for a Minnaert  $k = 0.5$  scattering law). The corresponding geometric albedo of the object assuming that the linear phase function could be extrapolated to an appropriately small phase angle  $\alpha_0$  would be<sup>8</sup>

$$\mathcal{A}_{\text{sphere}} = 0.67[B_0 + (\alpha_0 - 30^\circ) C_B]. \quad (15)$$

For the mid-sized moons Mimas, Enceladus, Tethys, Dione, and Rhea, this expression yields  $\mathcal{A}_{\text{sphere}} = 0.60, 0.92, 0.75, 0.57$  and  $0.63$ , respectively for  $\alpha_0 = 10^\circ$ , which are  $0.97, 0.92, 0.90, 0.87$ , and  $1.00$  times the central values reported by Thomas et al. (2018), so at this phase angle, the calculations are reasonably consistent. However, if we extrapolate to zero degrees phase,

we obtain  $\mathcal{A}_{\text{sphere}} = 0.65, 0.99, 0.82, 0.63$  and  $0.55$ , which are  $0.68, 0.72, 0.67, 0.63$ , and  $0.74$  times the geometric albedos measured by Verbiscer et al. (2007). This discrepancy most likely reflects the fact that this formula does not account for the opposition surges associated with these moons.

For the sake of simplicity, we will just use the parameters  $B_0$  in our analyses below. Tables 3–5 tabulate  $B_0$  and  $C_B$  for all of Saturn’s moons examined here assuming either a Lambertian scattering law or a Minnaert scattering law with  $k = 0.75$  or  $k = 0.50$ . These tables also include statistical errors based on the scatter of the points around the mean trend, and a systematic error that is based on the uncertainty in the mean size of the object. Additional systematic uncertainties associated with the size of the pixel response function are on the order of 5% and are not included here because these systematic uncertainties are common to all of the brightness estimates and so do not affect the moons’ relative brightness. Figure 15 compares the values of  $B_0$  derived assuming the different scattering laws for each of the moons. This plot shows that models assuming lower values of the Minnaert  $k$  parameter yield systematically lower estimates of  $B_0$ , but that these differences are rather subtle and have little effect on the relative brightnesses of the various moons. Hence, for the sake of simplicity, we will only consider the estimates of  $B_0$  computed assuming a Lambertian scattering law from here on. Figure 16 plots these central brightness values as a function of distance from the center of Saturn, along with estimates of the relative E-ring particle density and fluxes derived from images, as well as the relative energetic proton and electron fluxes (see below).

<sup>8</sup> Note that at small phase angles, the brightness differences for Minnaert and Lambertian scattering laws are negligible since the incidence and emission angles are nearly identical.

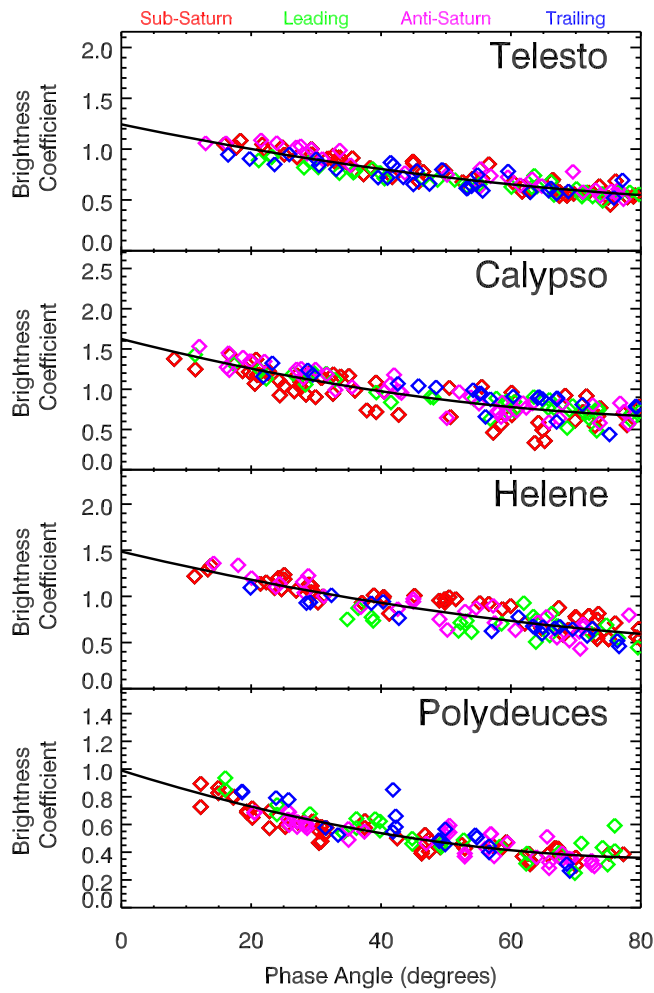
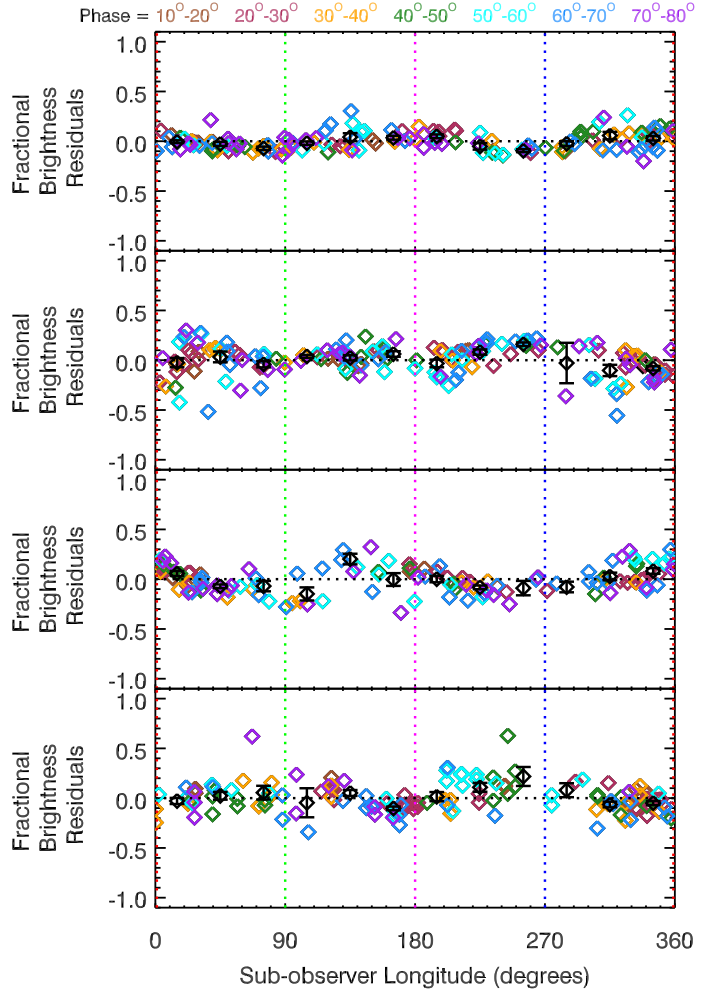


**Figure 10.** Estimated brightness coefficients for Lambertian models of Telesto, Calypso, Helene, and Polydeuces with their nominal shapes. The left plots show the brightness coefficients of the moons as a function of phase angle, with the data points color coded by the quadrant viewed by the spacecraft. The right-hand plots show the fractional residuals of the brightness estimates relative to the quadratic trend shown as a solid line in the left-hand plots. For Telesto, Calypso, and Polydeuces, this model yields reduces the dispersion associated with the viewing geometry. However, for Helene, the dispersion of the measurements around the mean trend has actually increased.

#### 4.2. Correlations Between the Moons' Brightnesses and the E Ring Particle Flux

Figure 16 shows that the brightness coefficients for the largest moons (Janus, Epimetheus, Mimas, Tethys, Dione, and Rhea) follow the same basic trends as previously reported for these moon's geometric albedos (Verbiscer et al. 2007, 2018). The brightness of these larger moons falls off with distance from Enceladus' orbit, which strongly suggests that the E-ring plays an important role in determining these moons' surface brightness. Furthermore, the leading-trailing asymmetries in these moons' surface brightness are also consistent with how E-ring particles are expected to strike the moons (Buratti et al. 1998; Schenk et al. 2011). Most of the visible E ring particles have orbital semimajor axes close to Enceladus and a range of eccentricities (Horanyi et al. 1992; Hamilton & Burns 1994). The E-ring particles outside Enceladus' orbit are therefore closer to the apocenter of their eccentric orbits and so are moving slower around the planet than the moons are. Hence, Tethys, Dione, and Rhea mostly overtake the E-ring particles, and the corresponding flux onto these moons is larger on their leading sides. On the other hand, the E-ring particles inside Enceladus' orbit are closer to their orbital pericenters, and so



tend to move faster around the planet than the moons. Hence, the E-ring particles tend to preferentially strike the trailing sides of Janus, Epimetheus, and Mimas. For all of these moons, the side that is preferentially struck by E-ring particles is brighter, as one would expect if the E-ring flux was responsible for brightening the moons.

The connection between the E-ring and the moons' brightness can be made more quantitative by estimating the flux of E-ring particles onto each of the moons. The E ring consists of particles with a wide range of orbital elements, so detailed numerical simulations will likely be needed to accurately compute the fluxes onto each moon. Such simulations are beyond the scope of this report, and so we will here simply approximate the particle flux based on simplified analytical models of the E ring motivated by the available remote-sensing and in situ observations.

Prior analyses of E-ring images obtained by the *Cassini* spacecraft provided maps of the local brightness density within this ring as functions of radius and height above Saturn's equatorial plane. These brightness densities are proportional to the local number density of particles times the size-dependent scattering efficiency for those particles, so these maps provide relatively direct estimates of the particle density in the vicinity of

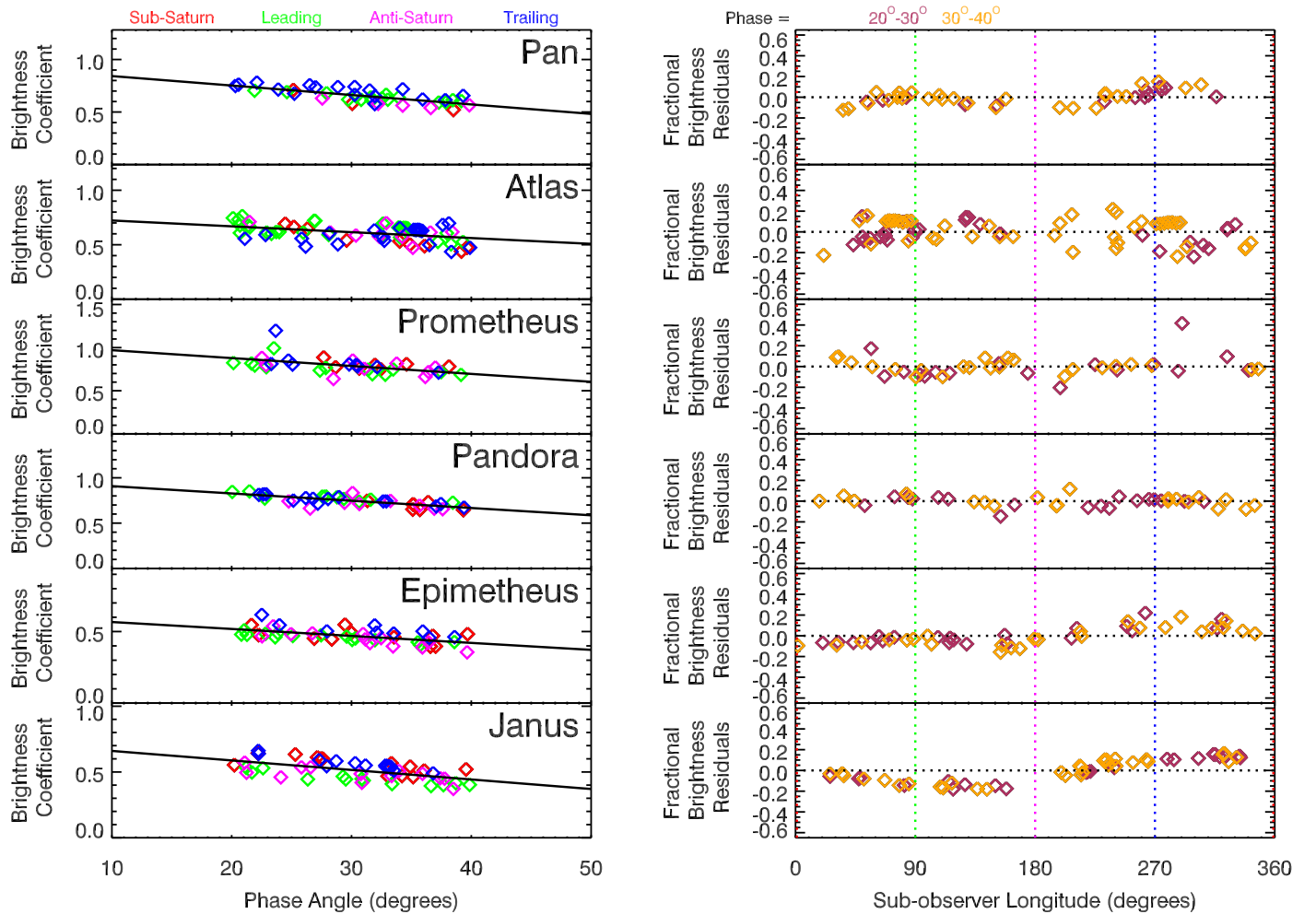


**Figure 11.** Estimated brightness coefficients for Lambertian models of the ring moons with their nominal shapes. The left plots show the brightness coefficients of the moons as a function of phase angle, with the data points color coded by the quadrant viewed by the spacecraft. The right-hand plots show the fractional residuals of the brightness estimates relative to the linear trend shown as a solid line in the left-hand plots. This model again reduces the dispersion around the phase trend, although for Atlas, the dispersion is rather high compared to the other moons. Also note that for Janus and Epimetheus, the leading hemisphere is clearly darker than the trailing hemisphere.

the moons. For this particular study, we will focus on the E-ring density profile shown in Figure 16, which is derived from the E130MAP observation made on day 137 of 2006, and is described in detail in Hedman et al. (2012). This observation included a set of wide-angle camera images that provided an extensive and high signal-to-noise edge-on map of the E ring at phase angles around  $130^\circ$  (W1526532467, W1526536067, W1526539667, W1526543267, W1526546867, W1526550467, and W1526554067). These images were assembled into a single mosaic of the edge-on ring, and then onion-peeled to transform the observed integrated brightness map into a map of the local ring brightness density in a vertical cut through the ring (Hedman et al. 2012). The profile of the brightness density near Saturn's equatorial plane was extracted from this map as the average brightness in regions between 1000 and 2000 km from Saturn's equatorial plane after removing a background level based on the average brightness 20,000–30,000 km away from that plane. Note that the region used here deliberately excluded the region within 1000 km of the equatorial plane to minimize contamination from the G ring interior to 175,000 km. The vertical scale height of the E ring is sufficiently large that including data in the 1000–2000 km range should provide a reasonable estimate of the density in the plane containing all of these moons.

Consistent with previous studies, the E-ring brightness density is strongly peaked around Enceladus' orbit. However, this profile also differs from the profiles reported elsewhere in the literature. For example, this profile is much more strongly peaked than that the profile used by Verbiscer et al. (2007). This is because the Verbiscer et al. (2007) profile was of the E-ring's vertically integrated brightness, rather than the brightness density close to the equatorial plane. The latter quantity is more sharply peaked because the E-ring's vertical thickness increases with distance from Enceladus' orbit, and because the ring is warped so that its peak brightness shifts away from Saturn's equatorial plane far from Enceladus' orbit (Kempf et al. 2008; Hedman et al. 2012; Ye et al. 2016). Since all of the moons orbit close to the planet's equatorial plane, the profile shown in Figure 16 is a better representation of the relative dust density surrounding the moons. On the other hand, the profile shown in Figure 16 is also a bit broader than in situ measurements would predict. These data have generally been fit to models where the particle density falls off with distance from Enceladus' orbit like power laws with very large indices (Kempf et al. 2008; Ye et al. 2016). Assuming that the brightness density is proportional to the particle number density, these models tend to underpredict the signals seen

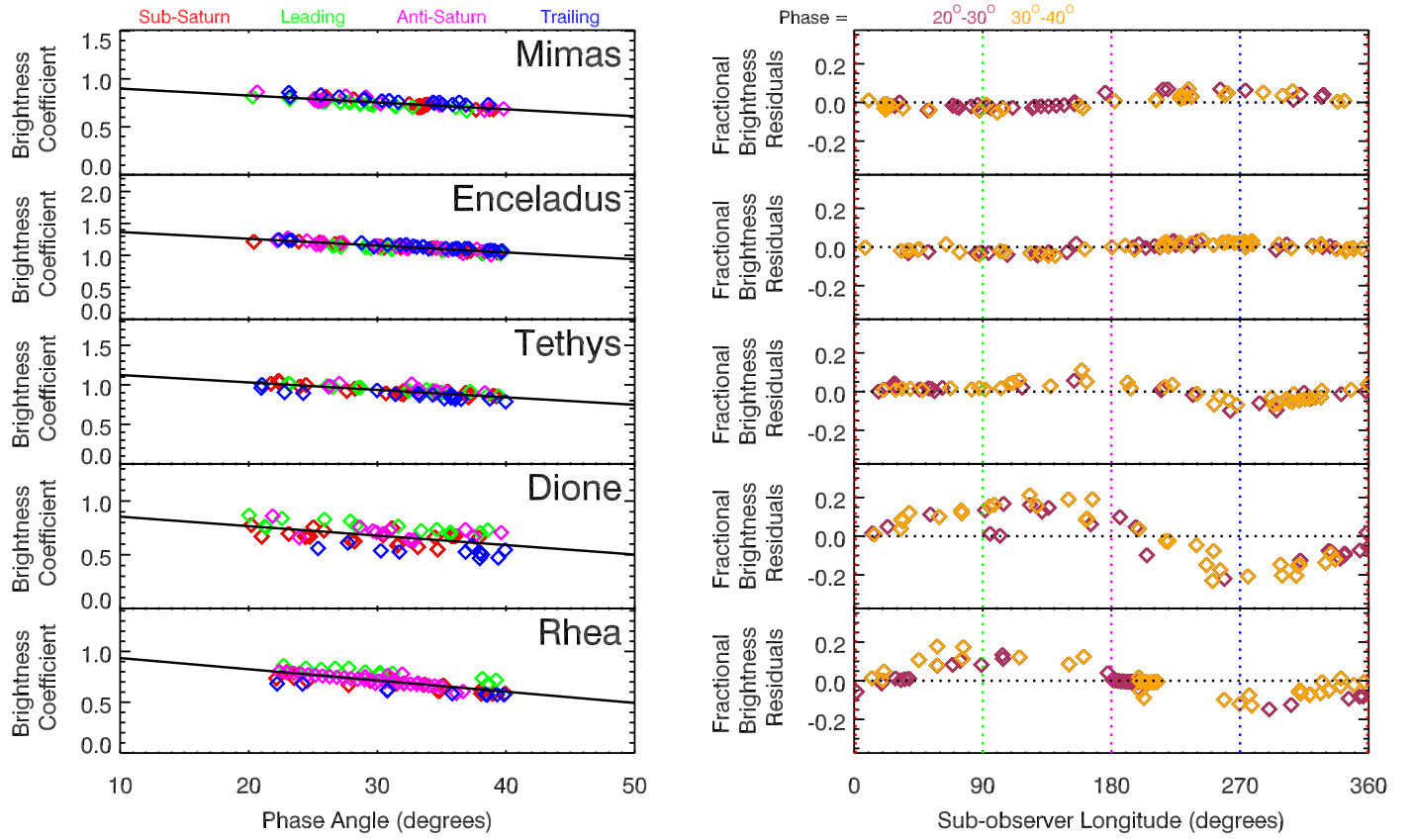


**Figure 12.** Estimated brightness coefficients for Lambertian models of the mid-sized moons with their nominal shapes. The left plot show the brightness coefficients of the moons as a function of phase angle, with the data points color coded by the quadrant viewed by the spacecraft. The right-hand plots show the fractional residuals of the brightness estimates relative to the linear trend shown as a solid line in the left-hand plots. Since all of these moons are close to spherical, the model does not affect the trends with longitude very much. Instead, this model simply enables the data for these moons to be compared with that from smaller moons. Note the longitudinal brightness asymmetries seen in these data are consistent with previous measurements and are mostly due to asymmetries in the E-ring flux.

exterior to  $5 R_S$  and interior to  $3 R_S$ . These discrepancies arise in part because the in situ instruments are only sensitive to grains with radii larger than  $0.9 \mu\text{m}$ , while the images are sensitive to somewhat smaller particles that probably have a broader spatial distribution (Horányi et al. 2008; Hedman et al. 2012). The profile shown in Figure 16 therefore should provide a reasonable estimate of the relative densities of the particles larger than  $0.5 \mu\text{m}$  across within this ring.

However, for the purposes of understanding how the E-ring affects the moons' surface properties, we are primarily interested in the E-ring particle flux into the moons, which depends not only on the particle density, but also on the particles' velocity distribution. Since a detailed investigation of the E-ring's orbital element distribution is beyond the scope of this paper, we will here consider a simple analytical model of the E-ring particles' orbital properties that can provide useful rough estimates of the particle flux into the various moons.

Prior analyses of E-ring images indicate that most of the visible particles in this ring have semimajor axes close to Enceladus' orbit, and that the large size of this ring is because the particles have a wide range of eccentricities and inclinations. Furthermore, the images indicate that mean eccentricities, inclinations, and semimajor axes were strongly correlated with each other (Hedman et al. 2012). We therefore posit that the E-ring density distribution seen in Figure 16 primarily reflects a distribution of eccentricities  $\mathcal{F}(e)$ . We also allow the semimajor axes of the particles to vary, but for the sake of simplicity, we

assume that the semimajor axes of these particles  $a$  is a strict function of  $e$ :  $a = [2400,000 + (e/0.1) \times 5000] \text{ km}$ , which is consistent with the imaging data (Hedman et al. 2012). Since we are only concerned with particles near Saturn's equatorial plane, we will not consider the inclination distributions here.

For a given eccentricity distribution  $\mathcal{F}(e)$ , the particle density as a function of radius  $d(r)$  should be given by the following integral:

$$d(r) = \int_{e_{\min}}^1 \frac{2}{|v_r|T} \mathcal{F}(e) de, \quad (16)$$

where  $v_r$  is the radial velocity of the particles and  $T$  is their orbital period, and the factor of two arises because particles with a finite eccentricity pass through each radius twice. The integral's lower limit is  $e_{\min} = |1 - r/a|$  because only particles with eccentricities greater than this can reach the observed  $r$ . Similarly, the average flux of particles onto a body on a circular orbit at a given radius is given by the integral.

$$F(r) = \int_{e_{\min}}^1 \frac{1}{2|v_r|T} \mathcal{F}(e) \sqrt{v_r^2 + \delta v_\lambda^2} de, \quad (17)$$

where  $v_r$  is the particle's radial velocity as defined above, and  $\delta v_\lambda$  is the particle's azimuthal velocity measured relative to the local circular orbital velocity. Note that a factor of one-fourth

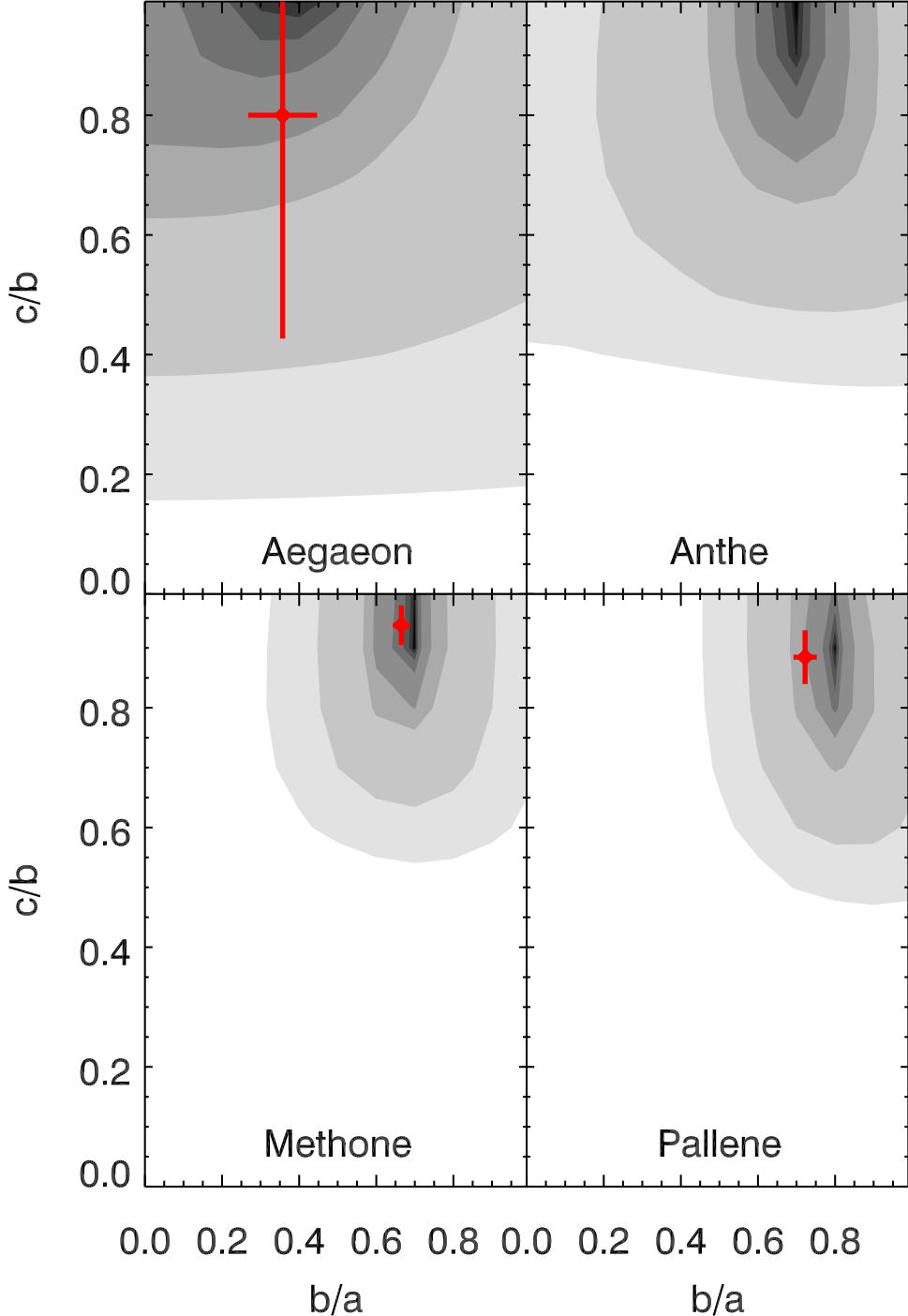


**Figure 13.** Photometric analysis of the shapes of Aegaeon, Anthe, Methone, and Pallene. Each panel shows the rms dispersion of the residuals between the photometric data and a Lambertian GEPM model with different shape parameters  $a/b$  and  $b/c$  and a quadratic  $B(a)$  function. The red data points are the estimates of these parameters derived from resolved images. For Aegaeon, Methone, and Pallene, the best-fit photometric models are reasonably consistent with the observed shapes. For Pallene, the best-fit model has a slightly higher  $b/a$  than was observed, but this can probably be attributed to the longitudinal brightness variations in this moon. These data also indicate that Methone and Anthe have very similar aspect ratios.

arises from averaging over the moon's surface. Since the radial motions of particles on any given orbit are symmetric inwards and outwards, in this model, there are no differences in the fluxes on the sub-Saturn and anti-Saturn sides of the moon. However, because the particles at a given radius can have different average azimuthal velocities, there can be asymmetries in the fluxes on the moon's leading and trailing sides.

These asymmetries can be parameterized by the following integral:

$$\delta F_\lambda(r) = \int_{e_{\min}}^1 \frac{1}{2|v_r|T} \mathcal{F}(e) \delta v_\lambda de, \quad (18)$$

which is *half* the difference between the fluxes on the leading and trailing points.

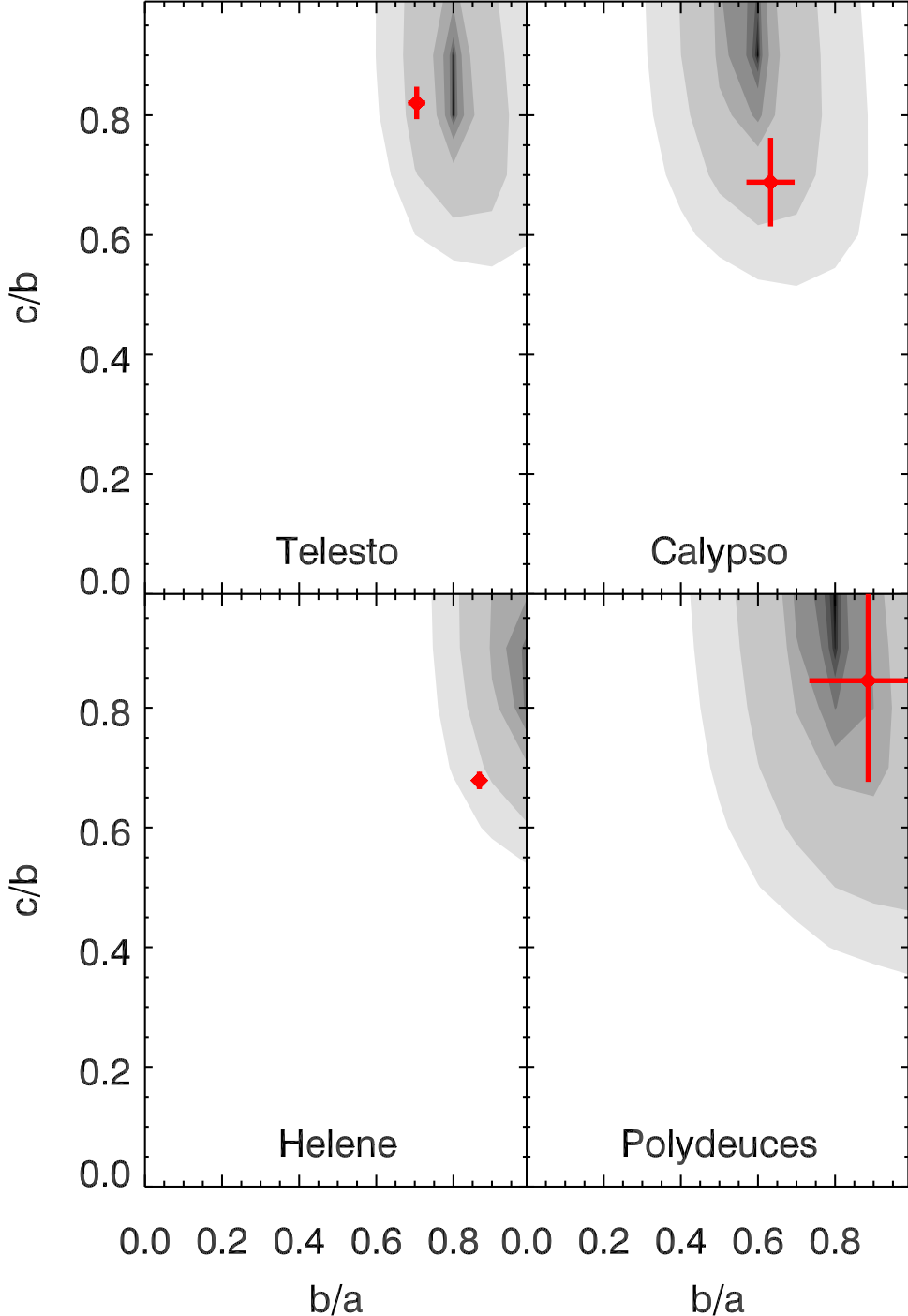


**Figure 14.** Photometric analysis of the shapes of Telesto, Calypso, Helene, and Polydeuces. Each panel shows the rms dispersion of the residuals between the photometric data and a Lambertian GEPM model with different shape parameters  $a/b$  and  $b/c$  and a quadratic  $B(\alpha)$  function. The red data points are the estimates of these parameters derived from resolved images. For Calypso and Polydeuces, the best-fit photometric models are reasonably consistent with the observed shapes. For Telesto, the best-fit model has a slightly higher  $b/a$  than was observed, and for Helene, the best-fit model has a  $b/a = 1$ .

In order to evaluate these integrals, recall the standard expressions for  $v_r$  and  $\delta v_\lambda$  in terms of orbital elements (Murray & Dermott 1999):

$$v_r = \frac{na}{\sqrt{1 - e^2}} e \sin f \quad (19)$$

$$\delta v_\lambda = \frac{na}{\sqrt{1 - e^2}} (1 + e \cos f) - na \sqrt{a/r} \quad (20)$$

where  $n = 2\pi/T$  is the mean motion of the particle and  $f$  is the true anomaly of the particle's orbit. At a given radius  $r$ , we will be observing particles at different mean anomalies given by the standard expression:

$$r = \frac{a(1 - e^2)}{1 + e \cos f} \quad (21)$$

**Table 3**  
Brightness Coefficients for Saturn's Moons Based on Data between  $20^\circ$  and  $40^\circ$  Phase Assuming a Lambertian Surface Scattering law

$B$ at $\alpha = 30^\circ$ $C_B = dB/d\alpha$ (per degree)	All Data	Sub-Saturn Quadrant	Leading Quadrant	Anti-Saturn Quadrant	Trailing Quadrant
Pan	$0.6492 \pm 0.0058 \pm 0.0142$ $-0.0071 \pm 0.0011 \pm 0.0002$	$0.6398 \pm 0.0233 \pm 0.0140$ $-0.0135 \pm 0.0041 \pm 0.0003$	$0.6314 \pm 0.0056 \pm 0.0138$ $-0.0066 \pm 0.0011 \pm 0.0001$	$0.6293 \pm 0.0126 \pm 0.0138$ $-0.0056 \pm 0.0022 \pm 0.0001$	$0.6744 \pm 0.0089 \pm 0.0148$ $-0.0042 \pm 0.0016 \pm 0.0001$
Atlas	$0.6254 \pm 0.0084 \pm 0.0084$ $-0.0055 \pm 0.0014 \pm 0.0001$	$0.5960 \pm 0.0092 \pm 0.0080$ $-0.0151 \pm 0.0015 \pm 0.0002$	$0.6475 \pm 0.0100 \pm 0.0087$ $-0.0051 \pm 0.0016 \pm 0.0001$	$0.6334 \pm 0.0242 \pm 0.0085$ $-0.0070 \pm 0.0046 \pm 0.0001$	$0.5898 \pm 0.0180 \pm 0.0079$ $0.0026 \pm 0.0031 \pm 0.0000$
Prometheus	$0.7928 \pm 0.0127 \pm 0.0130$ $-0.0083 \pm 0.0025 \pm 0.0001$	$0.8153 \pm 0.0184 \pm 0.0133$ $-0.0038 \pm 0.0048 \pm 0.0001$	$0.7550 \pm 0.0164 \pm 0.0123$ $-0.0084 \pm 0.0027 \pm 0.0001$	$0.7924 \pm 0.0236 \pm 0.0130$ $-0.0062 \pm 0.0047 \pm 0.0001$	$0.8129 \pm 0.0420 \pm 0.0133$ $-0.0168 \pm 0.0090 \pm 0.0003$
Pandora	$0.7600 \pm 0.0053 \pm 0.0057$ $-0.0072 \pm 0.0010 \pm 0.0001$	$0.7638 \pm 0.0320 \pm 0.0057$ $-0.0089 \pm 0.0054 \pm 0.0001$	$0.7704 \pm 0.0052 \pm 0.0058$ $-0.0069 \pm 0.0009 \pm 0.0001$	$0.7570 \pm 0.0225 \pm 0.0057$ $-0.0049 \pm 0.0049 \pm 0.0000$	$0.7550 \pm 0.0052 \pm 0.0057$ $-0.0073 \pm 0.0009 \pm 0.0001$
Janus	$0.5305 \pm 0.0082 \pm 0.0027$ $-0.0075 \pm 0.0015 \pm 0.0000$	$0.5726 \pm 0.0138 \pm 0.0029$ $-0.0081 \pm 0.0024 \pm 0.0000$	$0.4654 \pm 0.0055 \pm 0.0024$ $-0.0069 \pm 0.0009 \pm 0.0000$	$0.4989 \pm 0.0120 \pm 0.0026$ $-0.0057 \pm 0.0020 \pm 0.0000$	$0.5814 \pm 0.0043 \pm 0.0030$ $-0.0104 \pm 0.0010 \pm 0.0001$
Epimetheus	$0.4628 \pm 0.0060 \pm 0.0026$ $-0.0049 \pm 0.0010 \pm 0.0000$	$0.4665 \pm 0.0141 \pm 0.0026$ $-0.0041 \pm 0.0024 \pm 0.0000$	$0.4480 \pm 0.0038 \pm 0.0025$ $-0.0042 \pm 0.0006 \pm 0.0000$	$0.4422 \pm 0.0080 \pm 0.0025$ $-0.0079 \pm 0.0015 \pm 0.0000$	$0.5188 \pm 0.0103 \pm 0.0029$ $-0.0076 \pm 0.0019 \pm 0.0000$
Aegaeon	$0.1793 \pm 0.0050 \pm 0.0326$ $-0.0009 \pm 0.0009 \pm 0.0002$	$0.1648 \pm 0.0084 \pm 0.0300$ $-0.0019 \pm 0.0008 \pm 0.0003$	$0.1582 \pm 0.0042 \pm 0.0288$ $-0.0034 \pm 0.0006 \pm 0.0006$	$0.1352 \pm 0.0921 \pm 0.0246$ $-0.0086 \pm 0.0183 \pm 0.0016$	$0.2437 \pm 0.0145 \pm 0.0443$ $-0.0056 \pm 0.0022 \pm 0.0010$
Mimas	$0.7546 \pm 0.0028 \pm 0.0015$ $-0.0072 \pm 0.0006 \pm 0.0000$	$0.7533 \pm 0.0040 \pm 0.0015$ $-0.0093 \pm 0.0009 \pm 0.0000$	$0.7340 \pm 0.0016 \pm 0.0015$ $-0.0081 \pm 0.0004 \pm 0.0000$	$0.7622 \pm 0.0073 \pm 0.0015$ $-0.0079 \pm 0.0012 \pm 0.0000$	$0.7862 \pm 0.0034 \pm 0.0016$ $-0.0075 \pm 0.0007 \pm 0.0000$
18 Methone	$0.5558 \pm 0.0033 \pm 0.0115$ $-0.0058 \pm 0.0006 \pm 0.0001$	$0.5631 \pm 0.0081 \pm 0.0117$ $-0.0048 \pm 0.0003 \pm 0.0001$	$0.5529 \pm 0.0042 \pm 0.0114$ $-0.0060 \pm 0.0009 \pm 0.0001$	$0.5542 \pm 0.0083 \pm 0.0115$ $-0.0073 \pm 0.0015 \pm 0.0002$	$0.5498 \pm 0.0066 \pm 0.0114$ $-0.0049 \pm 0.0011 \pm 0.0001$
Pallene	$0.5228 \pm 0.0066 \pm 0.0164$ $-0.0071 \pm 0.0011 \pm 0.0002$	$0.5556 \pm 0.0126 \pm 0.0174$ $-0.0051 \pm 0.0005 \pm 0.0002$	$0.4660 \pm 0.0057 \pm 0.0146$ $-0.0076 \pm 0.0012 \pm 0.0002$	$0.5519 \pm 0.0114 \pm 0.0173$ $-0.0085 \pm 0.0021 \pm 0.0003$	$0.5267 \pm 0.0078 \pm 0.0165$ $-0.0052 \pm 0.0012 \pm 0.0002$
Enceladus	$1.1530 \pm 0.0029 \pm 0.0009$ $-0.0107 \pm 0.0005 \pm 0.0000$	$1.1451 \pm 0.0034 \pm 0.0009$ $-0.0104 \pm 0.0006 \pm 0.0000$	$1.1215 \pm 0.0043 \pm 0.0009$ $-0.0095 \pm 0.0010 \pm 0.0000$	$1.1580 \pm 0.0049 \pm 0.0009$ $-0.0126 \pm 0.0009 \pm 0.0000$	$1.1711 \pm 0.0034 \pm 0.0009$ $-0.0103 \pm 0.0006 \pm 0.0000$
Tethys	$0.9363 \pm 0.0046 \pm 0.0011$ $-0.0094 \pm 0.0008 \pm 0.0000$	$0.9408 \pm 0.0050 \pm 0.0011$ $-0.0103 \pm 0.0008 \pm 0.0000$	$0.9550 \pm 0.0035 \pm 0.0011$ $-0.0087 \pm 0.0007 \pm 0.0000$	$0.9704 \pm 0.0106 \pm 0.0011$ $-0.0086 \pm 0.0022 \pm 0.0000$	$0.8903 \pm 0.0067 \pm 0.0010$ $-0.0081 \pm 0.0011 \pm 0.0000$
Telesto	$0.9028 \pm 0.0100 \pm 0.0220$ $-0.0125 \pm 0.0019 \pm 0.0003$	$0.9365 \pm 0.0148 \pm 0.0228$ $-0.0088 \pm 0.0006 \pm 0.0002$	$0.8383 \pm 0.0087 \pm 0.0204$ $-0.0084 \pm 0.0014 \pm 0.0002$	$0.9671 \pm 0.0147 \pm 0.0236$ $-0.0151 \pm 0.0034 \pm 0.0004$	$0.8494 \pm 0.0216 \pm 0.0207$ $-0.0112 \pm 0.0042 \pm 0.0003$
Calypso	$1.0999 \pm 0.0176 \pm 0.0463$ $-0.0144 \pm 0.0032 \pm 0.0006$	$1.0628 \pm 0.0224 \pm 0.0448$ $-0.0123 \pm 0.0011 \pm 0.0005$	$1.1331 \pm 0.0239 \pm 0.0477$ $-0.0107 \pm 0.0045 \pm 0.0004$	$1.1645 \pm 0.0240 \pm 0.0490$ $-0.0251 \pm 0.0061 \pm 0.0011$	$1.2138 \pm 0.0712 \pm 0.0511$ $-0.0028 \pm 0.0134 \pm 0.0001$
Dione	$0.6785 \pm 0.0099 \pm 0.0005$ $-0.0088 \pm 0.0017 \pm 0.0000$	$0.6669 \pm 0.0105 \pm 0.0005$ $-0.0039 \pm 0.0020 \pm 0.0000$	$0.7634 \pm 0.0094 \pm 0.0005$ $-0.0064 \pm 0.0015 \pm 0.0000$	$0.7027 \pm 0.0151 \pm 0.0005$ $-0.0062 \pm 0.0033 \pm 0.0000$	$0.5561 \pm 0.0144 \pm 0.0004$ $-0.0049 \pm 0.0021 \pm 0.0000$
Helene	$1.0251 \pm 0.0148 \pm 0.0113$ $-0.0196 \pm 0.0027 \pm 0.0002$	$1.0807 \pm 0.0187 \pm 0.0119$ $-0.0086 \pm 0.0007 \pm 0.0001$	$0.8373 \pm 0.1644 \pm 0.0093$ $-0.0074 \pm 0.0224 \pm 0.0001$	$1.0544 \pm 0.0308 \pm 0.0117$ $-0.0169 \pm 0.0058 \pm 0.0002$	$0.9522 \pm 0.0289 \pm 0.0105$ $-0.0001 \pm 0.0064 \pm 0.0000$
Polydeuces	$0.6075 \pm 0.0089 \pm 0.0794$ $-0.0071 \pm 0.0016 \pm 0.0009$	$0.6034 \pm 0.0120 \pm 0.0789$ $-0.0073 \pm 0.0006 \pm 0.0010$	$0.6476 \pm 0.0205 \pm 0.0846$ $-0.0072 \pm 0.0030 \pm 0.0009$	$0.5945 \pm 0.0090 \pm 0.0777$ $-0.0094 \pm 0.0017 \pm 0.0012$	$0.6266 \pm 0.0121 \pm 0.0819$ $-0.0300 \pm 0.0029 \pm 0.0039$
Rhea	$0.7144 \pm 0.0057 \pm 0.0006$ $-0.0110 \pm 0.0011 \pm 0.0000$	$0.6967 \pm 0.0066 \pm 0.0005$ $-0.0109 \pm 0.0011 \pm 0.0000$	$0.7937 \pm 0.0046 \pm 0.0006$ $-0.0093 \pm 0.0009 \pm 0.0000$	$0.7146 \pm 0.0042 \pm 0.0006$ $-0.0120 \pm 0.0011 \pm 0.0000$	$0.6321 \pm 0.0031 \pm 0.0005$ $-0.0065 \pm 0.0004 \pm 0.0000$

**Note.** The first error bars are statistical, and the second are systematic errors due to uncertainties in the object's average size.

**Table 4**Brightness Coefficients for Saturn's Moons Based on Data between 20° and 40° Phase Assuming a Minnaert Surface Scattering Law with  $k = 0.75$ 

$B$ at $\alpha = 30^\circ$ $C_B = dB/d\alpha$ (per degree)	All Data	Sub-Saturn Quadrant	Leading Quadrant	Anti-Saturn Quadrant	Trailing Quadrant
Pan	0.6379 ± 0.0061 ± 0.0140 −0.0080 ± 0.0011 ± 0.0002	0.6289 ± 0.0284 ± 0.0138 −0.0152 ± 0.0050 ± 0.0003	0.6190 ± 0.0060 ± 0.0136 −0.0072 ± 0.0012 ± 0.0002	0.6166 ± 0.0144 ± 0.0135 −0.0063 ± 0.0025 ± 0.0001	0.6633 ± 0.0091 ± 0.0145 −0.0053 ± 0.0016 ± 0.0001
Atlas	0.6122 ± 0.0088 ± 0.0082 −0.0064 ± 0.0015 ± 0.0001	0.5863 ± 0.0108 ± 0.0079 −0.0174 ± 0.0018 ± 0.0002	0.6347 ± 0.0110 ± 0.0085 −0.0058 ± 0.0017 ± 0.0001	0.6126 ± 0.0215 ± 0.0082 −0.0074 ± 0.0041 ± 0.0001	0.5787 ± 0.0187 ± 0.0078 0.0016 ± 0.0032 ± 0.0000
Prometheus	0.7702 ± 0.0127 ± 0.0126 −0.0108 ± 0.0025 ± 0.0002	0.8051 ± 0.0208 ± 0.0132 −0.0114 ± 0.0054 ± 0.0002	0.7404 ± 0.0184 ± 0.0121 −0.0089 ± 0.0031 ± 0.0001	0.7668 ± 0.0236 ± 0.0125 −0.0108 ± 0.0047 ± 0.0002	0.7848 ± 0.0398 ± 0.0128 −0.0198 ± 0.0086 ± 0.0003
Pandora	0.7498 ± 0.0052 ± 0.0056 −0.0075 ± 0.0010 ± 0.0001	0.7639 ± 0.0299 ± 0.0057 −0.0102 ± 0.0051 ± 0.0001	0.7577 ± 0.0061 ± 0.0057 −0.0073 ± 0.0011 ± 0.0001	0.7397 ± 0.0220 ± 0.0055 −0.0048 ± 0.0048 ± 0.0000	0.7481 ± 0.0059 ± 0.0056 −0.0078 ± 0.0011 ± 0.0001
Janus	0.5257 ± 0.0084 ± 0.0027 −0.0077 ± 0.0015 ± 0.0000	0.5692 ± 0.0142 ± 0.0029 −0.0085 ± 0.0025 ± 0.0000	0.4595 ± 0.0054 ± 0.0024 −0.0070 ± 0.0009 ± 0.0000	0.4924 ± 0.0115 ± 0.0025 −0.0058 ± 0.0019 ± 0.0000	0.5777 ± 0.0051 ± 0.0030 −0.0107 ± 0.0012 ± 0.0001
Epimetheus	0.4588 ± 0.0060 ± 0.0026 −0.0051 ± 0.0011 ± 0.0000	0.4651 ± 0.0145 ± 0.0026 −0.0043 ± 0.0024 ± 0.0000	0.4433 ± 0.0039 ± 0.0025 −0.0045 ± 0.0006 ± 0.0000	0.4375 ± 0.0078 ± 0.0025 −0.0083 ± 0.0015 ± 0.0000	0.5136 ± 0.0105 ± 0.0029 −0.0078 ± 0.0019 ± 0.0000
Aegaeon	0.1758 ± 0.0049 ± 0.0320 −0.0008 ± 0.0008 ± 0.0001	0.1620 ± 0.0079 ± 0.0295 −0.0016 ± 0.0008 ± 0.0003	0.1512 ± 0.0042 ± 0.0275 −0.0037 ± 0.0006 ± 0.0007	0.1323 ± 0.0039 ± 0.0241 −0.0099 ± 0.0186 ± 0.0018	0.2386 ± 0.0138 ± 0.0434 −0.0054 ± 0.0021 ± 0.0010
Mimas	0.7498 ± 0.0028 ± 0.0015 −0.0073 ± 0.0006 ± 0.0000	0.7506 ± 0.0038 ± 0.0015 −0.0094 ± 0.0008 ± 0.0000	0.7285 ± 0.0015 ± 0.0015 −0.0082 ± 0.0004 ± 0.0000	0.7576 ± 0.0076 ± 0.0015 −0.0082 ± 0.0013 ± 0.0000	0.7796 ± 0.0037 ± 0.0016 −0.0076 ± 0.0008 ± 0.0000
Methone	0.5508 ± 0.0035 ± 0.0114 −0.0070 ± 0.0007 ± 0.0001	0.5663 ± 0.0087 ± 0.0117 −0.0050 ± 0.0003 ± 0.0001	0.5488 ± 0.0043 ± 0.0114 −0.0064 ± 0.0009 ± 0.0001	0.5423 ± 0.0073 ± 0.0112 −0.0090 ± 0.0014 ± 0.0002	0.5415 ± 0.0074 ± 0.0112 −0.0064 ± 0.0013 ± 0.0001
Pallene	0.5181 ± 0.0064 ± 0.0163 −0.0077 ± 0.0011 ± 0.0002	0.5537 ± 0.0127 ± 0.0174 −0.0052 ± 0.0005 ± 0.0002	0.4622 ± 0.0050 ± 0.0145 −0.0078 ± 0.0010 ± 0.0002	0.5468 ± 0.0097 ± 0.0172 −0.0095 ± 0.0018 ± 0.0003	0.5210 ± 0.0065 ± 0.0164 −0.0058 ± 0.0010 ± 0.0002
Enceladus	1.1462 ± 0.0029 ± 0.0009 −0.0110 ± 0.0005 ± 0.0000	1.1391 ± 0.0035 ± 0.0009 −0.0108 ± 0.0006 ± 0.0000	1.1146 ± 0.0043 ± 0.0009 −0.0099 ± 0.0010 ± 0.0000	1.1511 ± 0.0048 ± 0.0009 −0.0130 ± 0.0009 ± 0.0000	1.1639 ± 0.0035 ± 0.0009 −0.0106 ± 0.0006 ± 0.0000
Tethys	0.9311 ± 0.0046 ± 0.0011 −0.0096 ± 0.0008 ± 0.0000	0.9360 ± 0.0049 ± 0.0011 −0.0105 ± 0.0008 ± 0.0000	0.9494 ± 0.0035 ± 0.0011 −0.0090 ± 0.0007 ± 0.0000	0.9645 ± 0.0108 ± 0.0011 −0.0087 ± 0.0023 ± 0.0000	0.8849 ± 0.0065 ± 0.0010 −0.0083 ± 0.0010 ± 0.0000
Telesto	0.8915 ± 0.0103 ± 0.0217 −0.0134 ± 0.0019 ± 0.0003	0.9298 ± 0.0150 ± 0.0227 −0.0085 ± 0.0006 ± 0.0002	0.8245 ± 0.0067 ± 0.0201 −0.0094 ± 0.0011 ± 0.0002	0.9545 ± 0.0162 ± 0.0233 −0.0169 ± 0.0037 ± 0.0004	0.8341 ± 0.0185 ± 0.0203 −0.0107 ± 0.0036 ± 0.0003
Calypso	1.0928 ± 0.0196 ± 0.0460 −0.0143 ± 0.0035 ± 0.0006	1.0672 ± 0.0257 ± 0.0449 −0.0125 ± 0.0012 ± 0.0005	1.1091 ± 0.0336 ± 0.0467 −0.0126 ± 0.0064 ± 0.0005	1.1360 ± 0.0286 ± 0.0478 −0.0226 ± 0.0073 ± 0.0010	1.2102 ± 0.0790 ± 0.0510 −0.0026 ± 0.0148 ± 0.0001
Dione	0.6747 ± 0.0098 ± 0.0005 −0.0090 ± 0.0017 ± 0.0000	0.6631 ± 0.0104 ± 0.0005 −0.0041 ± 0.0020 ± 0.0000	0.7591 ± 0.0093 ± 0.0005 −0.0066 ± 0.0015 ± 0.0000	0.6987 ± 0.0151 ± 0.0005 −0.0063 ± 0.0032 ± 0.0000	0.5530 ± 0.0142 ± 0.0004 −0.0051 ± 0.0020 ± 0.0000
Helene	1.0163 ± 0.0150 ± 0.0112 −0.0201 ± 0.0027 ± 0.0002	1.0758 ± 0.0184 ± 0.0119 −0.0088 ± 0.0007 ± 0.0001	0.8208 ± 0.02026 ± 0.0091 −0.0081 ± 0.0276 ± 0.0001	1.0479 ± 0.0289 ± 0.0116 −0.0153 ± 0.0054 ± 0.0002	0.9473 ± 0.0256 ± 0.0105 −0.0012 ± 0.0057 ± 0.0000
Polydeuces	0.6016 ± 0.0090 ± 0.0786 −0.0074 ± 0.0016 ± 0.0010	0.6016 ± 0.0121 ± 0.0786 −0.0075 ± 0.0006 ± 0.0010	0.6375 ± 0.0212 ± 0.0833 −0.0071 ± 0.0031 ± 0.0009	0.5867 ± 0.0087 ± 0.0767 −0.0099 ± 0.0017 ± 0.0013	0.6201 ± 0.0090 ± 0.0811 −0.0310 ± 0.0022 ± 0.0041
Rhea	0.7104 ± 0.0056 ± 0.0006 −0.0112 ± 0.0011 ± 0.0000	0.6928 ± 0.0066 ± 0.0005 −0.0111 ± 0.0011 ± 0.0000	0.7894 ± 0.0046 ± 0.0006 −0.0094 ± 0.0008 ± 0.0000	0.7106 ± 0.0042 ± 0.0006 −0.0121 ± 0.0011 ± 0.0000	0.6286 ± 0.0031 ± 0.0005 −0.0067 ± 0.0004 ± 0.0000

**Note.** The first error bars are statistical, and the second are systematic errors due to uncertainties in the object's average size.

**Table 5**Brightness Coefficients for Saturn's Moons Based on Data between 20° and 40° Phase Assuming a Minnaert Surface Scattering Law with  $k = 0.50$ 

$B$ at $\alpha = 30^\circ$ $C_B = dB/d\alpha$ (per degree)	All Data	Sub-Saturn Quadrant	Leading Quadrant	Anti-Saturn Quadrant	Trailing Quadrant
Pan	0.6181 ± 0.0066 ± 0.0135 −0.0093 ± 0.0012 ± 0.0002	0.6099 ± 0.0346 ± 0.0134 −0.0174 ± 0.0061 ± 0.0004	0.5976 ± 0.0068 ± 0.0131 −0.0079 ± 0.0013 ± 0.0002	0.5935 ± 0.0172 ± 0.0130 −0.0072 ± 0.0030 ± 0.0002	0.6444 ± 0.0099 ± 0.0141 −0.0067 ± 0.0018 ± 0.0001
Atlas	0.5903 ± 0.0095 ± 0.0079 −0.0075 ± 0.0016 ± 0.0001	0.5682 ± 0.0141 ± 0.0076 −0.0202 ± 0.0024 ± 0.0003	0.6134 ± 0.0124 ± 0.0082 −0.0066 ± 0.0019 ± 0.0001	0.5808 ± 0.0207 ± 0.0078 −0.0080 ± 0.0039 ± 0.0001	0.5595 ± 0.0201 ± 0.0075 0.0006 ± 0.0034 ± 0.0000
Prometheus	0.7362 ± 0.0130 ± 0.0120 −0.0138 ± 0.0025 ± 0.0002	0.7796 ± 0.0255 ± 0.0128 −0.0192 ± 0.0066 ± 0.0003	0.7167 ± 0.0207 ± 0.0117 −0.0096 ± 0.0035 ± 0.0002	0.7280 ± 0.0242 ± 0.0119 −0.0160 ± 0.0048 ± 0.0003	0.7486 ± 0.0375 ± 0.0122 −0.0225 ± 0.0081 ± 0.0004
Pandora	0.7299 ± 0.0057 ± 0.0055 −0.0082 ± 0.0010 ± 0.0001	0.7540 ± 0.0330 ± 0.0057 −0.0118 ± 0.0056 ± 0.0001	0.7349 ± 0.0072 ± 0.0055 −0.0082 ± 0.0013 ± 0.0001	0.7105 ± 0.0217 ± 0.0053 −0.0051 ± 0.0047 ± 0.0000	0.7329 ± 0.0074 ± 0.0055 −0.0086 ± 0.0013 ± 0.0001
Janus	0.5143 ± 0.0086 ± 0.0026 −0.0082 ± 0.0015 ± 0.0000	0.5589 ± 0.0146 ± 0.0029 −0.0091 ± 0.0026 ± 0.0000	0.4478 ± 0.0055 ± 0.0023 −0.0074 ± 0.0009 ± 0.0000	0.4791 ± 0.0110 ± 0.0025 −0.0061 ± 0.0018 ± 0.0000	0.5672 ± 0.0060 ± 0.0029 −0.0112 ± 0.0014 ± 0.0001
Epimetheus	0.4494 ± 0.0061 ± 0.0025 −0.0056 ± 0.0011 ± 0.0000	0.4579 ± 0.0149 ± 0.0026 −0.0047 ± 0.0025 ± 0.0000	0.4336 ± 0.0040 ± 0.0024 −0.0050 ± 0.0007 ± 0.0000	0.4272 ± 0.0075 ± 0.0024 −0.0088 ± 0.0014 ± 0.0000	0.5027 ± 0.0108 ± 0.0028 −0.0082 ± 0.0020 ± 0.0000
Aegaeon	0.1712 ± 0.0048 ± 0.0311 −0.0007 ± 0.0008 ± 0.0001	0.1578 ± 0.0077 ± 0.0287 −0.0015 ± 0.0008 ± 0.0003	0.1440 ± 0.0044 ± 0.0262 −0.0040 ± 0.0007 ± 0.0007	0.1245 ± 0.0952 ± 0.0226 −0.0119 ± 0.0189 ± 0.0022	0.2322 ± 0.0132 ± 0.0422 −0.0053 ± 0.0020 ± 0.0010
Mimas	0.7362 ± 0.0028 ± 0.0015 −0.0077 ± 0.0006 ± 0.0000	0.7391 ± 0.0036 ± 0.0015 −0.0099 ± 0.0008 ± 0.0000	0.7147 ± 0.0015 ± 0.0014 −0.0085 ± 0.0004 ± 0.0000	0.7438 ± 0.0079 ± 0.0015 −0.0088 ± 0.0013 ± 0.0000	0.7640 ± 0.0041 ± 0.0015 −0.0080 ± 0.0008 ± 0.0000
Methone	0.5396 ± 0.0043 ± 0.0112 −0.0085 ± 0.0008 ± 0.0002	0.5621 ± 0.0102 ± 0.0116 −0.0054 ± 0.0004 ± 0.0001	0.5395 ± 0.0056 ± 0.0112 −0.0072 ± 0.0011 ± 0.0001	0.5228 ± 0.0073 ± 0.0108 −0.0109 ± 0.0013 ± 0.0002	0.5282 ± 0.0086 ± 0.0109 −0.0080 ± 0.0015 ± 0.0002
Pallene	0.5070 ± 0.0063 ± 0.0159 −0.0086 ± 0.0011 ± 0.0003	0.5436 ± 0.0134 ± 0.0171 −0.0055 ± 0.0005 ± 0.0002	0.4538 ± 0.0049 ± 0.0142 −0.0080 ± 0.0010 ± 0.0003	0.5336 ± 0.0087 ± 0.0168 −0.0107 ± 0.0016 ± 0.0003	0.5098 ± 0.0057 ± 0.0160 −0.0066 ± 0.0009 ± 0.0002
Enceladus	1.1264 ± 0.0029 ± 0.0009 −0.0120 ± 0.0005 ± 0.0000	1.1200 ± 0.0036 ± 0.0009 −0.0118 ± 0.0007 ± 0.0000	1.0949 ± 0.0044 ± 0.0009 −0.0107 ± 0.0010 ± 0.0000	1.1310 ± 0.0048 ± 0.0009 −0.0139 ± 0.0008 ± 0.0000	1.1433 ± 0.0036 ± 0.0009 −0.0115 ± 0.0006 ± 0.0000
Tethys	0.9152 ± 0.0045 ± 0.0010 −0.0103 ± 0.0008 ± 0.0000	0.9205 ± 0.0048 ± 0.0010 −0.0112 ± 0.0008 ± 0.0000	0.9330 ± 0.0034 ± 0.0011 −0.0097 ± 0.0006 ± 0.0000	0.9474 ± 0.0109 ± 0.0011 −0.0093 ± 0.0023 ± 0.0000	0.8694 ± 0.0063 ± 0.0010 −0.0089 ± 0.0010 ± 0.0000
Telesto	0.8680 ± 0.0107 ± 0.0212 −0.0144 ± 0.0020 ± 0.0004	0.9083 ± 0.0154 ± 0.0222 −0.0086 ± 0.0006 ± 0.0002	0.8019 ± 0.0064 ± 0.0196 −0.0106 ± 0.0010 ± 0.0003	0.9258 ± 0.0201 ± 0.0226 −0.0193 ± 0.0047 ± 0.0005	0.8096 ± 0.0149 ± 0.0197 −0.0103 ± 0.0029 ± 0.0003
Calypso	1.0692 ± 0.0227 ± 0.0450 −0.0142 ± 0.0041 ± 0.0006	1.0550 ± 0.0296 ± 0.0444 −0.0128 ± 0.0014 ± 0.0005	1.0738 ± 0.0437 ± 0.0452 −0.0150 ± 0.0083 ± 0.0006	1.0868 ± 0.0374 ± 0.0458 −0.0196 ± 0.0095 ± 0.0008	1.1901 ± 0.0861 ± 0.0501 −0.0032 ± 0.0162 ± 0.0001
Dione	0.6632 ± 0.0097 ± 0.0005 −0.0094 ± 0.0017 ± 0.0000	0.6517 ± 0.0103 ± 0.0005 −0.0046 ± 0.0019 ± 0.0000	0.7462 ± 0.0092 ± 0.0005 −0.0072 ± 0.0014 ± 0.0000	0.6868 ± 0.0149 ± 0.0005 −0.0069 ± 0.0032 ± 0.0000	0.5435 ± 0.0139 ± 0.0004 −0.0055 ± 0.0020 ± 0.0000
Helene	0.9935 ± 0.0151 ± 0.0110 −0.0204 ± 0.0028 ± 0.0002	1.0543 ± 0.0174 ± 0.0116 −0.0094 ± 0.0007 ± 0.0001	0.7958 ± 0.2351 ± 0.0088 −0.0090 ± 0.0320 ± 0.0001	1.0264 ± 0.0275 ± 0.0113 −0.0139 ± 0.0052 ± 0.0002	0.9315 ± 0.0215 ± 0.0103 −0.0029 ± 0.0048 ± 0.0000
Polydeuces	0.5879 ± 0.0090 ± 0.0769 −0.0079 ± 0.0016 ± 0.0010	0.5925 ± 0.0123 ± 0.0774 −0.0079 ± 0.0006 ± 0.0010	0.6206 ± 0.0215 ± 0.0811 −0.0073 ± 0.0032 ± 0.0010	0.5705 ± 0.0084 ± 0.0746 −0.0106 ± 0.0016 ± 0.0014	0.6065 ± 0.0060 ± 0.0793 −0.0322 ± 0.0014 ± 0.0042
Rhea	0.6984 ± 0.0055 ± 0.0005 −0.0116 ± 0.0011 ± 0.0000	0.6811 ± 0.0065 ± 0.0005 −0.0115 ± 0.0011 ± 0.0000	0.7760 ± 0.0044 ± 0.0006 −0.0100 ± 0.0008 ± 0.0000	0.6985 ± 0.0041 ± 0.0005 −0.0126 ± 0.0011 ± 0.0000	0.6179 ± 0.0031 ± 0.0005 −0.0071 ± 0.0004 ± 0.0000

**Note.** The first error bars are statistical, and the second are systematic errors due to uncertainties in the object's average size.

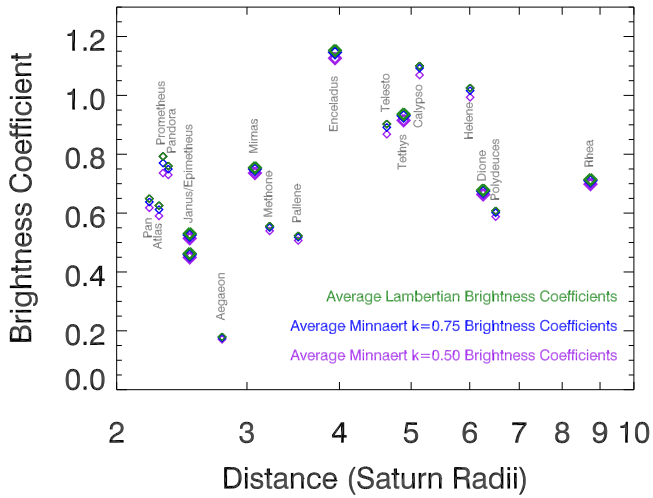


**Figure 15.** Comparisons of the average brightness coefficients of the various moons derived assuming different Minnaert scattering laws (see also Tables 3–5). While models assuming lower values of  $k$  do yield systematically lower brightness coefficients, the differences between the different models are fairly subtle and do not alter the trends among the different moons.

so we can re-express  $|v_r|$  and  $\delta v_\lambda$  in terms of  $r$

$$|v_r| = \frac{na^2}{r} \sqrt{e^2 - (r/a - 1)^2}, \quad (22)$$

$$\delta v_\lambda = \frac{na^2}{r} [\sqrt{1 - e^2} - \sqrt{r/a}]. \quad (23)$$

Inserting these expressions into the above integrals, we find the density, flux, and flux asymmetries can all be expressed as the following integrals over the eccentricity distribution (remember that  $a$  is implicitly a function of  $e$ ):

$$d(r) = \int_{e_{\min}}^1 \frac{r \mathcal{F}(e)}{\pi a^2 \sqrt{e^2 - (r/a - 1)^2}} de, \quad (24)$$

$$F(r) = \int_{e_{\min}}^1 \frac{n \mathcal{F}(e)}{4\pi} \sqrt{1 + \frac{(\sqrt{1 - e^2} - \sqrt{r/a})^2}{e^2 - (r/a - 1)^2}} de, \quad (25)$$

$$F_\lambda(r) = \int_{e_{\min}}^1 \frac{n \mathcal{F}(e)(\sqrt{1 - e^2} - \sqrt{r/a})}{4\pi \sqrt{e^2 - (r/a - 1)^2}} de. \quad (26)$$

It turns out that the observed density distribution shown in Figure 16 can be matched reasonably well by assuming the eccentricity is a Lorentzian times a regularization term to avoid singularities at  $e = 0$ :

$$\mathcal{F}(e) = \frac{\mathcal{F}_0}{1 + e^2/e_0^2} [1 - \exp(-e/e_c)] \quad (27)$$

with constants  $\mathcal{F}_0$ ,  $e_0$ , and  $e_c$ . The specific model density distribution shown in Figure 16 has  $e_0 = 0.17$  and  $e_c = 0.01$ . Note that  $e_c$  basically only affects the density levels close to Enceladus’ orbit, while  $e_0$  determines how quickly the signal falls off away from the E-ring core.

Using this same ansatz for  $\mathcal{F}(e)$ , we obtain estimates for how both the flux and flux asymmetry vary with radius, which are shown in the third panel of Figure 16. First, note that the flux is much less sharply peaked than the density. This occurs because the particles are moving faster relative to the local circular velocity at larger distances from Enceladus’ orbit thanks to

their higher eccentricities. Also note that azimuthal component of the flux is larger exterior to Enceladus’ orbit than it is interior to that moon. This asymmetry arises because exterior to Enceladus, the particles are all moving slower than the local circular velocity, while interior to Enceladus, the particles are all moving faster than the local circular speed, but the azimuthal components of their velocity can still fall below the local circular velocity depending on their true anomaly.

Finally, we can translate these trends in the relative flux into rough estimates of the absolute flux of E-ring particles using recent in situ measurements of the particle number density in the E-ring core. In principle, the brightness density seen in images can be translated into estimates of the particle number density, but in practice, the relevant conversion factor depends on the size-dependent light scattering efficiency of the particles. By contrast, the peak E-ring particle density has been directly measured to be between 0.02 and 0.2 m<sup>-3</sup> with various in situ measurements (Kempf et al. 2008; Ye et al. 2016). Now, as mentioned above, these densities are for the particles larger than the detection thresholds of these instruments, which is slightly larger than the sizes of the particles seen in remote-sensing images. Hence, the number density of visible particles could be somewhat larger than these measurements. Nevertheless, these are still the best estimates of the absolute particle density near the core of the E ring, and they should still provide a useful order-of-magnitude estimate of the visible particles. For the sake of concreteness, we will here assume a peak number density of 0.03 particles m<sup>-3</sup>, which is the value measured by Ye et al. (2016) for particles larger than 1 μm in radius.

Figure 17 and Table 6 give the brightness coefficients and estimated E-ring particle fluxes for all of the moons known to be embedded in the E ring. For the mid-sized moons and the co-orbitals, there is a very good correlation between the moon’s brightness coefficients and the estimated fluxes. This correlation not only applies to the average values for each moon but also to their leading and trailing sides, where the estimated flux values are taken to be  $F \pm \delta F_\lambda/\sqrt{2}$  (the factor of  $\sqrt{2}$  accounts for the fact that the observations span a full quadrant of each body). The one mid-sized moon that falls noticeably off the main trend is Rhea. This could be related to other unusual aspects of Rhea’s surface. Rhea’s visible spectrum is redder than any of the other mid-sized moons (Thomas et al. 2018), and its near-infrared spectrum exhibits stronger ice bands than Dione (Filacchione et al. 2012; Scipioni et al. 2014). Furthermore, radio-wave data indicate that Rhea has a higher albedo at centimeter wavelengths than Dione (Black et al. 2007; Le Gall et al. 2019). Various explanations have been put forward to these anomalies, including differences in the moons’ regolith structure (Ostro et al. 2010) and variations in the energetic particle and/or ring particle flux (Scipioni et al. 2014; Thomas et al. 2018). The latter option is probably the more likely explanation for Rhea’s excess brightness at visible wavelengths, since the moon is in a region where both the predicted fluxes of E-ring grains and energetic particles are expected to be very low (see also below). Indeed, our simple E-ring model is probably not completely accurate near Rhea’s orbit. Detailed numerical simulations of the E-ring particles reveal that there could be a population of sub-micron particles orbiting in the outskirts of the E ring close to Rhea’s orbit (Horányi et al. 2008). This population could potentially increase the particle flux into Rhea, moving that data point

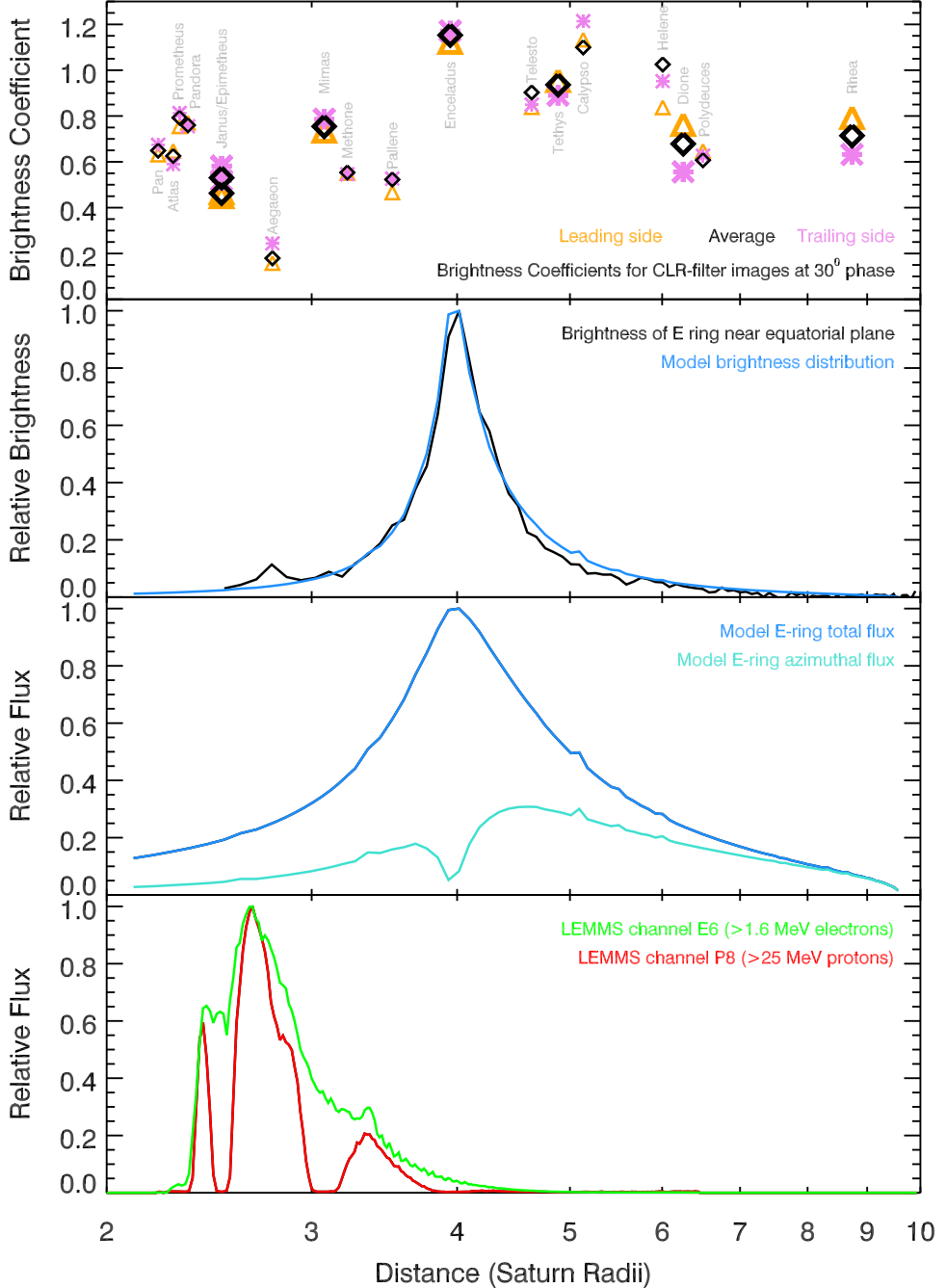


**Figure 16.** Correlations between the moon’s brightness and their environment. The top panel shows the brightness coefficients of the moons computed assuming a Lambertian scattering law as a function of distance from the planet’s center. Note that the locations of the trojan moons Telesto, Calypso, Polydeuces, and Helene are offset slightly for the sake of clarity. The next two panels show the E-ring’s relative brightness density and the relative flux of E-ring particles into the moons (i.e., the parameters  $F$  and  $|SF_L|$ ; see the text). The bottom panel shows the flux of high-energy protons and electrons derived by the MIMI LEMMS instrument from one early pass through this entire region.

closer to the trend defined by Mimas and Dione, but it is not clear whether it could also explain that moon’s spectral properties. In any case, overall, these data confirm that the E-ring particle flux is an important factor for determining the surface brightness of the mid-sized and co-orbital satellites.

Turning to the smaller moons, however, the situation is more complicated. Two of the co-orbital moons—Telesto and Polydeuces—fall close to the same trend as their larger companions. However, the other two co-orbitals—Calypso and Helene—fall noticeably above this trend. Meanwhile, Aegaeon, Methone, and Pallene all fall well below the trend for

the mid-sized moons. This implies that something besides the E-ring flux is affecting the brightnesses of these small moons.

#### 4.3. Darkening Aegaeon, Methone, and Pallene with Radiation

Aegaeon, Methone, and Pallene are all considerably darker than one would have predicted given their locations and the observed trend between Janus, Epimetheus, Mimas, and Enceladus. Aegaeon in particular is exceptionally dark, with a surface brightness coefficient around 0.2. This conclusion is consistent with the few resolved images of these bodies, which

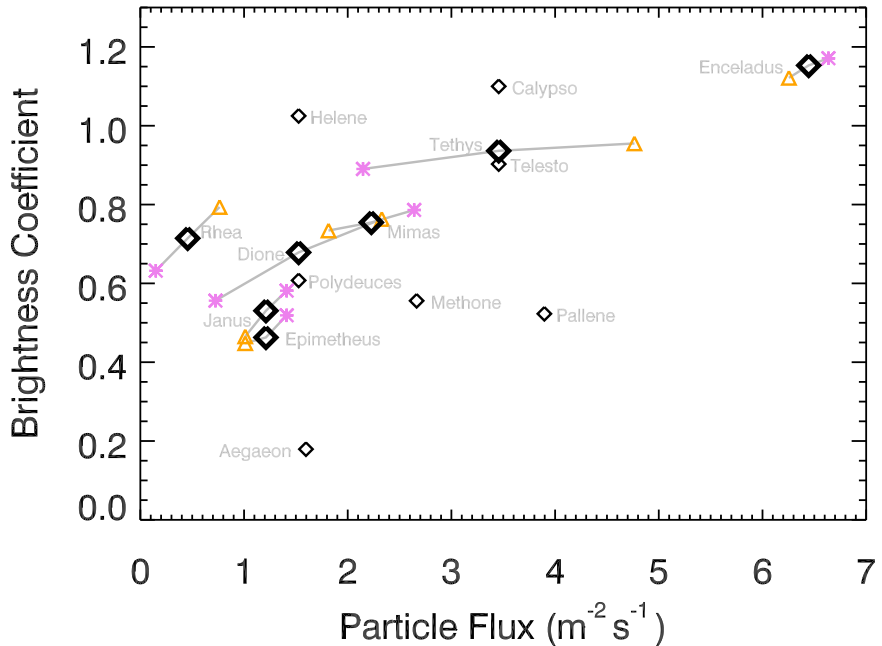


**Figure 17.** Moon brightness coefficients vs. computed E-ring particle flux, assuming peak number density of  $0.03 \text{ m}^{-3}$ ,  $e_0 = 0.17$  and  $e_{\min} = 0.01$ . The diamonds are the average values for each moon, while the orange triangles and magenta stars indicate the values for the leading and trailing sides of the mid-sized moons.

**Table 6**  
Particle and Radiation Fluxes

Moon	$B_0^{\text{a}}$			E-ring Flux <sup>b</sup>			Radiation Flux <sup>c</sup> (protons $\text{cm}^{-2} \text{s}^{-1}$ ) in range 25–59 MeV
	Ave.	Lead	Trail	Ave.	Lead	Trail	
Janus	0.53	0.47	0.58	1.21	1.01	1.41	5.4
Epimetheus	0.46	0.45	0.52	1.21	1.01	1.41	7.4
Aegaeon	0.18	0.16	0.24	1.60	1.32	1.88	920.4
Mimas	0.75	0.73	0.79	2.23	1.81	2.64	5.6
Methone	0.56	0.55	0.55	2.66	2.15	3.17	140.2
Pallene	0.53	0.47	0.53	3.89	3.19	4.60	162.0
Enceladus	1.15	1.12	1.17	6.44	6.25	6.63	4.4
Tethys	0.94	0.96	0.89	3.46	4.77	2.15	3.2
Telesto	0.90	0.84	0.84	3.46	4.77	2.15	3.2
Calypso	1.10	1.13	1.21	3.46	4.77	2.15	3.2
Dione	0.68	0.76	0.56	1.53	2.33	0.72	3.1
Helene	1.02	0.84	0.95	1.53	2.33	0.72	3.1
Polydeuces	0.61	0.65	0.63	1.53	2.33	0.72	3.1
Rhea <sup>d</sup>	0.71	0.79	0.63	0.46	0.76	0.15	3.1

#### Notes.

<sup>a</sup> Brightness coefficient at  $30^\circ$  computed assuming surface follows Lambertian scattering law, see Table 3.

<sup>b</sup> E-ring flux computed assuming  $e_0 = 0.17$ ,  $e_c = 0.01$  and a peak number density of  $0.03$  particles per cubic meter. Leading and trailing side values given by  $F \pm \delta F_\lambda / \sqrt{2}$ .

<sup>c</sup> Radiation fluxes computed assuming  $\pi$  steradian viewing angle.

<sup>d</sup> Radiation fluxes at Rhea assumed to be the same as those for Dione.

show that only the dark side of Iapetus has a comparably low surface brightness as Aegaeon (see Figure 18). In principle, the darkness of these moons could be due to a number of different factors, including their small size and their associations with other dusty rings, but the most likely explanation involves their locations within Saturn's radiation belts.

Aegaeon, Methone, and Pallene are much smaller than the mid-sized moons, and so their small sizes could somehow be responsible for their low surface brightness. Indeed, based on preliminary investigations of Aegaeon's low surface

brightness, Hedman et al. (2010) suggested that a recent collision catastrophically disrupted the body, stripping off its bright outer layers to produce the debris that is now the G ring and leaving behind a dark remnant. Deeper examination, however, does not support this model. For example, if a collision was sufficient to expose the dark core of a kilometer-scale body, then small impacts should expose dark materials on the other moons, but no such dark patches have been seen in any of the high-resolution images obtained by *Cassini*. More fundamentally, attributing Aegaeon's extreme darkness to

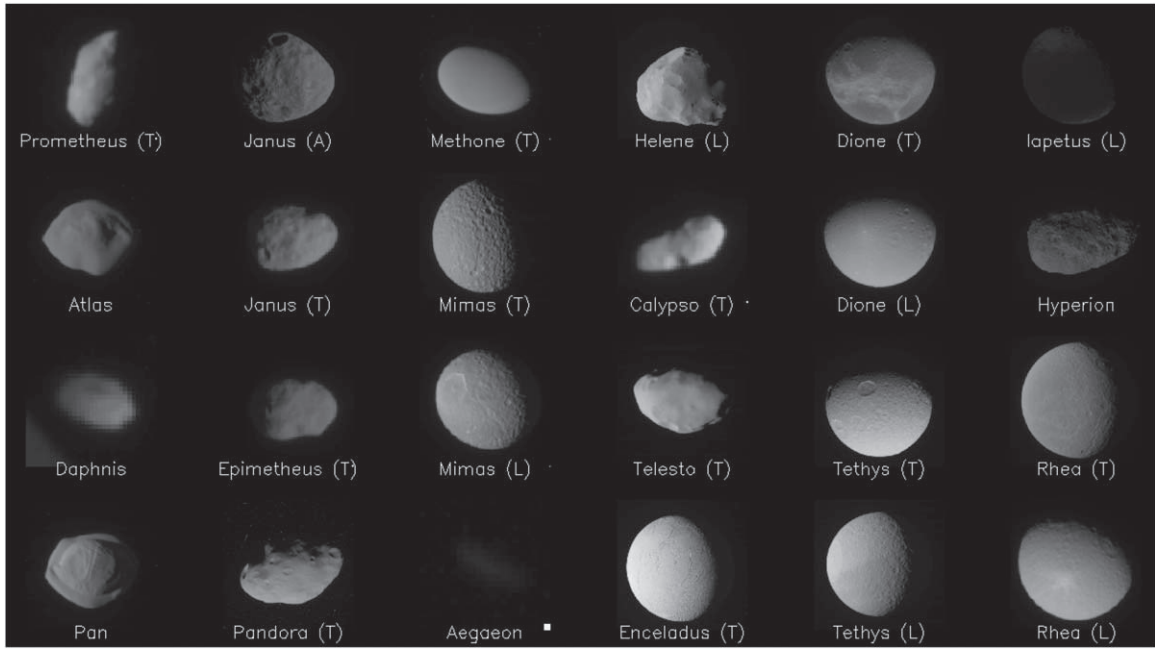


**Figure 18.** Resolved images of Saturn's moons at phase angles between 50° and 60°, shown with a common stretch with a gamma of 0.75. Letters following the names indicate the hemisphere observed (T = trailing, L = leading, A = anti-Saturn). This gallery clearly demonstrates that Aegaeon is anomalously dark and has a comparable surface brightness to Iapetus' dark side. Image files used for this mosaic are: N1643265020 = Aegaeon, N1870695654 = Atlas, N1506184171 = Calypso (T), N1656997840 = Daphnis, N1597675353 = Dione (T), N1606072353 = Dione (L), N1824725635 = Enceladus (T), N1521539514 = Epimetheus (T), N1687121104 = Helene (L), N1669612923 = Hyperion, N1510339442 = Iapetus (L), N1521539514 = Janus (T), N1627323065 = Janus (A), N1716192290 = Methone (T), N1484509816 = Mimas (L), N1855894795 = Mimas (T), N1867602424 = Pan, N1504612286 = Pandora (T), N1853392689 = Prometheus (T), N1505772509 = Rhea (L), N1591815592 = Rhea (T), N1514163567 = Telesto (T), N1855868106 = Tethys (L), N1563723519 = Tethys (T).

some discrete event in the past is difficult because the E-ring should be able to brighten this moon relatively quickly. Assuming typical particle sizes of around 1 μm, the above estimates of the E-ring flux implies that Aegaeon would acquire a layer of E-ring particles 10 μm thick in only 100,000 yr. This calculation neglects mixing within Aegaeon's regolith and any material ejected from Aegaeon, but even this basic calculation shows that E-ring particles would cause Aegaeon to brighten on very short timescales, which strongly suggests that whatever process is making Aegaeon dark is actively ongoing.

Another possibility is that Aegaeon, Methone, and Pallene are dark because they are embedded not only in the E ring, but also in narrower rings like the G ring. However, since these rings likely consist of debris knocked off the moons' surfaces, this does not necessarily explain why this material would be so dark. Another problem is that Prometheus and Pandora are rather bright, even though these moons are close to the F ring and therefore are likely coated in F-ring material (see below). Furthermore, since the rings/arcs associated with Methone and Pallene are over an order of magnitude fainter than the G ring (Hedman et al. 2018), it seems unlikely that these tenuous rings could significantly affect the surface properties of those two moons. Thus, the G ring and other dusty rings do not appear to provide a natural explanation for the darkness of these small moons.

A more plausible explanation for the low surface brightnesses of Aegaeon, Methone, and Pallene is that these moons orbit Saturn within regions that have unique radiation environments. The bottom panel of Figure 16 shows profiles of energetic proton and electron fluxes from two of the highest-energy channels of *Cassini*'s Low-Energy Magnetospheric Measurement System (LEMMS) instrument (Krimigis et al. 2004). Note that while the electron flux has a broad peak centered around the orbit of Aegaeon, the high-energy proton

flux is confined to three belts between the main rings and the orbits of Janus, Mimas, and Enceladus (Roussos et al. 2008). This disjoint distribution of high-energy protons arises because energetic protons circle the planet under the influence of the corotation electric field, but their longitudinal motion is enhanced by gradient-curvature drifts, which act in the same direction as corotation. These particles therefore orbit the planet with a period of one to a few hours. Combined with the alignment of the spin and dipole axes, this drift allows these protons to re-encounter the inner moons frequently, causing a permanent flux decrease (macrosignature) along their orbits for sufficiently energetic protons. It is important to realize that these macrosignatures are not just depressions in the energetic proton density, but are also regions where the *flux* of protons is greatly decreased. Proton macrosignatures along the moon orbits are visible in the data at energies of >300 keV or so but are only expected to exist at much higher energies for electrons. Since Janus and Mimas are exposed to comparable amounts of energetic electrons as Aegaeon, Methone, and Pallene, the electron flux is not a natural explanation for the smaller moons' low surface brightness. However, Aegaeon, Methone, and Pallene are exposed to much higher fluxes of high-energy protons than any of Saturn's other moons, so this is a plausible potential explanation for the darkness of these three moons.

Table 6 provides more quantitative estimates of the proton fluxes into the different moons. Here, we use the protons observed with the P8 channel on the LEMMS instrument as a proxy for the total flux of high-energy protons (Krimigis et al. 2004). In the radiation belts, this channel's sensitivity is mainly to protons of 25.2–59 MeV, and the numbers reported in Table 6 are for an acceptance solid angle of 1 steradian to facilitate comparisons with the E-ring particle flux. Since Mimas, Janus, and Epimetheus occupy narrow gaps in the radiation belts, the fluxes provided in

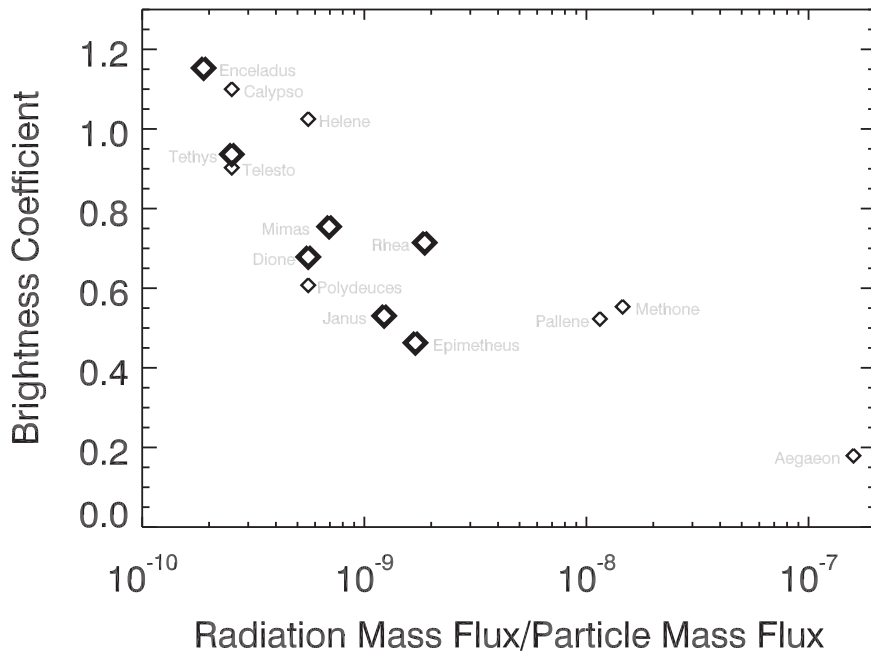


**Figure 19.** Moon brightness vs. the ratio of the radiation mass flux to the E-ring particle flux. The radiation mass flux here is the flux of protons with energies between 25 and 50 MeV, while the E-ring mass flux is the mass of particles larger than 1 micron. Note that the radiation fluxes for Methone, Pallene, and Aegaeon are measured, while for the other moons, they may represent upper limits. Still, the overall trend of decreasing brightness with increasing flux ratio is clear.

this table are averaged over the moons’ true anomalies. Furthermore, for Janus and Epimetheus, we also average over the semimajor axis variations associated with these moons’ co-orbital interactions. Also note that while estimates of the Galactic Cosmic Ray background have been removed from these data, the fluxes for the moons beyond Enceladus are probably upper limits. Nevertheless, these numbers clearly show that Methone, Pallene, and Aegaeon experience exceptionally high proton fluxes.

If radiation damage from high-energy protons is the dominant darkening process and the E-ring particles are the dominant brightening process, then we would expect the moons’ equilibrium surface brightness to depend on the ratio of the radiation flux to the E-ring particle flux. To make this ratio properly unitless, we consider the mass flux ratio for high-energy protons and E-ring particles. This quantity is computed by taking the number flux of protons given in Table 6 multiplied by the proton mass and dividing that number by the average flux of E-ring particles given in Table 6 multiplied by  $m_{\text{eff}}$ , the effective average mass of particles with radii larger than 1  $\mu\text{m}$ . Specifically, we assume  $m_{\text{eff}} = 4\pi \ln(100) \times 10^{-15} \text{ kg}$ , which is consistent with a power-law size distribution with a differential index of  $-4$  (Ye et al. 2014) extending between 1 and 100  $\mu\text{m}$ , and a particle mass density of  $1 \text{ g cm}^{-3}$ . Figure 19 shows that the moons’ brightnesses do indeed systematically decrease as this ratio increases. Furthermore, Methone, Pallene, and Aegaeon fall along the same basic trend in this plot as the mid-sized and co-orbital moons. This match provides strong evidence that radiation damage is the dominant process responsible for making Methone, Pallene, and Aegaeon dark.

At the moment, we do not know precisely which components of the radiation flux are responsible for the darkening. The macrosignatures are most prominent in the highest-energy proton channels, which suggests energetic protons are the dominant agent, but other agents (e.g., electrons with even higher energies) may also contribute at some level. If the darkening agent is protons with energies greater than 1 MeV, there are several ways

that they could be altering the surface. Howett et al. (2011) suggested that energetic electrons “sinter” or fuse grains in the uppermost layer, which can affect the reflectance properties at a range of wavelengths (Schenk et al. 2011; Howett et al. 2018). Electrons are mainly slowed down by interactions with electrons in materials. Protons are initially slowed down mainly by interactions with electrons in materials, although as they slow down, they interact more with nuclei. So it is possible very energetic protons (in the first fraction of their mean range) are causing the same kinds of changes to the ice as energetic electrons. Furthermore, they have large gyroradii and so they can often affect the whole body, i.e., they do not weather the surface differentially in many cases. Radiation damage can also change the chemical properties of surface materials, such as generating complex organics (Hapke 1986; Poston et al. 2018) or producing color centers in salts (Hand & Carlson 2015; Hibbitts et al. 2019; Trumbo et al. 2019), which could darken the surface and produce distinctive spectral signatures.

During its closest flybys of Aegaeon and Methone, *Cassini*’s NAC obtained images of both moons through multiple filters. We processed these high-resolution color images with the same methods as described above for the mid-sized moons, yielding the brightness coefficients given in Tables 27 and 28. We then interpolated these measurements to a single phase angle to obtain the visible spectra shown in Figure 20. Furthermore, during the close encounter with Methone, the Visual and Infrared Mapping Spectrometer (VIMS; Brown et al. 2004) was able to obtain near-infrared spectra of the moon. While VIMS was unable to spatially resolve Methone, VIMS acquired five “cubes” with good signal-to-noise (V1716191964, V1716192051, V1716192374, V1716192461, and V1716192872) that could yield decent disk-integrated spectra. We calibrated these cubes with the standard pipelines (Brown et al. 2004; Clark et al. 2012, flux calibration RC19), co-added the signals in the pixels containing the moon signal, removed backgrounds based on adjacent pixels, normalized the resulting spectra and averaged

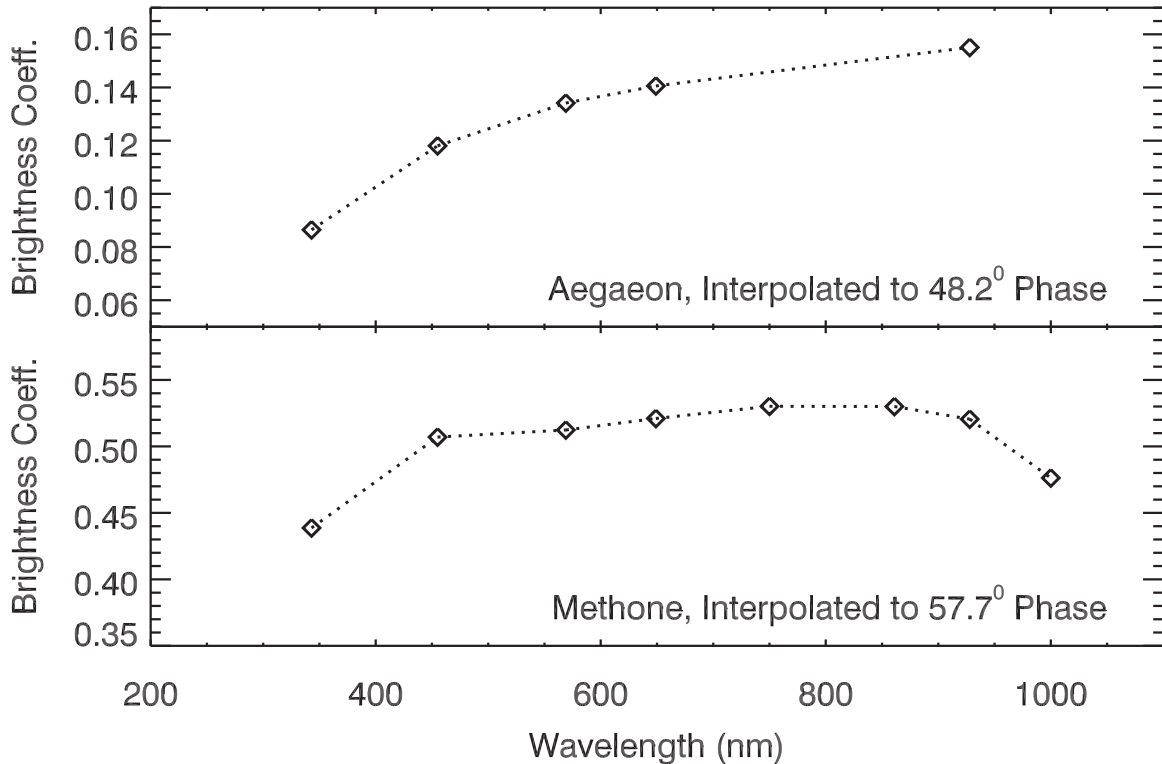


**Figure 20.** Visible spectra of Aegaeon and Methone obtained from resolved images during *Cassini*'s closest encounters with these moons. The only clear spectral feature is the break in slope around 500 nm, which is commonly found in spectra of the icy moons.

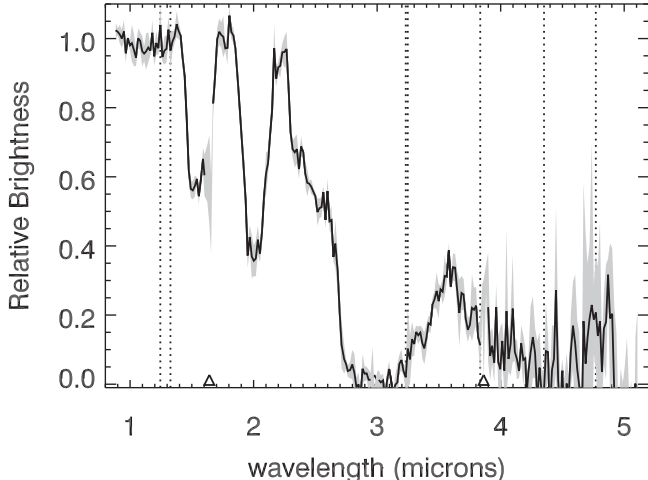


**Figure 21.** Near-infrared spectrum of Methone derived from observations from the VIMS instrument. The brightness is shown at an arbitrarily normalized scale. Note that the bands at 1.5, 2, and 3.1  $\mu\text{m}$  are typical of water ice, and the overall shape of the spectrum is comparable to that of other small moons.

them together to produce a single mean spectrum shown in Figure 21. (Note that this spectrum is arbitrarily normalized.) The near-infrared spectrum of Methone is dominated by water ice, while the visible spectra of the two moons are generally flat with a spectral break around 0.5  $\mu\text{m}$ . These moon's spectral properties are therefore very similar to those of the rest of Saturn's moons (Buratti et al. 2010, 2019; Filacchione et al. 2012). Furthermore, the depths of the water-ice bands at 1.5 and 2.0  $\mu\text{m}$  (computed following the procedures laid out in Filacchione et al. 2012) are  $0.45 \pm 0.04$  and  $0.60 \pm 0.06$ , respectively. These values are very similar to those previously found for Janus, Epimetheus, Telesto, Dione, and Rhea

(Filacchione et al. 2012). Hence, there is no evidence that these bodies have surfaces with distinctive spectrally active components, like irradiated salts (Hibbitts et al. 2019). Instead, the radiation appears to change the surface brightness relatively uniformly at all wavelengths.

An interesting point of comparison for these spectra is Jupiter's moon Callisto. Callisto and Aegaeon are probably exposed to similar fluxes of high-energy protons (roughly  $10/(\text{cm}^2 \text{ s sr keV})$  around energies of 1 MeV, Paranicas et al. 2018), and both objects are comparably dark (Callisto has a geometric albedo around 0.2 between 0.5 and 2.5  $\mu\text{m}$  (Calvin et al. 1995), and extrapolating the available data suggests that Aegaeon's equivalent spherical albedo is around 0.15). Like Aegaeon, Callisto has a visible spectrum that is flat longwards of 0.6  $\mu\text{m}$  and has a downturn at shorter wavelengths (Calvin et al. 1995; Moore et al. 2007). The structure in Callisto's spectrum in the near-infrared primarily consists of comparatively weak water-ice features, along with a weak carbon-dioxide band at 4.2  $\mu\text{m}$  (Moore et al. 2007), which is consistent with the compositional features seen in Methone and Saturn's other moons (Clark et al. 2008; Hendrix et al. 2018; Buratti et al. 2019). It may therefore be that both Callisto and Aegaeon represent end-members of what ice-rich surfaces look like when exposed to large doses of high-energy radiation. If correct, it could mean that even if we had near-IR spectra of Aegaeon, they would not contain diagnostic spectral features of the chemicals responsible for making its surface dark. Whether the observed amount of darkening is consistent with structural changes in the regolith (Howett et al. 2011; Schenk et al. 2011) or chemical changes in a more spectrally neutral component (such as the non sulfur-bearing ices in Poston et al. 2018), will require detailed spectral models that are beyond the scope of this work.

#### 4.4. The Excess Brightness of Prometheus, Pandora, Calypso, and Helene

After Aegaeon, Methone, and Pallene, the next most obvious anomalies in Figure 17 are Helene and Calypso. Calypso is brighter than both Tethys and Telesto, while Helene is brighter than both Dione and Polydeuces. These findings are actually consistent with prior estimates of these moons' geometric albedos summarized in Verbiscer et al. (2007, 2018). At the same time, it is worth noting that despite being in a region where the E-ring flux should be extremely low, Pan, Atlas, Prometheus, and Pandora are all reasonably bright, and in particular, Prometheus and Pandora are brighter than any of the other moons in their vicinity. The excess brightness of these moons is probably related to distinctive aspects of their near-infrared spectra. For the mid-sized moons, the depths of the moon's water-ice bands are reasonably well correlated with their visible brightness (Filacchione et al. 2012). However, Calypso, Prometheus, and Pandora all have deeper water-ice bands than Enceladus, while Atlas, Telesto, and Helene have water-ice bands intermediate in strength between Tethys and Dione (Buratti et al. 2010; Filacchione et al. 2012, 2013). Note that even though Helene does not appear to have as exceptionally deep water-ice bands as Calypso, both Calypso and Helene have deeper bands than their respective large companions Tethys and Dione. The anomalous spectral and photometric properties of Prometheus, Pandora, Calypso, and Helene could be attributed to a number of different factors, including the moons' size and differences in the local radiation environment. In practice, localized enhancements in the particle flux appear to be the most likely explanation, but the excess particle flux responsible for the high observed brightnesses of Helene and Calypso is far from clear.

In principle, the surface brightness of small moons could be different from the brightness of large moons in the same environment because their reduced surface gravity affects the porosity and structure of their regolith. In fact, one aspect of these moons' surface properties probably can be attributed to their small size: their general lack of a leading-trailing brightness asymmetries. In particular, all four of the trojan moons appear to lack the strong leading-trailing brightness asymmetries seen on Tethys and Dione.<sup>9</sup> For Tethys and Dione, this asymmetry is thought to arise because of asymmetries in the E-ring flux, so it is perhaps surprising that similar asymmetries are not seen in the smaller moons. However, the smaller size and much lower surface gravity of these moons means that secondary ejecta from the E-ring impacts can be more easily globally dispersed over their surfaces, providing a natural explanation for why these moons have more uniform surface properties.

While detailed modeling of impact debris transport around these small moons is beyond the scope of this paper, we can provide rough order-of-magnitude calculations that are sufficient to demonstrate the feasibility of this idea. Assuming that most of the E-ring particles striking these moons are near the apocenters of their eccentric orbits, we can assume  $r \simeq (1 + e) a$  in Equation (23) and estimate the E-ring particle's impact velocities at the orbits of Tethys and Dione to be  $1.4 \text{ km s}^{-1}$  and  $3.6 \text{ km s}^{-1}$ , respectively. Experimental studies of impacts

<sup>9</sup> Hirata et al. (2014) also found that there was not a strong leading-trailing asymmetry in the morphology of deposits on Telesto and Calypso. However, they also found that Helene appears to have a higher crater density on its trailing side, perhaps implying a thicker mantling deposit on its leading side.

into ice-rich targets by  $20\text{--}100 \mu\text{m}$  glass beads found impact yields at these velocities of the order of 100 (Koschny & Grün 2001), and assuming roughly comparable values for micron-sized E-ring grains would imply an effective average ejection velocity of at most  $14 \text{ m s}^{-1}$  and  $36 \text{ m s}^{-1}$ , respectively. These speeds are much less than the escape speeds from Tethys and Dione (which are  $390$  and  $510 \text{ m s}^{-1}$ , respectively), but are comparable to the escape speeds of Telesto, Calypso, and Helene (which are  $7$ ,  $19$ , and  $9 \text{ m s}^{-1}$ , respectively). Hence, it is reasonable to think that the debris from E-ring particle impacts is more uniformly distributed on the smaller trojans than they are on Tethys and Dione, making their surfaces more uniform in brightness.

However, while their size is likely responsible for their lack of leading-trailing brightness asymmetries, it is unlikely that size-related phenomena can explain the overall high brightness of Prometheus, Pandora, Calypso, and Helene. The problem with such ideas is that there are no clear trends between size and brightness excess. Telesto is intermediate in size between Helene and Calypso but is roughly the same brightness as Tethys. Also, Prometheus and Pandora are themselves intermediate in size between Epimetheus and Atlas. This lack of obvious trends with mass or size suggests that the brightness excess of these moons most likely reflects something different about their environments.

Given the previous analyses of the trends among the other moons, the easiest way to increase the brightness of these moons would be either by decreasing the radiation flux or increasing the particle flux. Decreasing the radiation flux is an unlikely explanation because the high-energy proton flux onto many of the moons is already very low (see Table 6). Furthermore, for the radiation flux to be lower at Calypso than at Telesto, or lower at Helene than at Polydeuces, there would need to be a strong asymmetry in the radiation flux on either side of Tethys and Dione. While both Tethys and Dione have been observed to produce localized reductions in plasma known as microsignatures, these do not extend all the way to the trojan moons. Also, given that the plasma is bound to the planet's magnetic field, which rotates faster than the moons orbit around the planet, it is hard to imagine any interaction with charged particles that would similarly affect Calypso (which trails Tethys) and Helene (which leads Dione).

The above considerations leave variations in the particle flux as the best remaining option. For Prometheus and Pandora, this is a perfectly reasonable explanation, since these moons fall within the outskirts of the F ring, which is a natural source of dust flux into these moons. If an excess flux of F-ring particles is indeed responsible for the high brightness of Prometheus and Pandora, this is interesting because it means that the dust impacting the moons does not have to be the relatively fresh ice found in the E ring to produce increases in brightness. In this case, the lower-opacity dusty rings surrounding Pan and Atlas could be keeping those moons somewhat brighter than they would otherwise be given their locations well interior to the E ring.

Excess dust fluxes are also an attractive explanation for the excess brightness of Calypso and Helene because these moons are nearly as bright as Enceladus, an object whose brightness is certainly due to a high particle flux. However, there is no obvious source for the particles that would strike Calypso and Helene more than their co-orbital companions. The brightness differences cannot be easily attributed to differences in the

E-ring flux, since Telesto, Calypso, and Tethys are at basically the same orbital distance from Saturn, as are Helene, Polydeuces, and Dione. Hence, the E-ring flux into Telesto, Tethys, and Calypso (or Helene, Dione, and Polydeuces) should be nearly the same.

In principle, asymmetries in the particle flux could arise from either subtle interactions between the larger moons and the E-ring grains, or more local particle populations sourced from the larger moons. For example, particles on nearly circular orbits launched from Tethys that are carried outward by plasma drag would preferentially fall behind Tethys, and thus potentially be more likely to strike Calypso than Telesto. The problem with such explanations is that for Calypso and Helene to fall along the same trend as the other moons in Figure 17, the excess particle flux into these moons needs to be a substantial fraction of the E ring flux, which would imply a large excess density of particles around these moons compared to Tethys, Dione, Telesto, or Polydeuces. These particles should produce localized brightness enhancements and/or longitudinal brightness asymmetries in the regions around Tethys' and Dione's orbits, and no such features have yet been seen in the *Cassini* images of the E ring. In principle, there could be some subtle interactions between E ring particles and the relevant moons that would cause the requisite variations in the particle flux without producing detectable asymmetries in the density of the rings. Fully exploring such possibilities would likely require numerical simulations that are beyond the scope of this work.

Given the above challenges with identifying a suitable dust population around these moons during the *Cassini* mission, it is worth considering whether Calypso's and Helene's current brightnesses are not their steady-state values but are instead transient phenomena caused by some event in the relatively recent past. Specifically, we can consider the possibility that a recent impact into Calypso and/or Helene released enough material to affect the global surface properties of both these moons. A thorough quantitative evaluation of such scenarios is beyond the scope of this paper. Instead we will just provide some order-of-magnitude calculations that demonstrate that this is a viable possibility.

The total amount of material needed to affect the overall surface brightness of Calypso and Helene is simply the amount of material needed to coat these moons with a layer thick enough to determine its optical properties at optical wavelengths. Since light can only penetrate a few wavelengths through the surface regolith, we may conservatively estimate that a 10  $\mu\text{m}$  thick layer of material will be sufficient for these purposes. Given that Calypso and Helene have surface areas of around 400  $\text{km}^2$  and 1400  $\text{km}^2$ , respectively, the total volume of material needed to coat these moons is 4000 and 14,000  $\text{m}^3$ . Conservatively assuming this is ice-rich material of negligible porosity, these volumes correspond to total debris masses of  $4 \times 10^6$  and  $14 \times 10^6 \text{ kg}$ , respectively.

The flux of objects large enough to produce these sorts of debris clouds is fairly well constrained thanks to observations of comparably massive impact-generated debris clouds above Saturn's rings described by Tiscareno et al. (2013). The masses of those clouds are uncertain and depend on the assumed size distribution of the debris, but the feature designated Bx probably had a mass between  $2 \times 10^5 \text{ kg}$  and  $2 \times 10^7 \text{ kg}$ , which is comparable to that required to brighten Calypso or Helene. The estimated flux of impactors able of producing this amount of debris is  $3 \times 10^{-20} \text{ m}^{-2} \text{ s}^{-1}$  (Tiscareno et al. 2013).

Assuming cross sections consistent with the observed sizes of Calypso and Helene, this means the mean time between impacts should be between 1000 and 10,000 yr.

The other relevant timescale in this problem is how long it would take E-ring material to coat these moons and erase any transient signals from an impact. Using the fluxes provided in Table 6, and assuming a typical E-ring particle radius of around 1  $\mu\text{m}$ , we estimate that E-ring material would accumulate on the surfaces at rates of between 0.2 nm yr<sup>-1</sup> for Helene and 0.5 nm yr<sup>-1</sup> for Calypso. It would therefore take 20,000 yr for Calypso and 50,000 yr for Helene to accumulate a 10  $\mu\text{m}$  thick layer of E-ring particles. These numbers could potentially be reduced by a factor of  $\sim 100$  if we account for the yield of secondary debris from each E-ring particle impact (see above). The resurfacing time due to E-ring particles is therefore likely comparable to the mean time between impacts capable of covering these entire moons in fresh impact debris. It is therefore not unreasonable that Calypso and Helene both experienced a recent impact that brightened their surfaces, while Telesto and Polydeuces managed to avoid such a recent collision. In principle, some of the material from a collision into Helene or Calypso could have been transported to the other moon, allowing a single impact to brighten both moons, but to properly explore the relative likelihood of such an event will require numerical simulations of both dynamics of the impact debris similar to those done by Dobrovolskis et al. (2010), perhaps including non-gravitational forces.

Note that this explanation for Calypso's and Helene's brightness means that impacts tend to increase the moons' brightness, rather than darken them. This might at first be counterintuitive because cometary debris in the outer solar system is generally assumed to be much darker than Saturn's moons. However, it is important to realize that most of the debris produced by the impacts would come from Helene and Calypso, not the impactor. Indeed, the expected impact yields for such bodies is of the order of 10,000 (Cuzzi & Estrada 1998; Tiscareno et al. 2013), and so the impactor required to produce  $4-14 \times 10^6 \text{ kg}$  of debris would be only  $4-14 \times 10^2 \text{ kg}$ , which corresponds to an ice-rich object with a radius between 0.5 and 0.7 m. Thus, most of the debris falling on the moons would be pure ice and should be able to brighten moon surfaces like the E and F rings are apparently able to do. This bright deposit would also be much thinner than the deposits previously identified in high-resolution images, which affect both the morphology and the color of the surface (Thomas et al. 2013; Hirata et al. 2014). While such a thin deposit would probably not produce obvious morphological structures (even the original crater would be near the resolution limit of the best images), it is not clear whether a fresh global covering of fine debris is consistent with the color variations currently observed on these moons (Thomas et al. 2013). Also, it is not obvious whether recent impacts are consistent with near-infrared spectra of these moons, which show that Prometheus, Pandora, and Calypso have deeper ice bands than Telesto and Helene (Filacchione et al. 2012). Even so, the above considerations indicate that a recent impact is a possible explanation for Calypso's and Helene's high surface brightness and so merits further investigation.

## 5. Summary

In conclusion, we have used a new photometric model for non-spherical objects to obtain surface brightness estimates that are comparable to those for the mid-sized satellites. Applying this model to Saturn's moons has revealed a number of

interesting features and trends, which are summarized below in order of the moons' increasing distances from Saturn.

1. Prometheus and Pandora are brighter than moons orbiting exterior and interior to them, suggesting that dust from the F ring is brightening these moons.
2. Janus and Epimetheus have brighter trailing hemispheres than leading hemispheres, which is consistent with the expected pattern for impacting E-ring particles.
3. Aegaeon, Methone, and Pallene are all darker than expected given their location within the E ring. This is most likely due to the high flux of high-energy radiation into these moons.
4. The spectral data for Aegaeon and Methone indicate that whatever material is responsible for making these moons dark reduces their brightness over a broad range of wavelengths and does not have obvious spectral signatures.
5. The photometric data indicate that Anthe probably has a shape similar to Methone.
6. Pallene's leading side is slightly darker than its trailing side.

7. Telesto and Polydeuces have surface brightnesses similar to their larger orbital companions (Tethys and Dione, respectively).
8. Calypso is substantially brighter than Tethys and Telesto, while Helene is substantially brighter than Dione and Polydeuces. These phenomena could either be due to an asymmetric flux of E-ring particles, or recent collisions with larger impactors.

Authors M.M.H. and P.H. offer thanks to NASA's *Cassini* Mission Project during various stages of this study. M.M.H. acknowledges support from the *Cassini* Data Analysis Program Grant NNX15AQ67G. P.H. gratefully acknowledges that photometric modeling enhancements, as well as refinements and testing of computer software that are used and first-reported in this paper, were developed under the auspices of NASA Planetary Geology and Geophysics Program grant NNX14AN04G. M.H. also wishes to acknowledge that the initial analyses of the small moons' brightnesses were done by M. Rehnberg as part of the REU program, and the calculations regarding the deposition rates on the various small moons were inspired by conservations with S. Morrison, S. G. Zaidi, and H. Sharma.

## Appendix A Python Code to Evaluate Predicted Areas

Note, the inputs to this program are the sub-solar longitude `slon`, the sub-solar latitude `slat`, the sub-observer longitude `clon`, the sub-observer latitude `clat`, the object's shape parameters `a,b,c`, and the Minnaert parameter `k`.

```
def objmod (slon,slat,clon,clat,a,b,c,k):
    import numpy as np
    theta=np.pi/180*np.array(range(181))
    phi=np.pi/180*np.array(range(361))
    mat=np.array(np.ones((361,181),float))
    thx=mat*1.0
    phix=mat*1.0
    for i in range(361):
        for j in range(181):
            thx[i,j]=np.pi*j/180
            phix[i,j]=np.pi*i/180
    areaf=np.sqrt(a**2*b**2*np.cos(thx)**2 + c**2*(b**2*np.cos(phi)**2 + a**2*np.sin(phi)**2)**2)
    rf=np.sqrt(areaf)
    xf=np.sin(thx)*np.cos(phi)/a
    yf=np.sin(thx)*np.sin(phi)/b
    zf=np.cos(thx)/c
    nx=xf/np.sqrt(xf**2+yf**2+zf**2)
    ny=yf/np.sqrt(xf**2+yf**2+zf**2)
    nz=zf/np.sqrt(xf**2+yf**2+zf**2)
    sln=slon*np.pi/180
    slt=(90-slat)*np.pi/180
    cln=clon*np.pi/180
    clt=(90-clat)*np.pi/180
    cosi=nx*np.sin(slt)*np.cos(sln)+ny*np.sin(slt)*np.sin(sln)+nz*np.cos(slt)
    cose=nx*np.sin(clt)*np.cos(cln)+ny*np.sin(clt)*np.sin(cln)+nz*np.cos(clt)
    cosi=.5*(cosi+abs(cosi))
    cose=.5*(cose+abs(cose))
    bright=cosi**k*cose**k*(1-k)
    brfact=bright*np.sin(thx)*areaf*cose*np.pi/180*np.pi/180
    pred=np.sum(brfact)

    return pred
```

## Appendix B A Revised Shape for Polydeuces

The shape model of Polydeuces reported by Thomas et al. (2013) has relatively large uncertainties because it was based on a very limited number of resolved images. Fortunately, late in the *Cassini* mission, there were two additional flybys of Polydeuces where the moon was over 10 pixels wide in the Narrow Angle Camera. Furthermore, in several of these images, a large fraction of the limb is visible thanks to the combination of direct illumination and Saturn shine (see Figures 22 and 23). The full set of resolved images listed in Table 7 was then manually fit to a  $(5^\circ \times 5^\circ)$  shape model. Saturn shine was crucial in getting centers. Shape control is good for the  $a$  and  $c$  axes;  $a$  is the best constrained, because the Saturn-shine images taken from near the intermediate axis show the full projection of  $a$ . The  $b$  axis is poorly constrained, with the terminator in some images being the primary source of information about this dimension. Note that the limb positions shown in Figure 23 are relatively smooth, but they do not approximate simple ellipsoids.

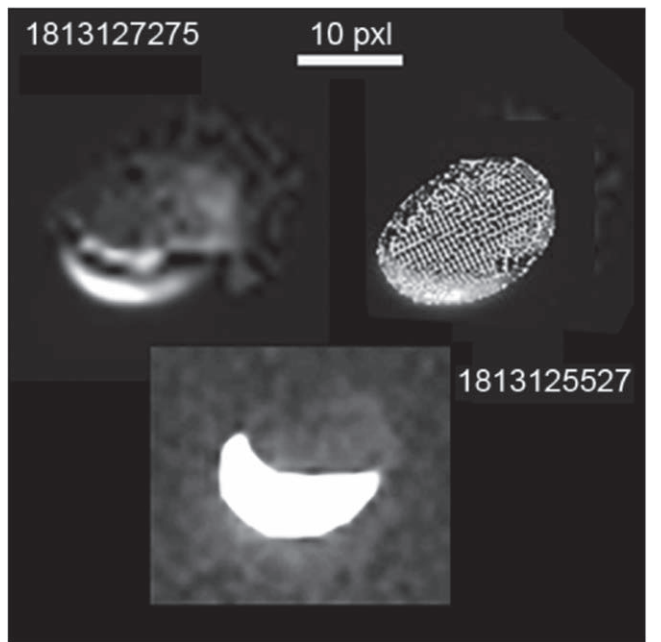


**Figure 22.** Shape analysis of Polydeuces from image N1813125527. Top left: image with regions under direct illumination and Saturn-shine illumination stretched separately. Top right: final shape model overlaid on image. Bottom: image with a single stretch.

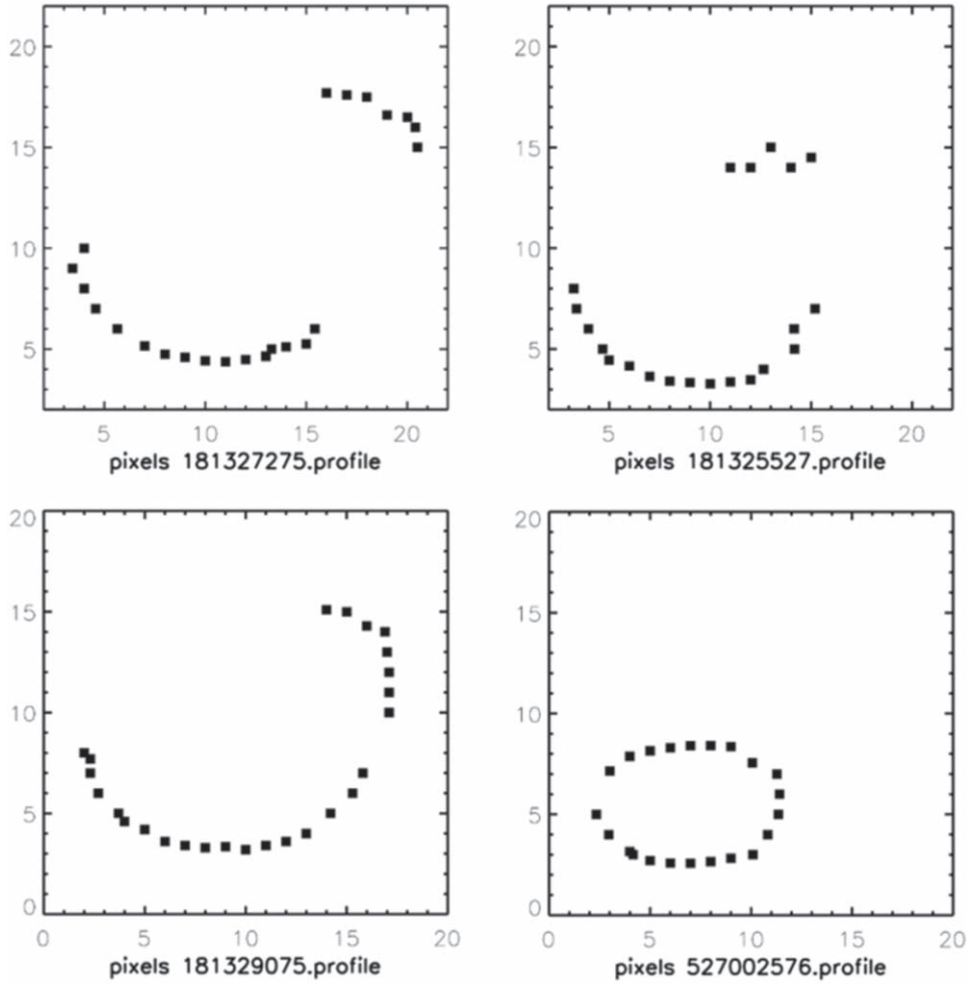


**Figure 23.** Estimated limb locations from representative images of Polydeuces.

**Table 7**  
Resolved Images of Polydeuces Used to Derive Its Shape

Image	Sub-spacecraft Lat. (deg)	Sub-spacecraft Long. (deg)	Sub-solar Lat. (deg)	Sub-solar Long. (deg)	Range (km)	Pole <sup>a</sup> (deg)	$x_c$ (pixels)	$y_c$ (pixels)
N1526998156	-0.69	300.81	-17.38	265.61	70745.54	359.92	504.9	512.4
N1527002576	-0.51	282.09	-17.38	272.34	64087.42	359.92	524.1	511.2
N1527002708	-0.50	281.47	-17.38	272.54	64101.53	359.92	527.4	511.9
N1527006179	-0.28	265.98	-17.38	277.82	68549.73	359.92	552.1	511.8
N1809910321	-0.02	30.47	24.54	300.35	47250.34	99.94	511.1	575.9
N1809910848	-0.05	34.59	24.54	301.16	44829.21	99.92	520.7	580.0
N1813120961	0.76	221.86	24.76	146.90	54004.30	179.92	495.6	519.7
N1813121872	0.87	227.85	24.76	148.29	49544.58	179.92	511.8	418.4
N1813121938	0.88	228.31	24.76	148.39	49237.54	179.92	511.3	407.1
N1813123674	1.13	242.24	24.76	151.03	41948.07	179.92	539.3	571.7
N1813125527	1.41	261.21	24.76	153.85	36595.63	151.89	533.3	414.4
N1813125560	1.42	261.59	24.76	153.90	36528.47	151.89	533.8	413.8
N1813127275	1.60	282.26	24.76	156.51	34808.05	153.29	546.6	574.0
N1813129075	1.61	303.92	24.76	159.25	36813.49	157.30	543.7	424.7
N1813129108	1.61	304.29	24.76	159.30	36884.91	157.39	541.3	410.2

**Note.**<sup>a</sup> Predicted positive pole azimuth in images, clockwise from up.

## Appendix C

### Data Tables for Individual Observations

In Tables 8–28, “Range” indicates the distance between the spacecraft and the body center. “Phase” is the solar phase angle at body center, “Sub-S/C Latitude/Longitude” are the sub-spacecraft planetocentric latitude and (west) longitude, while “Sub-solar Latitude/Longitude” are the sub-solar planetocentric latitude and (west) longitude. The value of  $A_{\text{eff}}$  is computed as described in the text, and the statistical error estimate is based on the scatter of brightness values in regions near the planet (note this uncertainty is very small and so is not

included for the larger moons).  $A_{\text{phys}}$  is the geometrical cross section of the moon from the perspective of the spacecraft, and the three values of  $a_{\text{pred}}$  are computed assuming Minnaert scattering laws with  $k = 1.0, 0.75$  and  $0.50$  assuming the shape parameters provided in Table 1. Note that since the shape of Anthe is not well determined, these parameters could not be computed for that moon. All images were obtained using the *Cassini* ISS NAC clear filters except for those given in the last two tables. All of these data tables are provided in machine-readable format in supplementary information associated with this article.

**Table 8**  
Brightness Estimates from Clear-filter Images of Aegaeon

Filename	Range (km)	Phase (deg)	Sub-S/C Latitude (deg)	Sub-S/C Longitude (deg)	Sub-solar Latitude (deg)	Sub-solar Longitude (deg)	$A_{\text{eff}}$ Value (km <sup>2</sup> )	$A_{\text{eff}}$ Error (km <sup>2</sup> )	$A_{\text{phys}}$ (km <sup>2</sup> )	$a_{\text{pred}}$ $k = 1$ (km <sup>2</sup> )	$a_{\text{pred}}$ $k = 0.75$ (km <sup>2</sup> )	$a_{\text{pred}}$ $k = 0.50$ (km <sup>2</sup> )
N1560588018	1708521.8	42.9	0.5	94.9	-12.0	136.3	0.05365	0.00490	0.4384	0.2172	0.2323	0.2511
N1597476237	1188834.9	28.2	5.0	264.3	-5.6	238.1	0.07027	0.00199	0.4390	0.2630	0.2720	0.2826
N1597477967	1215347.6	28.2	5.2	273.2	-5.6	247.1	0.06765	0.00234	0.4404	0.2819	0.2871	0.2938
N1598073885	1170967.9	12.9	-0.8	91.4	-5.5	79.3	0.08536	0.00193	0.4397	0.3073	0.3084	0.3098
N1598104211	1179616.4	28.4	3.9	262.5	-5.5	235.7	0.05817	0.00382	0.4371	0.2573	0.2672	0.2787
N1598106121	1209151.0	28.4	4.0	272.3	-5.5	245.5	0.06960	0.00162	0.4403	0.2803	0.2861	0.2933
N1600657200	1205263.9	15.2	4.4	89.6	-5.0	77.6	0.07635	0.00125	0.4407	0.3020	0.3038	0.3063
N1600659110	1177824.9	15.5	4.8	99.5	-5.0	87.5	0.07693	0.00195	0.4355	0.3038	0.3034	0.3038
N1603168767	1203629.1	14.9	0.1	80.3	-4.6	66.1	0.07670	0.00263	0.4346	0.2859	0.2903	0.2951
N1603169886	1188076.4	14.9	0.3	86.0	-4.6	71.9	0.11391	0.00194	0.4390	0.2978	0.3008	0.3042
N1603171005	1172385.6	14.9	0.4	91.7	-4.6	77.6	0.09027	0.00139	0.4397	0.3050	0.3065	0.3084

(This table is available in its entirety in machine-readable form.)

**Table 9**  
Brightness Estimates from Clear-filter Images of Anthe

Filename	Range (km)	Phase (deg)	Sub-S/C Latitude (deg)	Sub-S/C Longitude (deg)	Sub-solar Latitude (deg)	Sub-solar Longitude (deg)	$A_{\text{eff}}$ Value ( $\text{km}^2$ )	$A_{\text{eff}}$ Error ( $\text{km}^2$ )
N1575629162	1802888.5	14.3	4.6	314.9	-9.4	312.0	0.87980	0.00018
N1579321873	1440656.1	11.3	2.1	36.8	-8.8	34.0	0.94105	0.00006
N1579364158	1258508.1	17.9	6.6	213.0	-8.8	203.9	0.76642	0.00094
N1580356175	1214750.8	20.0	3.0	247.6	-8.6	231.3	0.88177	0.00086
N1581514393	1472790.1	21.2	12.5	210.3	-8.4	206.6	0.74765	0.00064
N1591878477	1067058.5	9.7	-2.1	117.6	-6.6	109.0	1.11239	0.00026
N1595481922	869685.1	30.3	-13.2	225.5	-5.9	195.6	0.56951	0.00006
N1596338308	1242696.0	28.9	22.9	42.6	-5.8	38.7	0.57676	0.00029
N1596721036	861845.3	21.8	-17.3	156.5	-5.7	137.6	0.67246	0.00010
N1599961164	1029589.9	30.0	-5.2	234.4	-5.1	204.3	0.68365	0.00041

(This table is available in its entirety in machine-readable form.)

**Table 10**  
Brightness Estimates from Clear-filter Images of Methone

Filename	Range (km)	Phase (deg)	Sub-S/C Latitude (deg)	Sub-S/C Longitude (deg)	Sub-solar Latitude (deg)	Sub-solar Longitude (deg)	$A_{\text{eff}}$ Value ( $\text{km}^2$ )	$A_{\text{eff}}$ Error ( $\text{km}^2$ )	$A_{\text{phys}}$	$a_{\text{pred}}$ $k = 1$ ( $\text{km}^2$ )	$a_{\text{pred}}$ $k = 0.75$ ( $\text{km}^2$ )	$a_{\text{pred}}$ $k = 0.50$ ( $\text{km}^2$ )
N1502651083	2157110.5	61.1	-16.3	195.6	-20.7	131.0	0.85344	0.00034	5.3901	1.7843	1.7464	1.7810
N1502796764	2182712.0	49.2	-16.1	63.9	-20.7	12.0	1.23989	0.00288	7.0567	2.7398	2.9195	3.1932
N1505466661	2597383.5	75.2	-0.3	304.2	-20.4	229.8	1.08037	0.00377	6.7187	2.6551	2.7021	2.8410
N1506716564	2357443.8	78.3	-0.3	65.0	-20.2	347.3	0.59662	0.00542	7.0143	1.2778	1.3753	1.5609
N1513354056	2991500.0	75.9	-0.2	90.1	-19.3	14.9	0.92142	0.00364	7.3746	1.9798	2.1500	2.4335
N1513572473	2639783.5	77.0	-0.3	272.5	-19.3	196.2	0.92816	0.00253	7.3726	1.9867	2.1553	2.4368
N1513697664	2444116.8	64.6	-0.3	55.8	-19.3	352.7	0.46728	0.00244	6.7177	1.6638	1.7749	1.9790
N1513745334	2160722.2	70.8	-0.3	259.1	-19.3	189.4	0.74070	0.00250	7.3012	1.9526	2.1226	2.4042
N1513875625	1857151.5	53.5	-0.3	58.0	-19.3	6.9	0.95244	0.00261	6.7962	2.2552	2.4016	2.6437
N1549374867	1488836.9	53.5	24.1	307.3	-13.9	345.9	0.95830	0.00073	6.8320	2.1726	2.3225	2.5697

(This table is available in its entirety in machine-readable form.)

**Table 11**  
Brightness Estimates from Clear-filter Images of Pallene

Filename	Range (km)	Phase (deg)	Sub-S/C Latitude (deg)	Sub-S/C Longitude (deg)	Sub-solar Latitude (deg)	Sub-solar Longitude (deg)	$A_{\text{eff}}$ Value ( $\text{km}^2$ )	$A_{\text{eff}}$ Error ( $\text{km}^2$ )	$A_{\text{phys}}$	$a_{\text{pred}}$ $k = 1$ ( $\text{km}^2$ )	$a_{\text{pred}}$ $k = 0.75$ ( $\text{km}^2$ )	$a_{\text{pred}}$ $k = 0.50$ ( $\text{km}^2$ )
N1502276381	2437835.2	78.9	-10.4	287.9	-20.8	205.9	2.01443	0.00006	16.3913	5.0531	5.3314	5.8471
N1502795579	2300004.0	56.1	-15.3	339.6	-20.7	280.6	2.70475	0.00006	13.2926	6.5691	6.3338	6.2744
N1505466121	2520183.0	76.3	-0.3	279.6	-20.4	204.1	1.68066	0.00263	16.5546	4.9522	5.2495	5.7894
N1506716999	2173371.8	78.1	-0.3	118.7	-20.2	41.4	1.67143	0.00796	15.7004	5.3684	5.5332	5.9192
N1506907435	2497063.0	71.6	-0.3	79.2	-20.2	8.8	1.63914	0.00849	16.5278	4.4971	4.8088	5.3639
N1508412740	2300827.8	74.2	-0.4	117.9	-20.0	44.6	1.74305	0.00371	15.7529	5.8123	5.9700	6.3476
N1511332959	2177036.2	70.4	-0.3	218.9	-19.6	149.7	1.25172	0.00081	14.0280	3.1824	3.2588	3.5060
N1511457594	2063485.1	65.9	-0.3	303.6	-19.6	239.2	2.54285	0.00214	15.4411	6.7978	6.8418	7.0881
N1513573553	2819354.8	70.9	-0.2	29.3	-19.3	319.5	1.22749	0.01477	13.3699	3.1804	3.1936	3.3680
N1513745544	2272592.5	71.0	-0.3	291.1	-19.3	221.2	2.37342	0.00109	16.1621	6.0496	6.2639	6.7042

(This table is available in its entirety in machine-readable form.)

**Table 12**  
Brightness Estimates from Clear-filter Images of Telesto

Filename	Range (km)	Phase (deg)	Sub-S/C Latitude (deg)	Sub-S/C Longitude (deg)	Sub-solar Latitude (deg)	Sub-solar Longitude (deg)	$A_{\text{eff}}$ Value ( $\text{km}^2$ )	$A_{\text{eff}}$ Error ( $\text{km}^2$ )	$A_{\text{phys}}$	$a_{\text{pred}}$ $k = 1$ ( $\text{km}^2$ )	$a_{\text{pred}}$ $k = 0.75$ ( $\text{km}^2$ )	$a_{\text{pred}}$ $k = 0.50$ ( $\text{km}^2$ )	
N1495206641	1158822.1	41.0	-20.6	283.1	-21.7	239.0	209.49303	0.00203	510.9615	291.6927	296.2795	304.6195	
N1495310692	533103.5	48.7	-16.1	57.3	-21.6	108.6	186.92639	0.00024	477.0852	267.6940	266.3135	269.2979	
N1513353874	3223840.5	76.1	-0.2	38.3	-19.3	323.0	55.22128	0.02512	418.3909	80.5283	81.8249	87.6863	
N1513525391	2910381.2	70.1	-0.2	50.4	-19.3	341.4	60.29562	0.02358	448.4575	98.7257	103.0927	113.0088	
N1515851740	1677181.9	64.8	-0.1	138.3	-19.0	75.1	125.14794	0.00486	424.5765	195.9870	191.5797	192.7610	
33	N1550920790	1675677.8	54.1	17.0	20.2	-13.6	65.3	118.35385	0.00402	402.1162	166.1985	162.1580	163.5099
	N1551094911	1848412.8	78.9	35.6	24.2	-13.6	89.6	67.92459	0.01501	474.1757	127.2060	127.8723	134.8444
	N1552385974	1908353.1	60.3	23.1	9.4	-13.4	58.5	91.43609	0.00739	409.6214	135.3984	133.7996	137.6850
	N1552559265	2051421.1	79.1	35.6	15.1	-13.4	80.9	63.43113	0.01314	465.5626	115.4674	115.9241	122.3549
	N1553937429	1710299.9	73.7	39.0	186.0	-13.1	242.1	59.57480	0.00959	472.9421	110.4580	112.4599	120.3907

(This table is available in its entirety in machine-readable form.)

**Table 13**  
Brightness Estimates from Clear-filter Images of Calypso

Filename	Range (km)	Phase (deg)	Sub-S/C Latitude (deg)	Sub-S/C Longitude (deg)	Sub-solar Latitude (deg)	Sub-solar Longitude (deg)	$A_{\text{eff}}$ Value ( $\text{km}^2$ )	$A_{\text{eff}}$ Error ( $\text{km}^2$ )	$A_{\text{phys}}$	$a_{\text{pred}}$ $k = 1$ ( $\text{km}^2$ )	$a_{\text{pred}}$ $k = 0.75$ ( $\text{km}^2$ )	$a_{\text{pred}}$ $k = 0.50$ ( $\text{km}^2$ )	
N1495209871	890860.8	16.6	-26.6	140.6	-21.7	123.2	215.58528	0.00317	286.1855	174.0992	172.8976	172.3568	
N1495306082	744442.8	8.1	-13.8	337.8	-21.6	335.5	175.25667	0.00123	226.2691	127.2145	124.7317	122.5648	
N1511290086	2690833.8	65.2	-0.4	36.6	-19.6	332.9	17.58906	0.08132	232.8271	49.1007	49.7600	52.9677	
N1513526081	2894673.2	79.3	-0.2	306.3	-19.3	227.6	74.90391	0.00928	263.6748	94.7175	95.4810	99.6274	
N1513746037	2373977.8	60.5	-0.4	51.7	-19.3	353.0	46.70824	0.01034	260.2657	63.1165	66.3753	72.8773	
34	N1515907721	1464391.1	60.9	-0.2	142.6	-19.0	83.5	83.69676	0.00505	233.0732	113.9775	108.6222	106.2716
	N1552346494	1321233.1	61.8	27.5	159.6	-13.4	207.5	37.35155	0.00874	268.3173	44.9510	47.2656	52.3660
	N1553898744	2159565.5	64.2	27.7	341.8	-13.1	33.1	26.20873	0.02650	268.3491	44.8040	46.7589	51.4545
	N1555145582	1602579.5	48.5	20.1	228.9	-12.9	265.0	128.16917	0.00516	281.0121	125.2374	124.5597	127.3711
	N1555190012	2097829.5	50.7	18.5	322.5	-12.9	2.9	39.47476	0.01584	260.9357	60.1786	64.1787	71.3580

(This table is available in its entirety in machine-readable form.)

**Table 14**  
Brightness Estimates from Clear-filter Images of Helene

Filename	Range (km)	Phase (deg)	Sub-S/C Latitude (deg)	Sub-S/C Longitude (deg)	Sub-solar Latitude (deg)	Sub-solar Longitude (deg)	$A_{\text{eff}}$ Value (km <sup>2</sup> )	$A_{\text{eff}}$ Error (km <sup>2</sup> )	$A_{\text{phys}}$ (km <sup>2</sup> )	$a_{\text{pred}}$ $k = 1$ (km <sup>2</sup> )	$a_{\text{pred}}$ $k = 0.75$ (km <sup>2</sup> )	$a_{\text{pred}}$ $k = 0.50$ (km <sup>2</sup> )	
N1495206161	1294705.5	42.7	-18.2	304.9	-21.7	259.4	396.51160	0.00187	967.6930	517.9379	516.7247	523.9229	
35	N1495311312	759950.5	37.1	-11.6	23.3	-21.6	60.7	441.52603	0.00102	875.4782	473.1956	464.6283	463.5204
	N1518953101	2748696.2	79.6	-0.2	105.4	-18.5	26.3	112.52875	0.00832	936.0639	252.2294	259.4079	278.8613
	N1551142776	1958827.1	79.7	37.5	358.6	-13.6	64.0	131.82022	0.00863	1073.9272	202.1025	211.6382	233.8763
	N1552435415	1408418.5	71.1	39.7	182.1	-13.4	233.0	156.52940	0.00212	1089.9978	236.4063	248.8237	275.2325
	N1552559550	2128087.8	76.1	34.2	359.5	-13.4	62.1	153.74387	0.00710	1041.6052	216.2016	225.0033	246.5506
	N1553980614	2283324.2	73.3	30.3	5.3	-13.1	66.7	174.85187	0.01106	1003.6191	232.7841	239.9312	259.7333
	N1555144412	2156979.0	50.5	14.9	356.3	-12.9	38.9	316.47403	0.01079	875.6731	318.9241	321.5581	335.0835
	N1555273968	1665478.9	64.1	29.9	187.0	-12.9	236.5	193.77692	0.00647	994.6682	268.8191	276.9818	298.2223
	N1555401574	2415179.8	70.1	25.4	10.8	-12.9	71.1	192.75861	0.00907	960.7724	252.7399	257.6930	275.0952

(This table is available in its entirety in machine-readable form.)

**Table 15**  
Brightness Estimates from Clear-filter Images of Polydeuces

Filename	Range (km)	Phase (deg)	Sub-S/C Latitude (deg)	Sub-S/C Longitude (deg)	Sub-solar Latitude (deg)	Sub-solar Longitude (deg)	$A_{\text{eff}}$ Value ( $\text{km}^2$ )	$A_{\text{eff}}$ Error ( $\text{km}^2$ )	$A_{\text{phys}}$ ( $\text{km}^2$ )	$a_{\text{pred}}$ $k = 1$ ( $\text{km}^2$ )	$a_{\text{pred}}$ $k = 0.75$ ( $\text{km}^2$ )	$a_{\text{pred}}$ $k = 0.50$ ( $\text{km}^2$ )
N1495210661	786145.6	20.5	-30.4	160.4	-21.7	139.7	2.90468	0.00001	7.0605	4.2419	4.2603	4.3066
N1495210808	785039.1	20.5	-30.5	160.6	-21.7	139.9	2.91503	0.00050	7.0595	4.2381	4.2567	4.3035
N1495306772	654423.7	23.8	-15.1	314.0	-21.6	289.8	3.43378	0.00023	6.9841	4.3321	4.3030	4.3052
N1502650213	2702061.5	61.8	-13.0	352.9	-20.7	288.4	0.97387	0.00811	6.5699	2.6354	2.6208	2.6964
N1502795114	1786225.5	57.4	-19.8	206.2	-20.7	144.6	0.98527	0.00242	6.8046	2.6539	2.6866	2.8104
N1506004925	1776319.6	42.5	-0.3	24.1	-20.3	345.8	1.53273	0.00150	6.5743	3.0580	3.0755	3.1661
N1506764534	2079087.6	74.1	-0.3	130.9	-20.2	57.7	1.00535	0.00187	6.8619	2.3180	2.3419	2.4618
N1552385671	1995458.6	58.7	22.0	2.3	-13.4	50.1	1.07005	0.00245	6.7750	2.4551	2.4817	2.6011
N1552606368	2087051.8	75.1	37.9	328.4	-13.3	27.1	0.67719	0.00367	7.4350	1.7321	1.8083	1.9824
N1555091419	1332245.4	52.9	18.5	165.6	-12.9	208.8	0.99503	0.00121	6.6734	2.5446	2.5833	2.7098

(This table is available in its entirety in machine-readable form.)

**Table 16**  
Brightness Estimates from Clear-filter Images of Pan

Filename	Range (km)	Phase (deg)	Sub-S/C Latitude (deg)	Sub-S/C Longitude (deg)	Sub-solar Latitude (deg)	Sub-solar Longitude (deg)	$A_{\text{eff}}$ Value (km <sup>2</sup> )	$A_{\text{eff}}$ Error (km <sup>2</sup> )	$A_{\text{phys}}$ (km <sup>2</sup> )	$a_{\text{pred}}$ $k = 1$ (km <sup>2</sup> )	$a_{\text{pred}}$ $k = 0.75$ (km <sup>2</sup> )	$a_{\text{pred}}$ $k = 0.50$ (km <sup>2</sup> )	
N1577141695	1928322.1	23.9	14.1	255.1	-9.2	260.7	222.3964	0.0696	578.4056	329.4306	331.6341	337.6532	
N1578630786	1758181.6	32.0	22.1	241.8	-8.9	249.6	184.8326	0.0461	584.9566	296.6020	301.0208	311.0923	
N1579656793	1773520.2	33.9	21.7	108.1	-8.7	123.4	178.0623	0.0538	593.9390	290.1136	297.4645	310.7608	
N1579750304	1820849.6	38.5	24.4	60.8	-8.7	80.9	166.6279	0.0497	592.5009	285.7020	290.0645	300.9773	
N1580566295	1680456.4	25.2	16.6	232.0	-8.6	233.0	195.7154	0.0450	555.9801	293.7928	297.1923	304.7319	
37	N1580653070	1733973.4	31.7	20.7	129.4	-8.6	141.7	163.4020	0.0510	565.7847	265.4792	272.7606	285.4930
	N1580766531	1705000.6	35.9	25.8	232.9	-8.5	243.8	166.9957	0.0418	585.8973	276.7147	282.0406	293.7582
	N1581513746	1618819.1	20.3	11.3	262.5	-8.4	257.6	239.9507	0.0549	578.0841	339.4847	341.6902	346.8926
	N1582637274	1579629.0	30.4	21.2	110.2	-8.2	117.9	186.9957	0.0390	590.8297	301.4664	307.5970	319.1276
	N1583401389	1432863.0	20.6	9.3	265.2	-8.1	254.1	244.7941	0.0396	576.1828	340.2280	342.5082	347.5359

(This table is available in its entirety in machine-readable form.)

**Table 17**  
Brightness Estimates from Clear-filter Images of Atlas

Filename	Range (km)	Phase (deg)	Sub-S/C Latitude (deg)	Sub-S/C Longitude (deg)	Sub-solar Latitude (deg)	Sub-solar Longitude (deg)	$A_{\text{eff}}$ Value (km <sup>2</sup> )	$A_{\text{eff}}$ Error (km <sup>2</sup> )	$A_{\text{phys}}$ (km <sup>2</sup> )	$a_{\text{pred}}$ $k = 1$ (km <sup>2</sup> )	$a_{\text{pred}}$ $k = 0.75$ (km <sup>2</sup> )	$a_{\text{pred}}$ $k = 0.50$ (km <sup>2</sup> )	
N1495208581	1200176.6	20.9	-19.6	50.0	-21.7	27.8	281.1014	0.0047	657.0602	362.1453	363.9504	367.7587	
38	N1503007485	1538741.6	34.7	-19.2	68.2	-20.7	31.3	223.5278	0.0023	668.9564	338.6541	343.4461	352.5163
	N1503007793	1533078.1	34.6	-19.2	70.2	-20.7	33.4	227.3121	0.0027	670.7019	341.2420	346.0067	355.0086
	N1503008105	1527283.9	34.5	-19.3	72.3	-20.7	35.5	228.6507	0.0051	672.3640	343.8194	348.5363	357.4478
	N1503008417	1521438.0	34.4	-19.4	74.3	-20.7	37.7	231.1872	0.0018	673.9126	346.3409	350.9915	359.7968
	N1503008885	1512585.0	34.2	-19.5	77.4	-20.7	40.9	232.9991	0.0036	676.0113	349.9915	354.5059	363.1126
	N1503009353	1503649.2	34.1	-19.6	80.6	-20.7	44.2	232.8272	0.0053	677.8268	353.4491	357.7854	366.1541
	N1503009821	1494651.4	34.0	-19.7	83.7	-20.7	47.4	237.5102	0.0028	679.3419	356.6757	360.7953	368.8904
	N1503010289	1485613.0	33.9	-19.8	86.9	-20.7	50.6	240.1510	0.0030	680.5445	359.6346	363.5007	371.2880
	N1503069320	1141798.9	26.9	-22.4	128.2	-20.7	99.3	281.0052	0.0022	680.1461	383.0209	383.2054	386.1073

(This table is available in its entirety in machine-readable form.)

**Table 18**  
Brightness Estimates from Clear-filter Images of Prometheus

Filename	Range (km)	Phase (deg)	Sub-S/C Latitude (deg)	Sub-S/C Longitude (deg)	Sub-solar Latitude (deg)	Sub-solar Longitude (deg)	$A_{\text{eff}}$ Value (km $^2$ )	$A_{\text{phys}}$ (km $^2$ )	$a_{\text{pred}}$ $k = 1$ (km $^2$ )	$a_{\text{pred}}$ $k = 0.75$ (km $^2$ )	$a_{\text{pred}}$ $k = 0.50$ (km $^2$ )
N1575914492	2251982.5	23.7	11.0	290.4	-9.4	302.5	3789.8745	5945.7690	3187.5754	3251.0505	3354.0364
N1577051965	1729552.4	21.7	10.5	105.2	-9.2	114.1	2767.1677	6027.8188	3416.9006	3461.8240	3542.7866
N1577098105	1950314.6	23.5	11.7	56.7	-9.2	67.5	3105.4451	5615.8433	3143.3091	3130.0500	3154.3108
N1577215016	1997065.0	30.5	16.9	126.3	-9.2	142.4	1868.2275	5680.9424	2381.0442	2488.8511	2652.8489
N1579655833	1695057.1	33.8	22.7	159.5	-8.7	172.1	1180.3311	4969.6963	1394.5358	1483.8430	1628.8689
N1579750574	1792714.6	39.1	24.8	75.0	-8.7	95.8	2139.3582	6508.8945	3160.9849	3228.7004	3371.5254
N1580566520	1695084.1	25.1	16.5	241.6	-8.6	242.1	2460.6575	5902.4258	3075.2437	3117.7126	3207.7449
N1580613950	1675761.0	28.5	19.4	198.9	-8.6	204.3	1072.9626	4690.8086	1637.4780	1684.0397	1775.9514
N1580652770	1801057.0	31.4	19.9	94.4	-8.5	107.9	2452.1985	6411.5083	3319.8735	3397.4214	3536.6499
N1581773008	1698358.5	36.4	24.8	146.6	-8.4	162.0	1182.3083	5469.3691	1606.8419	1726.7169	1913.2938

(This table is available in its entirety in machine-readable form.)

**Table 19**  
Brightness Estimates from Clear-filter Images of Pandora

Filename	Range (km)	Phase (deg)	Sub-S/C Latitude (deg)	Sub-S/C Longitude (deg)	Sub-solar Latitude (deg)	Sub-solar Longitude (deg)	$A_{\text{eff}}$ Value (km $^2$ )	$A_{\text{phys}}$ (km $^2$ )	$a_{\text{pred}}$ $k = 1$ (km $^2$ )	$a_{\text{pred}}$ $k = 0.75$ (km $^2$ )	$a_{\text{pred}}$ $k = 0.50$ (km $^2$ )
N1509277557	468022.3	22.9	-0.4	265.5	-19.9	253.3	2551.8445	5090.0981	3120.5850	3123.7810	3154.0962
N1509278230	472646.5	22.6	-0.4	269.5	-19.9	257.8	2570.1541	5096.4727	3147.9783	3147.3135	3173.4172
N1509279125	478756.8	22.3	-0.4	274.7	-19.9	263.7	2566.7014	5092.3550	3167.1782	3161.3831	3181.8542
N1580567525	1640145.8	26.5	17.1	154.1	-8.6	160.8	1430.8479	4400.8467	2070.5557	2112.7646	2190.2957
N1580765496	1904911.6	35.2	22.9	17.8	-8.5	34.0	1456.2356	4503.1094	1980.4275	2009.6714	2086.2158
N1586165759	1350404.0	30.7	22.8	196.6	-7.6	192.5	1438.1946	4457.3887	1918.5052	1974.0736	2072.5266
N1587847451	1348720.8	33.2	25.9	181.8	-7.3	180.1	1434.0127	4492.5977	1816.3823	1879.5070	1989.8180
N1588712327	1356261.8	36.9	29.6	149.3	-7.1	152.9	1364.9861	4862.9883	1992.1320	2069.7925	2203.2756
N1588750068	1531763.5	36.4	28.7	36.2	-7.1	43.1	1643.4033	4929.4019	2191.9797	2248.6235	2360.1055
N1589546843	1256224.4	37.1	28.9	295.2	-7.0	285.6	1808.1101	5304.1875	2643.2776	2693.0691	2801.2913

(This table is available in its entirety in machine-readable form.)

**Table 20**  
Brightness Estimates from Clear-filter Images of Janus

Filename	Range (km)	Phase (deg)	Sub-S/C Latitude (deg)	Sub-S/C Longitude (deg)	Sub-solar Latitude (deg)	Sub-solar Longitude (deg)	$A_{\text{eff}}$ Value (km <sup>2</sup> )	$A_{\text{phys}}$ (km <sup>2</sup> )	$a_{\text{pred}}$ $k = 1$ (km <sup>2</sup> )	$a_{\text{pred}}$ $k = 0.75$ (km <sup>2</sup> )	$a_{\text{pred}}$ $k = 0.50$ (km <sup>2</sup> )	
N1524964907	216295.5	32.9	-0.2	231.7	-17.7	260.0	7242.8188	23032.1738	13006.3779	12950.2812	13073.6650	
N1524965120	218050.4	33.1	-0.2	232.7	-17.7	261.3	7309.7822	23068.7754	13013.6660	12960.8555	13088.8672	
N1524965317	219704.9	33.2	-0.2	233.7	-17.7	262.4	7263.7207	23101.8184	13018.2275	12968.6035	13101.0693	
N1559172642	1524436.8	32.8	3.4	240.2	-12.3	269.3	7429.6016	23336.8145	13109.0371	13110.5742	13289.6104	
N1574754459	2196734.8	30.9	6.4	117.4	-9.6	143.9	5808.9624	23470.2305	12579.3428	12747.0762	13089.3350	
40	N1575011551	1781307.5	35.9	8.7	214.5	-9.5	245.6	6037.6162	22617.5801	12008.4717	11995.7139	12184.7939
	N1575756631	2123755.0	20.2	7.7	25.9	-9.4	36.7	7426.0449	22477.6230	13007.3262	13013.5850	13124.5449
	N1577098705	1741632.5	24.1	13.2	158.3	-9.2	167.3	5780.8052	22500.2676	12159.1025	12271.3994	12527.1123
	N1579447272	1512084.6	21.1	12.1	219.4	-8.8	216.3	7683.9600	22952.0625	13004.3496	13092.5225	13302.1230
	N1579749394	1653319.0	37.8	27.0	216.0	-8.7	228.6	5322.4150	24143.4258	11435.9316	11649.8604	12127.4639

(This table is available in its entirety in machine-readable form.)

**Table 21**  
Brightness Estimates from Clear-filter Images of Epimetheus

Filename	Range (km)	Phase (deg)	Sub-S/C Latitude (deg)	Sub-S/C Longitude (deg)	Sub-solar Latitude (deg)	Sub-solar Longitude (deg)	$A_{\text{eff}}$ Value (km <sup>2</sup> )	$A_{\text{phys}}$ (km <sup>2</sup> )	$a_{\text{pred}}k = 1$ (km <sup>2</sup> )	$a_{\text{pred}}k = 0.75$ (km <sup>2</sup> )	$a_{\text{pred}}k = 0.50$ (km <sup>2</sup> )	
N1564454340	3290726.2	35.7	0.2	102.2	-11.4	136.2	2377.4211	10843.6914	5896.0864	5991.3555	6178.0361	
N1575054751	1876191.9	36.5	8.1	305.2	-9.5	337.3	2441.1824	10606.0703	5452.1060	5553.2422	5752.8184	
N1575800491	1999183.2	23.9	9.4	116.1	-9.4	130.8	3085.0137	10715.6104	6366.2119	6423.5264	6536.9209	
N1577051695	1832468.5	21.1	9.9	62.7	-9.2	71.6	3373.8743	10739.0752	6656.8516	6666.2461	6722.8457	
N1577141905	1907909.6	24.0	14.3	248.9	-9.2	254.0	3560.7798	10821.0596	6570.8481	6597.0679	6682.7441	
41	N1578545720	1936707.5	26.9	16.3	20.4	-8.9	29.8	2513.5916	10150.9297	5696.2822	5726.6514	5825.5596
	N1579749784	1883149.0	37.0	23.5	30.9	-8.7	49.6	2117.9294	10441.0947	5433.1025	5473.6685	5617.6523
	N1580482099	1570688.6	21.3	12.1	115.5	-8.6	120.5	3110.6165	10744.9404	6555.0938	6591.6235	6677.4932
	N1580528164	1840117.9	22.2	13.0	31.9	-8.6	37.4	2827.2590	10258.7510	6044.1182	6064.4678	6137.0151
	N1580652470	1905801.2	30.1	18.8	49.7	-8.5	62.4	2659.8137	10640.1279	6071.2495	6099.3809	6208.2104

(This table is available in its entirety in machine-readable form.)

**Table 22**  
Brightness Estimates from Clear-filter Images of Mimas

Filename	Range (km)	Phase (deg)	Sub-S/C Latitude (deg)	Sub-S/C Longitude (deg)	Sub-solar Latitude (deg)	Sub-solar Longitude (deg)	$A_{\text{eff}}$ Value (km <sup>2</sup> )	$A_{\text{phys}}$ (km <sup>2</sup> )	$a_{\text{pred}}$ $k = 1$ (km <sup>2</sup> )	$a_{\text{pred}}$ $k = 0.75$ (km <sup>2</sup> )	$a_{\text{pred}}$ $k = 0.50$ (km <sup>2</sup> )	
N1481705814	901668.0	26.0	1.2	328.3	-23.1	318.9	58778.3984	120528.9844	72071.1719	72161.4062	72962.6797	
N1488814545	1607311.0	36.1	-0.0	92.4	-22.4	63.2	48915.5898	124417.2969	69472.8047	70052.2266	71725.5547	
N1488829675	1389412.9	38.3	-0.3	160.1	-22.4	127.9	43297.4219	118568.5938	64146.7969	64234.5859	65466.9531	
N1488881205	1509689.5	33.6	0.1	25.5	-22.4	359.8	47407.6680	119972.6641	66077.2109	66508.0078	67946.8750	
N1488897255	1261645.8	28.7	-0.1	87.2	-22.4	68.7	54479.7578	124463.9375	74076.8281	74477.5938	75695.7109	
42	N1488913065	1011333.3	30.2	-0.4	157.8	-22.4	136.5	51089.8398	118754.7812	68925.3750	68958.1172	69846.3750
	N1488923681	968930.9	34.8	-0.5	211.3	-22.4	183.4	47263.4258	119611.2031	64885.4414	65408.5273	66984.3828
	N1490685953	1217789.1	27.1	-0.1	73.3	-22.2	57.0	55973.9688	124187.1406	74193.6562	74603.1797	75775.0391
	N1493535431	1568050.6	31.5	-19.1	87.8	-21.9	54.3	51982.8047	124988.4766	72796.9688	73410.1172	74912.5781
	N1496631451	1693633.4	36.9	-19.0	100.0	-21.5	60.7	46542.9180	124733.3438	69656.1016	70284.1953	72002.0703

(This table is available in its entirety in machine-readable form.)

**Table 23**  
Brightness Estimates from Clear-filter Images of Enceladus

Filename	Range (km)	Phase (deg)	Sub-S/C Latitude (deg)	Sub-S/C Longitude (deg)	Sub-solar Latitude (deg)	Sub-solar Longitude (deg)	$A_{\text{eff}}$ Value (km <sup>2</sup> )	$A_{\text{phys}}$ (km <sup>2</sup> )	$a_{\text{pred}}$ $k = 1$ (km <sup>2</sup> )	$a_{\text{pred}}$ $k = 0.75$ (km <sup>2</sup> )	$a_{\text{pred}}$ $k = 0.50$ (km <sup>2</sup> )	
N1477565247	765619.5	33.6	4.8	269.2	-23.6	250.8	129597.7109	200214.7812	114034.1094	114808.4453	117213.5234	
N1481509793	1980087.2	38.1	-3.6	37.2	-23.2	3.3	112414.9297	198977.5781	107244.1953	108142.8125	110943.3359	
N1481706474	671641.8	31.8	1.9	262.1	-23.2	242.0	134909.2031	200088.9375	115689.9297	116444.5000	118710.9219	
N1488878396	1267780.9	29.5	-0.2	107.2	-22.4	87.3	131631.8125	199811.5156	118290.2266	118853.9844	120768.7969	
N1490643112	1433963.0	30.3	-0.2	73.8	-22.2	52.4	131019.1172	200326.0312	117010.0703	117714.7188	119840.6875	
43	N1490687213	978323.2	38.4	-0.2	219.8	-22.2	187.5	113043.2344	197782.8125	105885.6484	106861.8672	109754.1641
	N1495039341	1616055.4	38.8	-20.1	140.7	-21.7	99.0	109264.4844	198342.5156	108068.6719	108744.9062	111325.3438
	N1499868413	1547410.6	29.0	-18.2	51.8	-21.1	21.1	133408.5625	200039.6406	117567.9141	118313.5156	120384.3125
	N1501504263	1398906.6	32.4	-17.5	349.5	-20.9	315.4	127095.5000	198437.7969	113908.2109	114500.0703	116622.1797
	N1502971691	1461577.5	36.7	-21.5	135.8	-20.7	96.4	114585.1250	198719.9844	110699.1016	111351.0156	113779.3359

(This table is available in its entirety in machine-readable form.)

**Table 24**  
Brightness Estimates from Clear-filter Images of Tethys

Filename	Range (km)	Phase (deg)	Sub-S/C Latitude (deg)	Sub-S/C Longitude (deg)	Sub-solar Latitude (deg)	Sub-solar Longitude (deg)	$A_{\text{eff}}$ Value (km <sup>2</sup> )	$A_{\text{phys}}$ (km <sup>2</sup> )	$a_{\text{pred}}k = 1$ (km <sup>2</sup> )	$a_{\text{pred}}k = 0.75$ (km <sup>2</sup> )	$a_{\text{pred}}k = 0.50$ (km <sup>2</sup> )
N1477564227	668321.5	34.3	5.5	108.6	-23.6	127.2	467384.2500	888561.6875	501631.5938	505492.8750	516790.9688
44	N1481443192	2092752.0	38.5	-5.2	82.3	-23.2	418260.5312	890977.5000	482936.9062	487384.6250	500435.1562
	N1488790300	1703386.8	35.0	-0.2	87.5	-22.4	453760.6875	890506.1250	500846.7188	504735.3750	516249.4062
	N1488792254	1675049.4	34.9	-0.2	91.7	-22.4	452431.1562	890194.3750	501912.9062	505747.7500	517133.7812
	N1488822445	1311927.4	38.4	0.0	162.6	-22.4	428045.9062	875014.5000	474645.6562	477596.4375	488958.7188
	N1488925841	1396850.2	28.3	-0.4	17.0	-22.4	497584.6562	882233.8125	521838.3750	524370.2500	532586.0625
	N1490557912	1967571.0	39.0	-0.3	33.5	-22.2	409800.2500	884963.8750	473073.0312	477229.9375	490086.0312
	N1493533631	1427707.1	28.7	-21.0	117.6	-21.9	514314.7812	887667.5625	530566.8750	532909.5000	540927.2500
	N1495251742	1033161.4	31.4	-18.6	311.5	-21.7	456368.3750	888833.3125	517746.8125	520331.3438	529449.4375
	N1496638951	1490964.0	35.4	-21.2	137.4	-21.5	453459.3438	882876.6250	497749.6562	500517.2500	510863.5625

(This table is available in its entirety in machine-readable form.)

**Table 25**  
Brightness Estimates from Clear-filter Images of Dione

Filename	Range (km)	Phase (deg)	Sub-S/C Latitude (deg)	Sub-S/C Longitude (deg)	Sub-solar Latitude (deg)	Sub-solar Longitude (deg)	$A_{\text{eff}}$ Value (km <sup>2</sup> )	$A_{\text{phys}}$ (km <sup>2</sup> )	$a_{\text{pred}}k = 1$ (km <sup>2</sup> )	$a_{\text{pred}}k = 0.75$ (km <sup>2</sup> )	$a_{\text{pred}}k = 0.50$ (km <sup>2</sup> )	
N1477563207	1170144.5	28.2	3.0	343.0	-23.6	333.3	370990.3125	995340.3750	592636.1250	595648.3750	605015.7500	
N1490685593	809791.7	29.7	-0.3	165.6	-22.2	145.0	420229.0312	987021.1250	580514.4375	583542.4375	593330.8750	
N1493443511	2022987.0	35.6	-16.2	59.5	-21.9	22.2	384033.1875	994090.6875	554967.2500	558834.2500	571424.5625	
N1493490431	1483911.4	31.6	-21.4	127.9	-21.9	93.8	440784.8438	989768.0000	574031.2500	577404.6250	588149.5625	
N1495082541	1947127.1	34.5	-15.8	32.5	-21.7	356.6	373174.8438	995271.3125	562407.0000	566208.2500	578319.3750	
45	N1496541751	1899698.2	38.0	-17.9	97.9	-21.5	57.6	382418.9688	991109.1250	540685.9375	545129.3125	558951.5000
	N1498185942	1845955.9	33.4	-17.6	75.2	-21.3	39.9	411062.7188	992851.3125	566026.3125	569668.1875	581332.3750
	N1499867332	1303523.9	21.4	-21.9	102.0	-21.1	79.0	468760.2812	991185.3750	619325.9375	621271.0000	627294.8750
	N1501604957	288094.3	37.3	-43.3	239.5	-20.9	203.5	317982.9375	992150.6875	543207.5000	547919.8750	561828.8750
	N1501609726	273323.9	39.9	-41.3	251.5	-20.9	210.8	288696.3750	992566.5000	528932.3125	533965.6250	548955.6250

(This table is available in its entirety in machine-readable form.)

**Table 26**  
Brightness Estimates from Clear-filter Images of Rhea

Filename	Range (km)	Phase (deg)	Sub-S/C Latitude (deg)	Sub-S/C Longitude (deg)	Sub-solar Latitude (deg)	Sub-solar Longitude (deg)	$A_{\text{eff}}$ Value (km <sup>2</sup> )	$A_{\text{phys}}$ (km <sup>2</sup> )	$a_{\text{pred}}$ $k = 1$ (km <sup>2</sup> )	$a_{\text{pred}}$ $k = 0.75$ (km <sup>2</sup> )	$a_{\text{pred}}$ $k = 0.50$ (km <sup>2</sup> )	
N1477220185	2585475.5	39.2	-8.8	76.4	-23.6	38.3	710596.1875	1835874.0000	988102.5625	996176.2500	1022431.0000	
N1481511293	2012632.4	30.2	-3.6	58.0	-23.2	34.2	829956.0000	1839455.7500	1078401.8750	1084108.8750	1102722.0000	
N1484528177	500340.0	34.8	3.7	318.7	-22.9	295.5	633058.1875	1841690.8750	1033522.5000	1041154.6250	1064504.7500	
N1484528732	495890.5	34.7	3.7	318.9	-22.9	296.0	638173.2500	1841716.1250	1035086.8750	1042678.6250	1065899.0000	
N1486953989	2366332.0	38.6	-1.8	45.3	-22.6	11.8	684924.6875	1841255.3750	998314.5625	1006207.2500	1031875.0000	
46	N1488892945	1774114.6	29.4	-0.2	19.2	-22.4	359.3	774522.9375	1843294.6250	1088845.6250	1094685.0000	1112966.2500
	N1488919155	1561799.4	24.0	-0.2	32.8	-22.4	23.4	888326.0625	1842469.8750	1132182.8750	1136421.3750	1149809.7500
	N1488924761	1510984.0	23.1	-0.2	35.5	-22.4	28.5	907498.5625	1842268.6250	1137753.1250	1141781.3750	1154478.5000
	N1490556712	1439026.4	31.2	-0.3	115.6	-22.2	92.9	838673.0000	1831451.3750	1065606.7500	1071885.0000	1091575.8750
	N1506067445	1617571.4	33.7	-0.3	20.0	-20.3	352.3	709971.7500	1843247.8750	1050104.1250	1057106.6250	1079044.0000

(This table is available in its entirety in machine-readable form.)

**Table 27**  
Brightness Estimates from Color Images of Aegeon

Filename	Filter	Range (km)	Phase (deg)	Sub-S/C Latitude (deg)	Sub-S/C Longitude (deg)	Sub-solar Latitude (deg)	Sub-solar Longitude (deg)	$A_{\text{eff}}$ Value ( $\text{km}^2$ )	$A_{\text{phys}}$ ( $\text{km}^2$ )	$a_{\text{pred}}$ $k = 1$ ( $\text{km}^2$ )	$a_{\text{pred}}$ $k = 0.75$ ( $\text{km}^2$ )	$a_{\text{pred}}$ $k = 0.50$ ( $\text{km}^2$ )
N1643264167	CLR	14546.9	73.3	74.0	168.5	2.6	140.8	0.01090	0.5320	0.1032	0.1189	0.1437
N1643264273	CLR	14875.4	70.5	71.5	165.2	2.6	141.3	0.03011	0.5259	0.1053	0.1212	0.1461
N1643264379	CLR	15235.6	67.9	69.0	162.9	2.6	141.8	0.01150	0.5193	0.1071	0.1230	0.1479
N1643264504	CLR	15694.0	65.0	66.2	161.1	2.6	142.5	0.00276	0.5110	0.1088	0.1247	0.1494
N1643264609	RED	16121.3	62.6	63.9	160.1	2.6	143.0	0.01380	0.5034	0.1099	0.1257	0.1501
N1643264664	GRN	16352.0	61.4	62.7	159.6	2.6	143.3	0.01555	0.4994	0.1103	0.1260	0.1503
N1643264720	BL1	16590.4	60.2	61.6	159.3	2.6	143.6	0.01085	0.4953	0.1107	0.1263	0.1504
N1643264798	UV3	16902.0	58.8	60.2	158.9	2.6	144.0	0.00929	0.4901	0.1110	0.1265	0.1503
N1643264854	IR3	17195.7	57.5	59.0	158.7	2.6	144.3	0.01505	0.4853	0.1113	0.1266	0.1502
N1643264914	CLR	17482.6	56.4	57.9	158.5	2.6	144.6	0.01383	0.4807	0.1114	0.1266	0.1499

(This table is available in its entirety in machine-readable form.)

**Table 28**  
Brightness Estimates from Color Images of Methone

Filename	Filter	Range (km)	Phase (deg)	Sub-S/C Latitude (deg)	Sub-S/C Longitude (deg)	Sub-solar Latitude (deg)	Sub-solar Longitude (deg)	$A_{\text{eff}}$ Value ( $\text{km}^2$ )	$A_{\text{phys}}$ ( $\text{km}^2$ )	$a_{\text{pred}}$ $k = 1$ ( $\text{km}^2$ )	$a_{\text{pred}}$ $k = 0.75$ ( $\text{km}^2$ )	$a_{\text{pred}}$ $k = 0.50$ ( $\text{km}^2$ )
N1716192103	CLR	4454.4	63.1	-15.6	130.2	14.4	74.0	1.53738	6.5733	3.1004	3.0766	3.1407
N1716192136	UV3	4604.6	62.3	-15.1	129.6	14.4	74.2	1.33006	6.5866	3.1460	3.1221	3.1853
N1716192191	GRN	4868.9	60.9	-14.2	128.8	14.4	74.4	1.61003	6.6073	3.2183	3.1941	3.2558
N1716192224	IR1	5026.2	60.2	-13.7	128.3	14.4	74.5	1.69522	6.6183	3.2571	3.2328	3.2935
N1716192257	IR3	5181.9	59.5	-13.3	127.9	14.4	74.7	1.69304	6.6282	3.2928	3.2682	3.3281
N1716192290	CLR	5343.4	58.9	-12.9	127.5	14.4	74.8	1.72429	6.6377	3.3273	3.3025	3.3614
N1716192323	BL1	5500.6	58.3	-12.5	127.2	14.4	75.0	1.69781	6.6461	3.3585	3.3335	3.3915
N1716192356	RED	5662.6	57.7	-12.1	126.9	14.4	75.1	1.76546	6.6540	3.3885	3.3632	3.4203
N1716192389	IR2	5822.3	57.2	-11.7	126.6	14.4	75.2	1.81560	6.6611	3.4162	3.3907	3.4468
N1716192437	IR4	6033.7	56.5	-11.3	126.2	14.4	75.4	1.65345	6.6697	3.4502	3.4243	3.4792

(This table is available in its entirety in machine-readable form.)

## ORCID iDs

- M. M. Hedman <https://orcid.org/0000-0002-8592-0812>  
P. Helfenstein <https://orcid.org/0000-0003-4870-1300>  
R. O. Chancia <https://orcid.org/0000-0002-7867-7674>  
E. Roussos <https://orcid.org/0000-0002-5699-0678>  
C. Paranicas <https://orcid.org/0000-0002-4391-8255>  
A. J. Verbiscer <https://orcid.org/0000-0002-3323-9304>

## References

- Acton, C. H. 1996, *P&SS*, 44, 65  
Black, G. J., Campbell, D. B., & Carter, L. M. 2007, *Icar*, 191, 702  
Brown, R. H., Baines, K. H., Bellucci, G., et al. 2004, *SSRv*, 115, 111  
Buratti, B., & Veverka, J. 1984, *Icar*, 58, 254  
Buratti, B. J. 1984, *Icar*, 59, 392  
Buratti, B. J., Bauer, J. M., Hicks, M. D., et al. 2010, *Icar*, 206, 524  
Buratti, B. J., Mosher, J. A., & Johnson, T. V. 1990, *Icar*, 87, 339  
Buratti, B. J., Mosher, J. A., Nicholson, P. D., McGhee, C. A., & French, R. G. 1998, *Icar*, 136, 223  
Buratti, B. J., Thomas, P. C., Roussos, E., et al. 2019, *Sci*, 364, eaat2349  
Calvin, W. M., Clark, R. N., Brown, R. H., & Spencer, J. R. 1995, *JGR*, 100, 19041  
Clark, R. N., Cruikshank, D. P., Jaumann, R., et al. 2012, *Icar*, 218, 831  
Clark, R. N., Curchin, J. M., Jaumann, R., et al. 2008, *Icar*, 193, 372  
Cuzzi, J. N., & Estrada, P. R. 1998, *Icar*, 132, 1  
Dobrovolskis, A. R., Alvarez, J. L., Zahnle, K. J., & Lissauer, J. J. 2010, *Icar*, 210, 436  
Filacchione, G., Capaccioni, F., Ciarniello, M., et al. 2012, *Icar*, 220, 1064  
Filacchione, G., Capaccioni, F., Clark, R. N., et al. 2013, *ApJ*, 766, 76  
Franz, O. G., & Millis, R. L. 1975, *Icar*, 24, 433  
Hamilton, D. P., & Burns, J. A. 1994, *Sci*, 264, 550  
Hand, K. P., & Carlson, R. W. 2015, *GeoRL*, 42, 3174  
Hapke, B. 1986, *Icar*, 66, 270  
Hedman, M. M., Burns, J. A., Hamilton, D. P., & Showalter, M. R. 2012, *Icar*, 217, 322  
Hedman, M. M., Cooper, N. J., Murray, C. D., et al. 2010, *Icar*, 207, 433  
Hedman, M. M., Postberg, F., Hamilton, D. P., Renner, S., & Hsu, H. W. 2018, in *Planetary Ring Systems. Properties, Structure, and Evolution*, ed. M. S. Tiscareno & C. D. Murray (Cambridge: Cambridge Univ. Press), 308  
Helfenstein, P., & Veverka, J. 1989, in *Asteroids II*, ed. R. P. Binzel, T. Gehrels, & M. S. Matthews (Tucson, AZ: Univ. Arizona Press), 557  
Hendrix, A. R., Buratti, B. J., Cruikshank, D. P., et al. 2018, in *Enceladus and the Icy Moons of Saturn*, ed. P. Schenk et al. (Tucson, AZ: Univ. Arizona Press), 307  
Hibbitts, C. A., Stockstill-Cahill, K., Wing, B., & Paranicas, C. 2019, *Icar*, 326, 37  
Hirata, N., Miyamoto, H., & Showman, A. P. 2014, *GeoRL*, 41, 4135  
Horanyi, M., Burns, J. A., & Hamilton, D. P. 1992, *Icar*, 97, 248  
Horányi, M., Juhász, A., & Morfill, G. E. 2008, *GeoRL*, 35, L04203  
Howett, C. J. A., Hendrix, A. R., Nordheim, T. A., et al. 2018, in *Enceladus and the Icy Moons of Saturn*, ed. P. Schenk et al. (Tucson, AZ: Univ. Arizona Press), 343  
Howett, C. J. A., Spencer, J. R., Schenk, P., et al. 2011, *Icar*, 216, 221  
Kempf, S., Beckmann, U., Moragas-Klostermeyer, G., et al. 2008, *Icar*, 193, 420  
Koschny, D., & Grün, E. 2001, *Icar*, 154, 391  
Krimigis, S. M., Mitchell, D. G., Hamilton, D. C., et al. 2004, *SSRv*, 114, 233

- Le Gall, A., West, R. D., & Bonnefoy, L. E. 2019, *GeoRL*, **46**, 11747
- McEwen, A. S. 1991, *Icar*, **92**, 298
- Minnaert, M. 1941, *ApJ*, **93**, 403
- Moore, J. M., Chapman, C. R., Bierhaus, E. B., et al. 2007, in *Jupiter*, ed. F. Bagenal et al. (Cambridge: Cambridge Univ. Press), 397
- Muinonen, K., & Lumme, K. 2015, *A&A*, **584**, A23
- Murray, C. D., & Dermott, S. F. 1999, *Solar System Dynamics* (Cambridge: Cambridge Univ. Press)
- Noland, M., Veverka, J., Morrison, D., et al. 1974, *Icar*, **23**, 334
- Ostro, S. J., West, R. D., Wye, L. C., et al. 2010, *Icar*, **206**, 498
- Paranicas, C., Hibbitts, C. A., Kollmann, P., et al. 2018, *Icar*, **302**, 560
- Pitman, K. M., Buratti, B. J., & Mosher, J. A. 2010, *Icar*, **206**, 537
- Porco, C. C., West, R. A., Squyres, S., et al. 2004, *SSRv*, **115**, 363
- Poston, M. J., Mahjoub, A., Ehlmann, B. L., et al. 2018, *ApJ*, **856**, 124
- Roussos, E., Krupp, N., Armstrong, T. P., et al. 2008, *GeoRL*, **35**, L22106
- Schenk, P., Hamilton, D. P., Johnson, R. E., et al. 2011, *Icar*, **211**, 740
- Schröder, S. E., Mottola, S., Keller, H. U., Raymond, C. A., & Russell, C. T. 2014, *P&SS*, **103**, 66
- Scipioni, F., Tosi, F., Stephan, K., et al. 2013, *Icar*, **226**, 1331
- Scipioni, F., Tosi, F., Stephan, K., et al. 2014, *Icar*, **234**, 1
- Shkuratov, Y., Kaydash, V., Korokhin, V., et al. 2011, *P&SS*, **59**, 1326
- Thomas, P., & Helfenstein, P. 2019, *Icar*, in press
- Thomas, P., Tiscareno, M. S., & Helfenstein, P. 2018, in *Enceladus and the Icy Moons of Saturn*, ed. P. Schenk et al. (Tucson, AZ: Univ. Arizona Press), 387
- Thomas, P. C. 2010, *Icar*, **208**, 395
- Thomas, P. C., Burns, J. A., Hedman, M., et al. 2013, *Icar*, **226**, 999
- Tiscareno, M. S., Mitchell, C. J., Murray, C. D., et al. 2013, *Sci*, **340**, 460
- Trumbo, S. K., Brown, M. E., & Hand, K. P. 2019, *Sci*, **5**, aaw7123
- Verbiscer, A., French, R., Showalter, M., & Helfenstein, P. 2007, *Sci*, **315**, 815
- Verbiscer, A., Helfenstein, P., Buratti, B., & Royer, E. 2018, in *Enceladus and the Icy Moons of Saturn*, ed. P. Schenk et al. (Tucson, AZ: Univ. Arizona Press), 323
- Verbiscer, A. J., & Veverka, J. 1989, *Icar*, **82**, 336
- Verbiscer, A. J., & Veverka, J. 1992, *Icar*, **99**, 63
- Verbiscer, A. J., & Veverka, J. 1994, *Icar*, **110**, 155
- Vickers, G. 1996, *Powder Technology*, **86**, 195
- West, R., Knowles, B., Birath, E., et al. 2010, *P&SS*, **58**, 1475
- Ye, S. Y., Gurnett, D. A., & Kurth, W. S. 2016, *Icar*, **279**, 51
- Ye, S. Y., Gurnett, D. A., Kurth, W. S., et al. 2014, *JGRA*, **119**, 6294